Communauté
UNIVERSITÉ Grenoble Alpes

THÈSE

Pour obtenir le grade de

DOCTEUR DE la Communauté UNIVERSITÉ GRENOBLE ALPES

Spécialité : **Sciences de la Terre et de l'Univers et de l'Environnement (CESTUE)**

Arrêté ministériel : 25 mai 2016

Présentée par

Miriam Patricia Ortega Ramírez

Thèse dirigée par **Laurent Oxarango**

préparée au sein **Institut des Géosciences de l'Environnemenet (IGE)**
et de **Terre Univers Environnement**

Analysis of soil structural, and transfer properties using pore scale images and numerical modelling.

Thèse soutenue publiquement le **19 juillet 2019**,
devant le jury composé de :

Azita Ahmadi-Sénichault
Professeur des Universités, ENSAM / I2M Bordeaux , Rapporteur
Laurent Lassabatère
Ingénieur TPE HDR, ENTPE/LEHNA Lyon, Rapporteur
Éric Vincens
Professeur des Universités, École Centrale / LTDS Lyon, Président
Céline Duwig
CR IRD HDR, IGE Grenoble, Examinatrice
Laurent Oxarango
Professeur des Universités, UGA / IGE Grenoble, Directeur de thèse

Acknowledgements

First of all, I would like to express my gratitude to my mother Maria de la Luz whose love has always motivated me, and her support is a building stone for the realization of all my plans.

I thank to Dr. Laurent Oxarango for his guidance in my discovery of the vast world of the porous media science, and his flexibility to let me explore where my scientific curiosity was leading.

I would also like to express my gratitude to Dr. Blanca Prado, and Dr. Alfonso Gastelum for their orientation in my transition from theoretical physics to soil physics as well as being part of my thesis committee.

Thanks to the jury members and the rest of the my thesis committee for reading my thesis, give me theirs corrections and the stimulating discussions: Dr. Azita Ahmadi-Sénichault, Dr. Laurent Lassabatère, Dr. Éric Vincens, Dr. Céline Duwig, Dr. Patrice Delmas, and Dr. Jeans Martins.

I acknowledge CONACyT (Consejo nacional de ciencia y tecnología) financial help for supporting this research through the program "becas en el extranjero", and to the IGE (Institut des Géosciences de l'Environnement) for granting me with a contract for the last months of this research. I am also grateful to have been part of the project H2020 Rise PROTINUS and to the Instituto de Geología at UNAM (my Alma Mater) for hosting me during my short stays.

Arriving to my PhD dissertation was also possible thanks to the fraternal and bounded atmosphere that was created by the PhD and master students that surrounded me. I would like to make an especial mention to Magda,

Catherine, Claudio, Ana, Mabe, Mathilde, Gaby, Javier, Charlene, Mateo, Yasmine, Foteini, Anil and Jean Carlos.

Finally I want to thank the ever present love of Arturo Amor, regardless of any distance, it is my other building stone that inspires me and motivates me to perform achievements like this.

Analyse des propriétés structurelles et de transport de sols granulaires par imagerie et simulations numériques à l'échelle des pores.

Résumé

Les transferts de fluide et de soluté en milieux poreux présentent de nombreuses applications dans des contextes environnementaux ou industriels. Ils sont classiquement décrits par des équations macroscopiques faisant intervenir des propriétés effectives telles que la perméabilité ou la dispersivité. Ces propriétés dépendent fortement de la structure géométrique complexe du réseau de pores qui permet le mouvement du fluide. La micro-tomographie à rayon X a récemment permis d'accéder à une représentation tri-dimensionnelle réaliste de la structure interne de ces milieux. Les images produites permettent d'estimer les propriétés morphologiques du milieu poreux mais aussi les propriétés de transport à partir de simulations numériques directes. Le travail réalisé dans cette thèse constitue une contribution à l'état de l'art dans ce domaine. Une attention particulière est portée à l'effet de la résolution spatiale de la tomographie sur la qualité de l'estimation des propriétés morphologiques et de transport. Un ensemble de méthodes numériques pertinentes a été sélectionné, dévelopée et mis en oeuvre afin de pouvoir calculer la porosité, la surface spécifique, la distribution de taille de pore, la perméabilité et la dispersivité du milieu sur des volumes représentatifs du matériau. Ces travaux se sont concentrés sur l'étude d'un sable réel et d'un empilement virtuel de sphères à différentes résolutions. Ils ont permis de definir un critère de qualité basé sur le rapport entre des grandeurs caractéristiques des grains et la taille des voxels de l'image. Ce critère permet de déterminer a priori si une image de milieu granulaire est adaptée au calcul de perméabilité et de dispersivité par simulation numérique des équations de Stokes et d'advection-diffusion (ADE). Bien que l'ADE utilise le champs de vitesse du fluide, il s'est avéré qu'elle présente un comportement plus robuste que le calcul d'écoulement.

Mots clés : Milieux poreux, Micro-tomographie X, Écoulement, transport, propriétés effectives

Abstract

Fluid and solute transport in porous media are key processes in a wide range of environmental and engineering applications. They are classically described through macroscopic equation involving effective properties such as permeability or dispersivity. These properties strongly depend on the complex geometric structure of the pore network that allows fluid movements. X-ray micro-computed tomography recently opened the potentiality to produce realistic three-dimensional images of the internal structure of porous media. These images could be used to estimate morphological properties of the material but also transport properties using direct numerical simulations. This PhD thesis provides a contribution to the state of the art in this domain. A particular attention was given to the effect of the tomography resolution on the quality of the estimation of morphological and transport properties. A set of numerical methods were selected or developed and implemented in order to compute the porosity, the specific surface, the pore size distribution, the permeability and the dispersivity in a Representative Elementary Volume of material. They were applied to a sample of real sand and on a virtual pack of spheres. It allowed defining a quality criterion based on the ratio between characteristic sizes of grains and the image voxel size. This criterion allows determining a priori if a given image of granular medium is suitable for permeability and dispersivity computation based on Stokes and Advection-diffusion (ADE) equations respectively. Even if the ADE uses the flow field computed from Stokes equation, it revealed more robust than the flow computation itself.

Keywords : Porous media, X-ray CT, flow, transport, effective properties

Contents

Introduction

Soils are a natural resource key to environmental, social and economical functions such as: biomass production; environment protection (Filtering, buffering and transformation capacity between the critical zone elements); source of raw materials (e.g. clay, sand, gravel and minerals in general; as well as a source of energy and water); gene reservoir; engineering medium; and cultural heritage (Blum, 2005). All of them depend on the soil physical and chemical properties like texture, bulk density, water holding capacity, organic matter content, and soil structure; rock type, cation exchange capacity, acid production resulting from microbial and root respiration, and management strategies (Schoonover and Crim, 2015). The change of these properties affects soil natural and human processes.

Examples of these processes are in the agriculture industry where in order to provide food supply the soil is altered physically through soil preparation techniques such as tillage (Batey, 2009; Badalíková, 2010), leading in some cases to soil erosion (Prosdocimi et al., 2016). In this same industry the soil chemical properties are modified through soil fertilization (Bennett et al., 2001; King et al., 2015). Another example of the manipulation of soil properties comes from the energy industry improvement of the performance of processes like hydrocarbons extraction (Hawthorne et al., 2013), or nuclear waste management (Marschall et al., 2005; Delage et al., 2010). A negative consequence of most of these industries is the soil contamination (Cram et al., 2004). Its remediation depends on the contaminant (Wang et al., 2008; Ren et al., 2018) and the techniques rely on some particular reactive transport process with respect to soil properties. Thanks to the filter function of the soil, it can also clean ground water or waste water in a natural (Keesstra et al., 2012) or constructed way (Kadam et al., 2009). In the mitigation strategies of the climate change the soil plays a key role

being a natural carbon storage (Lal, 2009; Lehmann and Kleber, 2015) and atmospheric CO_2 storage by the technique called CO_2 sequestering (Mehmani et al., 2012).

Most of these examples depict the effects of soil modification through macroscopic properties like porosity (Kumar et al., 2010b), permeability (Juanes et al., 2006a), and dispersivity (Kuncoro et al., 2014). Despite being macroscopic properties, they comprise the remnants of the microstructure of the porous material. By this means, before introducing the micro and macro scale properties of the soil it turns convenient to define the soil as a porous media. This material is defined as a spatial domain that contains a solid portion (the solid matrix) with an interconnected void space (the pore space) (Nield et al., 2006a), such portions are called phases. A sandy soil containing water (fully filled) is said to have two phases, the sand, and the water. The interconnectedness of the void phase are called pores and through them occurs the flow of one or more fluids. Soils, fissured rocks, filter paper and fibrous aggregates are examples of porous media. In this thesis the porous material we deal with is a sandy soil which has two phases: the solid and the water.

When we study a porous media at the microscale, we are considering orders of magnitude of the characteristic length of the pore (for this study this length has an order of magnitude $\approx 1 \times 10^{-6} m$). The macroscale is the scale derived from averaging the microscale properties within a Representative Elementary Volume (REV) which defines a volume at which the parameter of interest is both homogeneous and statistically stationary, but still small to be considered as a volume element of continuum mechanics (for this study $\approx 1 \times 10^{-3} m$. More details about the REV analysis will be presented in the next chapter).

The so-called up-scaling methods are mathematical methods that allow to pass from the micro to the macro scale description. Some of them are the homogenization (Auriault et al., 2010; Bruining et al., 2012) and the volume averaging, the last of which consists in obtaining an average of the studied property (for instance, the pressure, solute concentration, temperature, etc) into the REV. In the macroscale description, this average is considered to be the property value at the center of the REV. By this process of averaging, information on the local variations at the microscopic scale is lost. However,

it is at the macroscopic level at which experimental measurements of state variables can be done (Bear, 2018; Whitaker, 2013).

The study of the porous materials and in particular the soil at a microscale has been improved thanks to the progress in pore scale imaging techniques like the X-ray Micro Computed Tomography (μCT). The μCT is a non destructive and three dimensional (3D) technique to visualize and quantify the internal structures of materials. Applying image analysis techniques enables to compute morphological parameters such as porosity, specific surface, pore size distribution, tortuosity or connectivity. Such information provides a better understanding of the fluid and solute transport (Lehmann et al., 2006; Silin and Patzek, 2006; Vogel et al., 2010).

The imaging techniques also opened the opportunity to take into account the real pore structure while solving flow or transport equations within the pore space by Direct Numerical Simulation (DNS) (Mostaghimi et al., 2013). This new branch of research was originally known under the concept of Digital Rock Physics (DRP). It has been applied to various kind of phenomena, for example: water flow in saturated condition, thermal conductivity (Andrä et al., 2013), electrical conductivity (Miller et al., 2015), or solute diffusivity (Feng et al., 2017). These processes can be simulated in stationary conditions using numerical methods like finite differences (FD), finite volume (FV), lattice Boltzmann (LBM). The average of the numerical result allows to estimate the corresponding macroscopic property (permeability, thermal and electrical effective conductivity, effective diffusivity).

The branch of DRP faces two main obstacles. The first of them is that increasing the resolution of the image[1] enlarges the number of mesh elements, implying that a bigger computational power is required. The computation of fluid and particle transport is particularly demanding. A quantification of the effects of voxel size on computed parameters is thus needed. The second difficulty is related to the size of the image. In μCT the image resolution is inversely proportional to the size of the sample, i.e., the better is the resolution, the smaller the sample has to be (Wildenschild and Sheppard, 2013). This two restrictions associated with the necessity to

[1]The resolution of an image is considered to be the size of the image voxel. A higher resolution corresponds to a smaller voxel size

make computations in a REV, lead us to a fundamental constraint: The image could not be smaller than a REV, it should have a good resolution, and the mesh elements should not go beyond the computational limits. On top of that, the REV size depends on the measured property (Guibert et al., 2015a). Therefore, one of the problems to be evaluated in the present thesis is: What is the adequate X-ray CT scan resolution and sample volume allowing to derive a reliable macroscopic property? This question has been addressed by several authors concerning microstructural properties (Cooper et al., 2007; Lehmann et al., 2006; Al-Raoush et al., 2003). Some research is reported on the study of resolution effects on water flow properties (Borujeni et al., 2013; Yoon and Dewers, 2013), and less for the solute transport.

In this thesis it is proposed a criterion based on a structural property of a sandy soil to predict if a 3D image has an adequate resolution in order to compute in a reliable way the permeability via a FV method. It was developed an algorithm to compute the advection-diffusion transport directly into the soil microstructure . Numerical column experiments were then simulated in order to explore the dispersion effect in a large range of Peclet number. The averaged breakthrough curves were analyzed by an inverse procedure to compute the Dispersion coefficient and dispersivity of a granular material. The effect of CT resolution on the dispersion coefficient could then be discussed. As well as the effect of computing the macro properties of solute and flux transport on numerically rescaled images and images obtained at different CT resolution.

The thesis is divided as follows: Chapter 1 presents the fundamental concepts to understand the porous media structure characterization and the tools implemented in this thesis; in Chapter 2 the fundamental concepts to understand the flow and solute transport at the microscale are presented as well as the algorithm to solve advection diffusion transport; in Chapter 3 the fundamental concepts to understand the flow and solute transport at the macro scale are presented as well as the way the macroscopic quantities were computed; Chapter 4 is an accepted publication in the journal "Soil Research" where a criterion is proposed in order to determine if the resolution of an image is good enough for the computation of permeability using a FVM; Chapter 5 is an under submission publication where the algorithm here developed is presented and employed to study the effect of the image resolution on a solute transport experiment.

Chapter 1

Acquisition and characterization of the pore structure based on x-ray CT

It is possible to visualize the pore structure of a material through 3D images to study its morphology and flux processes occurring on it. Therefore, know the quality of a 3D image is a necessary first step before studying the transport problem. In this chapter we present the tools selected to the study of the porous media, and to define the resolution of the 3D image where we are going to compute the transport equations.

1.1 Principles of μCT

One of the techniques that allow to visualize the pore media structure is the micro computed tomography μCT. This method in a rough description, takes 2D radiographs of the sample and through a reconstruction process provides a 3D-image. These radiographs are taken with a X-ray CT scanner which generally consists of three common parts: an X-ray source, a sample manipulation device and a detector. Initially X-rays [1] are emitted from the

[1] X-radiation is a form of electromagnetic radiation, with wavelengths ranging from 0.01 to 10 nanometers, and energies in the range 100 eV to 100 keV. X-rays with wavelengths below 0.2-0.1 nm are called hard X-rays. And above 0.2-0.1 nm are called soft X-rays. Due to the similar size of atoms the hard X-rays are useful for example determining crystal

source and pass through the sample, where are progressively attenuated (see the Lambert-Beer's equation or Ketcham and Carlson (2001); Wildenschild and Sheppard (2013)). The X-rays that go through the object hit an X-ray sensitive screen. A digital camera is used to capture the image on the screen, which replicates the X-ray penetration pattern of the object Mooney et al. (2012).

1.2 Image processing

The product of a complete X-ray CT scan is a 3D matrix of relative attenuation values, sometimes called a data brick. After the reconstruction process, a 3D image stack is obtained as a discrete representation in gray scale. Its discrete 3D elements are called voxels, which normally are symmetric and their side size defines the spatial resolution of the 3D image (i.e. the smaller the voxels size is, the higher the resolution is Borujeni et al. (2013)). The total number of voxels mainly depends on the μCT apparatus sensor and the type of X-rays source.

Normally the image reconstructed presents artifacts, i. e., any error in the perception or representation of any visual information introduced by the involved equipment or technique. The most common artifacts are beam hardening, which causes the edges of an object to appear brighter than the center (while a poly-chromatic beam passes through an object, it will preferentially loss the lower energy parts of its spectrum, the resulting beam is a beam which has a higher average energy than the incident one), it can be reduced by pre-hardening the beam using a physical attenuating filter (aluminum, copper or brass), using smaller samples, and a correction during image reconstruction. Another common artifact is called the ring artifact. It occurs in scanners where the sample rotate, appearing as full or partial circles centered on the rotational axis. They are caused by shifts in output from individual detectors or sets of detectors, which cause the corresponding ray or rays in each view to have anomalous values; the position of a ring corresponds to the area of greatest overlap of these rays during reconstruction Ketcham and Carlson (2001).

structures by X-ray crystallography.

1.2.1 Filtering

Images are rarely perfect representations of the attenuation coefficients, since they are disturbed by optical transfer functions, scatter, and noise. Consequently, after reconstruction an image is usually filtered to reduce the noise level. The first filters that one encounters in the image processing literature are filters that have low-pass characteristics and are spatially invariant, like the Gaussian and the median filter. The effect of such filters is to smooth the image, affecting the sharp edged features in the image (Noise suppression as a part of the tomographic reconstruction has the same effect). Therefore, less processed images, which have been captured with an appropriate resolution should always be preferred in order to preserve both the finest details of the micro-structure and the quality of the data Kaestner et al. (2008); Mendoza et al. (2007).

1.2.2 Rescaling

A process that will be used in this study is called re-scaling or re-sizing it aims at increasing or decreasing the number of voxels in a 3D image. This process is not lossless. Re-scaling a volume to a smaller number of voxels, and then re-scaling it back to the original resolution, results in an image sightly different from the original one Danahy et al. (2007).

The re-scaling process can be divided conceptually into two processes: 3D interpolation of the discrete volume to a continuous volume and then sampling the interpolated volume to the desired resolution Parker et al. (1983). Various forms of interpolating functions have been developed. Reviews, and catalogs of methods can be found in Lehmann et al. (1999); Parker et al. (1983); Szeliski (2010); Grevera and Udupa (1996). In the present study, re-scaling will be use to decrease the resolution of the 3D image, decreasing the number of voxels in each direction. The ratio of this the new amount of voxels and the original amount of voxels per side is here called the re-scaling factor (RF). In other words an image with RF = 0.5 has a number of voxels in each direction which has decreased to the half of the original image. Where the original image has a RF of 1.

1.2.3 Segmentation

In order to compute morphological and transport properties of the sample, a distinction between solid phase and void phase should be performed. This process is called segmentation and aims at converting the gray scale into distinct phases, by identifying different populations in the image based on their intensity values. This process can be achieved through a variety of methods Dong and Blunt (2009); Steffen Schluter (2010). In Iassonov et al. (2009) an analysis of 14 segmentation methods is presented. In this study the segmentation was done in two phases: solid and void. The default Isodata algorithm of the software Imagej 2.34 was used. It performs a simple thresholding based on the histogram of the full 3D image. In Figure 1.1, a slice of the 3D image in gray scale and segmented is presented.

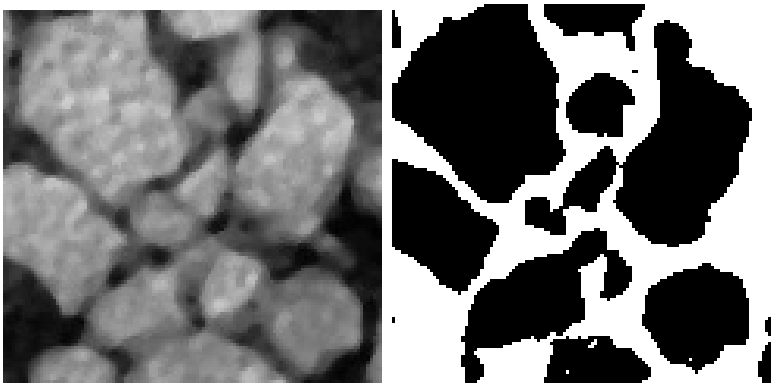

(a) Voxel size 4.5 μm, RF 1 (b) Voxel size 4.5 μm, RF 1

Figure 1.1: Example of a gray scale image segmented.

1.3 Computing morphological properties

Soil structure is the size, shape and arrangement of the solid particles and voids which is highly variable Letey (1991) and determines properties and process at physical, chemical and biological level occurring in the soil. For example the soil structure determines the air porosity, available water, permeability, diffusivity, activity of microorganisms. Nowadays with the improvement of the μCT and the image analysis, a new branch of the mathematics

has emerged to analyze and process geometrical structures of digital images, based on set theory, lattice theory, topology, and random functions. In this section the main soil structure parameters will be presented as well as the way they were computed.

1.3.1 Porosity

Porosity ϕ is the fraction of the bulk volume of the porous sample that is occupied by pore or void space Dullien (2012b),

$$\phi = \frac{V_{void}}{V_{Total}} = \frac{V_{Total} - V_{solid}}{V_{Total}} \ . \tag{1.1}$$

Depending on the type of porous medium, the porosity may vary from zero to one. Typically the sand porosity goes from 0.37 to 0.50 in contrast the limestone goes from 0.04 to 0.10 Nield et al. (2006b).

There are many experimental methods used to determine porosity some of them are mercury intrusion, gas expansion, water evaporation, inhibition. In general these methods measure the pore volume by measuring how much liquid, or gas can be contained in the soil sample, assuming it is occupying the void space, other methods like the direct one measures the bulk volume of a porous sample and then all the voids are destructed, measuring the volume of only the solids, having the disadvantage of a destructive method. With the image analysis technique the porosity can be computed counting the number of void voxels and dividing it over the total number of voxels of the image.

1.3.2 Specific surface

The specific surface, S_s, is the ratio between the surface between solid and void phases and the total volume. It is defined as:

$$S_s = \frac{S}{V_{Total}} \ , \tag{1.2}$$

where the surface S$[L^2]$ is the boundary between the solid and the void phases. A typical method to compute it numerically is based on counting

the number of voxel faces corresponding to a border. However this is a not converging method because as smaller is the voxel size the bigger is S. Instead here S was computed using the discrete extension in 3D of the integral geometry theorem of Cauchy-Crofton (see Do Carmo and Do Carmo (1976)). This method is based on counting the intersections of a surface, with lines spread parallel to 13 directions in all the 3D volume Santaló (2004); Legland et al. (2011); Lehmann and Legland (2012).

Specific surface via Cauchy-Crofton theorem

In the following paragraphs we will present the theorem in 3D, its discretization and how we implemented it in a code.

The theorem of Cauchy-Crofton computes the $d-1$ surface measure of the d-dimensional objects:

$$S^{d-1}(X) = \frac{d \cdot w_d}{w_{d-1}} \int_{\mathcal{L}^d} \chi(X \cap L) dL \ , \tag{1.3}$$

where w_d is the volume of the d-dimensional ball, $\mathcal{L}^d$ is the set of all lines the d-dimensional space, and $\chi(X \cap L)$ is the Euler Poincaré characteristic, which is equal to the number of connected components of the intersection of X (the studied object) with a line L, or equivalently half the number of intersections of the boundary of X with the line. The above integral is normalized such that the mass of lines hitting the unit ball equals w_{d-1}, the measure of the unit ball projection on a $(d-1)$-dimensional plane Lehmann et al. (2012). In the particular case of 3D it reduces to

$$S(X) = 4 \int_{\mathcal{L}^3} \chi(X \cap L) dL \ \ . \tag{1.4}$$

For the purpose of applying this theorem in the image analysis field, the Cauchy-Crofton formula is discretized in such a way that measurement of the Euler characteristics can be performed considering a finite number of lines L. The discretization of this theorem in 2D is clearly explained in Boykov and Kolmogorov (2003), and a more complex procedure is done for the 3D discretization (see Lang et al. (2001); Ohser and Mücklich (2000); Lehmann et al. (2012)):

$$S(x) \simeq 4 \sum_k \frac{C_k}{\lambda_k} \chi(X \cap L_k) \ , \tag{1.5}$$

where L_k is the finite set of 3D discrete lines parallel to direction k, λ_k the density of discrete lines in direction k, and C_k is the discretization weight associated to 3D direction k.

The weight C_k depends on the distances between e_k (the unitary direction k vector) and its neighbor directions. It can be approximated dividing the unit sphere Ω into the Voronoi cells with respect to the set of directions w_k. In this case 26 directions were chosen $\{w_k, k = 0, ..., 25\}$. The natural choice for C_k is the relative area of the corresponding Voronoi cell, $4\pi C_k$ the area of the kth Voronoi cell: $C_k = 0.045778$ for $C_k = 0, 1, 2$, $C_k = 0.036981$ for $k = 3, ..., 8$, and $C_k = 0.035196$ for $k = 9, ..., 12$ with $C_k = C_{k+13}$ (Lang et al. (2001); Ohser and Mücklich (2000)).

Something surprising of the Cauchy-Crofton formula is the small number of directions needed to have a surface value close to the real value. In the 2D case following the discretization of Boykov and Kolmogorov (2003), one can obtain good results computing perimeter of curves with few lines at only four directions (by hand computation). In the 3D case we chose to divide the space in a Cartesian grid (to later in the code match the discretization of the space with the discretization of the 3D image) and three families of direction were chosen:

- Parallel to the axis directions (family 1): (1,0,0), (0,1,0), (0,0,1)
- First diagonal (family 2): (1,1,0), (-1,1,0), (1,0,1), (-1,0,1), (0,1,1), (0,-1,1)
- Second diagonal (family 3): (1,1,1), (-1,1,-1), (1,1,-1), (-1,1,-1)

The complete set of directions includes also the negative of each family member i.e. all the directions of family 1 are: (1,0,0), (0,1,0), (0,0,1) and (-1,0,0), (0,-1,0), (0,0,-1). Making a total of 26 directions for the three families. Therefore, for the 26 directions Eq. (1.5) becomes:

$$\mathrm{S(x)} \simeq 4 \left(\frac{0.045778}{\lambda_1} \chi(X \cap L_1) + \frac{0.036981}{\lambda_2} \chi(X \cap L_2) + \frac{0.035196}{\lambda_3} \chi(X \cap L_3) \right) \ , \tag{1.6}$$

where $\lambda_k = \frac{|e_k|}{\delta^3}$ so, $\lambda_1 = \frac{1}{\delta^2}$, $\lambda_2 = \frac{\sqrt{2}}{\delta^2}$,$\lambda_1 = \frac{\sqrt{3}}{\delta^2}$ which correspond to family 1, 2 and 3 respectively. Thus, it is only missing to compute the intersections $\chi(X \cap L_k)$ which are associated to each family, and that is the main goal of the code developed for the specific surface computing.

Code implementation

The 3D image to analyze has to be previously segmented therefore, there are just to types of voxels (void or solid). In this situation a boundary void voxel, has at least one solid neighbors voxel. The neighbors voxels are classified in three types according to the families already studied.

For a given voxel (i, j, k),

- Neighbors family 1 are $(i+1, j, k)$, $(i, j+1, k)$, $(i, j, k+1)$, $(i-1, j, k)$, $(i, j-1, k)$, $(i, j, k-1)$.
- Neighbors family 2 are $(i+1, j+1, k)$, $(i-1, j-1, k)$, $(i-1, j+1, k)$, $(i+1, j-1, k)$, $(i+1, j, k+1)$, $(i-1, j, k-1)$, $(i-1, j, k+1)$, $(i+1, j, k-1)$, $(i, j+1, k+1)$, $(i, j-1, k-1)$, $(i, j-1, k+1)$, $(i, j+1, k-1)$.
- Neighbors family 3 are $(i+1, j+1, k+1)$, $(i-1, j+1, k-1)$, $(i+1, j+1, k-1)$, $(i-1, j+1, k+1)$.

In the C program we developed to compute the specific surface via the Cauchy-Crofton theorem, to find the intersections is simplified to count per direction how many voxels (i, j, k) present neighbor of different phase than itself.

To evaluate and understand the capacity of our method, we computed with the Cauchy-Crofton and the counting voxels methods, the surface area of three synthetic figures: a cylinder, a cube, and two spheres touching in a point. We calculated the error (difference between the real known surface value and the surface area computed via the method of Cauchy-Crofton and Counting voxels) and compared it with the radio of voxel size over the characteristic size of the figure. See Fig 4.9.

In all the cases the error using Cauchy-Crofton method(CCM) decreases as the radio $voxel\,size/R$ increases (R is the characteristic length of the

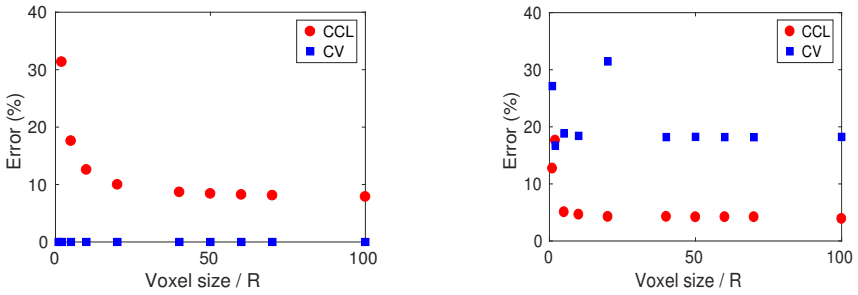

(a) Cube

(b) Cylinder.

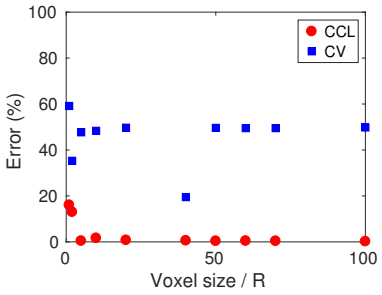

(c) Two spheres

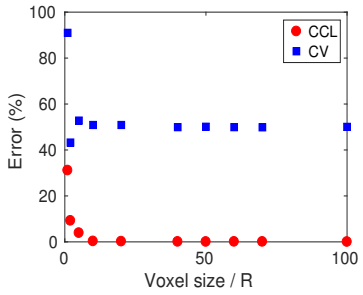

(d) One sphere

Figure 1.2: Error as a function of the adimensional quantity: voxel size over R, with R the characteristic length of the figure. CCL represents the Cauchy-Crofton method and CV represents the counting voxels method. Fig 1.2(a), Fig 1.2(b), Fig 1.2(c), and Fig 1.2(d) represent the case of a cube parallel to the 3D image mesh, a cylinder parallel to the 3D image mesh, two spheres touching each other in one point, and a sphere alone respectively.

figure). In all the cases except in the case of the cube, the accuracy of CCM is better than the counting voxels method (CCVM). In fact CCM shows a better behavior as more spherical is the figure. This result is related to the use of the Voronoi sphere as basis for discretization. While the CCVM is good only when the figure has square shapes following the orientation of the mesh.

1.3.3 PSD

The pore size distribution (PSD) is a common porous media property that classifies the porous phase into a set of discrete classes of pore size. Several methods have been proposed to compute the PSD of soils. Recently, Houston et al. (2017) presented a detailed comparison of existing methods implemented in commercial or free software (Maximum Inscribed Balls, morphological closing, object separation or skeleton computation). Based on its good performance for granular soils, the method of morphological closing was used in the current study following the pioneer work of Doughty and Tomutsa (1996) and Lin and Miller (2000). The first one analyzed the pore size and connectivity of Fontainebleau and Bentheim sand stones. And the second one studied the connectivity of the cake deposits in filtration processes. The method was applied on soils by Vogel and Roth (1998) and Vogel and Roth (2001) to study a German Orthic Luvisol or more recently by Muñoz-Ortega et al. (2015) to estimate the effect of tillage on soil structure.

The method here developed requires a segmented image, where one phase is defined as the background (normally the void space), the other as the foreground (normally the solid space), and a structural element (SE). In the case of PSD in a 3D image, a natural SE choice is a sphere of diameter D_i. The morphological operation to be applied is the closing over the solid phase with the chosen SE. This operation is the erosion of the resulting image after a dilatation, both operations using the same SE. The resulting image has a background where regions smaller than the SE have been removed, and in consequence the foreground is increased (for more details see Serra (1982); Wu et al. (2009); Goutsias and Batman (2000)).

In order to compute the PSD the closing operation is applied successively using increasing SE diameters D_i, resulting in a progressive reduction of the pore phase or pore volume (Fig. 1.3). At each closing step, the remaining pore volume is computed which corresponds to pores with diameter bigger or equal to D_i. The difference between the pore volume in the original image and the pore volume after the closing operation gives the volume associated to pores with diameter between 0 and D_i. This technique leads straightforward to the cumulative pore volume in function of the pore size diameter. It is finally presented as the percentage ratio of the total pore

volume.

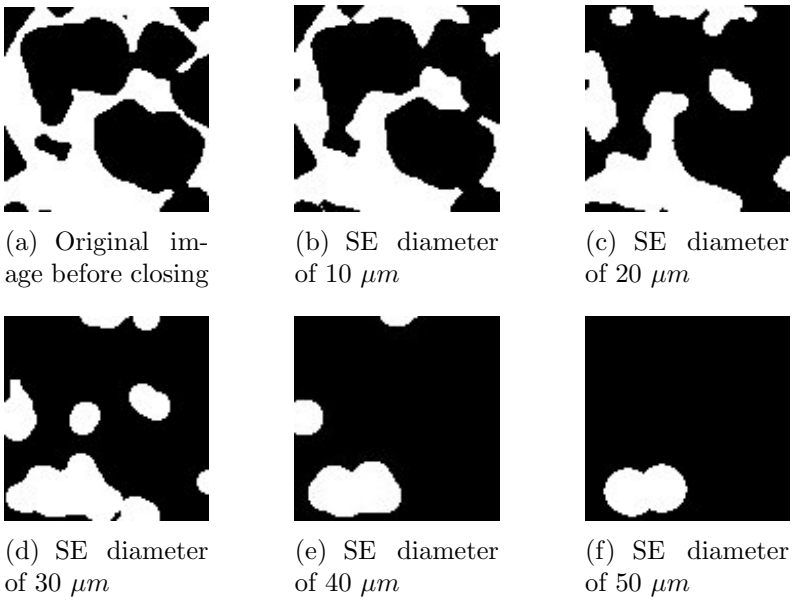

(a) Original image before closing

(b) SE diameter of 10 μm

(c) SE diameter of 20 μm

(d) SE diameter of 30 μm

(e) SE diameter of 40 μm

(f) SE diameter of 50 μm

Figure 1.3: Zoom on a square section of the Fontainebleau sand of an arbitrary slide for RF 1 (size: 540 μm): Progressive closing operation.

1.4 REV

To find the size, l, of the REV of a given property, there is the deterministic and the statistical method. The first one is implemented by taking a small volume, normally, centered within the sample, compute the property of interest and expand the volume in all directions. This process is repeated untill the property of interest remains constant Drugan and Willis (1996). This method is implemented in Costanza-Robinson et al. (2011) and Rozenbaum and du Roscoat (2014).

In order to find the statistical REV (SREV), different sets of sub-volumes are tested, the REV is achieved when the standard deviation of the distribution is small (or smaller than an arbitrarily value). Examples where this method

was implemented are Calonne et al. (2012) and Yoon and Dewers (2013).

Both the deterministic or the statistical REV depend on the property under consideration. It tends to be smaller for a geometric property (Porosity, specific surface) than for a flux property (permeability, diffusivity) Guibert et al. (2015b).

More precisely and the method followed in this thesis is described in Kanit et al. (2003), Zhang et al. (2000), Brown et al. (2000).

Chapter 2

Modelling flow and solute transport at the microscale

2.1 Introduction

The purpose of this section is to present the equations and properties that govern transport in porous media at a microscopic level. In particular we are interested in solving flow and transport equations directly on the pore structure. A mission that few years ago was even considered impossible ((Bear and Bachmat, 2012) page 3) due to the complexity of the geometry of the porous media. However, improvements have been done thanks to the detailed information provided by the μCT. Nevertheless, computational limitations are still present: like computational capacity which lead us to limitations of the volume size, or numerical diffusion.

2.2 Flow modelling

Fluid dynamics is the part of physics that study the motion of fluids (Landau and Lifshitz, 1959). To do it there are two ways to describe the fluid flows, the Lagrangian and the Eulerian. In the Lagrangian description, fixed pack of matter of fixed identity is defined as the system to study sys, and its properties are described as a function of time. In the Eulerian description, a fixed control volume V is defined, through which the fluid flows and the flow properties are described as fields within the control volume. Each property

is expressed as a function of space and time (more details see (Hauke, 2008)).

The link between the Eulerian and the Lagrangian description is the material or substantial derivative. It is a field quantity, i.e. it is expressed in the Eulerian frame of reference as a function of space and time (x,y,z,t). The material derivative of a variable is the rate at which that variable changes with time for a given particle.

To study conservative quantities in fluid Dynamics the Euler description is preferred, as it is difficult to identify and follow a system of fluid particles. Because the conservation laws of classic mechanics are in the Lagrangian version, a conversion has to be done. This conversion is done through the Reynolds theorem.

Reynolds transport theorem is used to compute derivatives of integrated quantities. To enunciate it, lets call B to any extensive property (like mass, momentum, volume) and b the intensive version of B therefore

$$b = B/m \ , \tag{2.1}$$

where m is the mass. B can be computed in the hole system as

$$B_{sys} = \int_{sys} \rho b dV \ , \tag{2.2}$$

with ρ the density. The Reynolds transport theorem for a non deforming control volume V states

$$\frac{DB_{sys}}{Dt} = \frac{\partial}{\partial t} \int_V \rho b dV + \int_S \rho b \mathbf{u} \cdot \hat{\mathbf{n}} dS \ , \tag{2.3}$$

which means that the time rate of change of B within the system equals to the rate of change of B within the control volume plus the net flux of B through the control volume boundaries.

Reynolds theorem is used in formulating the basic conservation laws of continuum mechanics, in the following sections we will make use of this theorem to present the mass and momentum conservation.

2.2.1 Mass balance

To use the Reynolds transport theorem to the mass conservation the quantities B and b must be identified. Being the mass the extensive quantity B then

$$B = m \qquad\qquad b = m/m = 1\,, \tag{2.4}$$

assuming there are no sinks and sources of mass in our system the substitution of m and 1 instead of B and b in Eq. (2.3) leads to

$$0 = \frac{\partial}{\partial t}\int_V \rho dV + \int_S \rho \mathbf{u}\cdot\hat{\mathbf{n}} dS\ . \tag{2.5}$$

This means that the change on time of mass within the control volume equals the rate of mass that enters and leaves the control volume.

Applying Green's formula to express the right term as a volume integral over V Eq. (2.5) can be written as

$$0 = \frac{\partial}{\partial t}\int_V \rho dV + \int_V \nabla\cdot(\rho\mathbf{u}) dV. \tag{2.6}$$

Since this equation holds for any volume, the integrand must vanish, i.e.

$$\frac{\partial \rho}{\partial t} + \nabla\cdot(\rho\mathbf{u}) = 0\ , \tag{2.7}$$

the vector quantity $\rho\mathbf{u}$ is known as the mass flux density $\mathbf{j}$. Its direction is that of the motion of the fluid, while its magnitude equals the mass of fluid flowing in unit time through unit area perpendicular to the velocity (Landau and Lifshitz, 1959).

Eq. (2.7) is the continuity equation for the mass density in absence of sources or sinks, in general when a property Γ is conserved it obeys the general conservation equation

$$\frac{\partial \Gamma}{\partial t} + \nabla\cdot\vec{\Omega} = G\ , \tag{2.8}$$

with Ω the flux vector in units of conserved property per unit time per unit area and G is the source/sink term with units of the property per unit time, which in all this study will be considered 0.

Coming back to Eq. (2.7), applying the divergence operator to the flux, it can be rewritten as

$$\begin{aligned}\rho\nabla\cdot\mathbf{u} &= -\,\mathbf{u}\cdot\nabla\rho - \frac{\partial\rho}{\partial t} \\ &= -\left(\mathbf{u}\cdot\nabla - \frac{\partial}{\partial t}\right)\rho \\ &= -\,\frac{D}{Dt}\rho\ ,\end{aligned} \tag{2.9}$$

where $\frac{D}{Dt}$ is know as the material or substantial derivative of a field quantity, i.e., it is expressed in the Eulerian frame of reference as a function of space and time (x,y,z,t), making a link between the Eulerian and the Lagrangian description.

For example, the material derivative of the velocity, $D\mathbf{u}/Dt = \mathbf{u}\cdot\nabla\mathbf{u} + \frac{\partial\mathbf{u}}{\partial t}$, does not simply denote the rate of change of fluid velocity at a fixed point. It is composed in two parts: $\frac{\partial\mathbf{u}}{\partial t}$ the change in time of the velocity at a point fixed in space is called the local or unsteady rate of change of $\mathbf{u}$. And $\mathbf{u}\cdot\nabla\mathbf{u}$ the difference between the velocities (at the same instant) at two points following a velocity field line. It is called the convective or advective rate of change of $\mathbf{u}$.

2.2.2 Momentum conservation

To apply the Reynolds transport theorem on the momentum conservation, the quantities B and b must be identified. Being the momentum $m\mathbf{u}$ the extensive quantity

$$B = m\mathbf{u} \qquad\qquad b = m\mathbf{u}/m = \mathbf{u}\ . \tag{2.10}$$

Substituting into Eq. (2.3)

$$\frac{Dm\mathbf{u}}{Dt} = \frac{\partial}{\partial t}\int_V \rho\mathbf{u}dV + \int_S \rho\mathbf{u}\mathbf{u}\cdot\hat{\mathbf{n}}dS\ . \tag{2.11}$$

Which means that the change in time of momentum within the system equals the change in time of momentum within the control volume plus the

momentum that crosses the boundary of the control volume.

Newton's second law states that the rate of change of the momentum, $\mathbf{p} = m\mathbf{u}$ is equal to the net force acting on the body $\mathbf{F}$. Depending on the phenomena studied the forces that can act on a control volume V may change, here only the superficial forces will be considered, they are pressure and the viscous forces. The total force due to the stresses is the sum of the stress vectors in all the control volume surface ((White, 1986),(Pedley, 1997) and (Landau and Lifshitz, 1959)).

$$\mathbf{F}_s = \int_{cs} \hat{\mathbf{n}} \cdot \sigma dS \ , \tag{2.12}$$

with $\hat{n}$ the unitary surface vector, and σ the stress tensor given by

$$\sigma = \begin{pmatrix} -p + \tau_{xx} & \tau_{yx} & \tau_{zx} \\ \tau_{xy} & -p + \tau_{yy} & \tau_{zy} \\ \tau_{xz} & \tau_{yz} & -p + \tau_{zz} \end{pmatrix} \ , \tag{2.13}$$

where p is the hydrostatic pressure acting in each face, and τ_{ij} and are the viscous stresses.

Following the second law of Newton from Eq. (2.11) and Eq. (2.12)

$$\frac{Dm\mathbf{u}}{Dt} = \frac{\partial}{\partial t}\int_V \rho\mathbf{u}dV + \int_S \rho\mathbf{u}(\mathbf{u}\cdot\hat{\mathbf{n}})dS = \int_S \hat{\mathbf{n}}\cdot\sigma dS \ . \tag{2.14}$$

Applying the divergence theorem to the surface integrals we obtain

$$\frac{\partial}{\partial t}\int_V \rho\mathbf{u}dV + \int_V \nabla\cdot(\rho\mathbf{u}\mathbf{u})dV = \int_V \nabla\cdot\sigma dV \ , \tag{2.15}$$

as it is valid for any kind of control volume

$$\frac{\partial}{\partial t}\rho\mathbf{u} + \nabla\cdot(\rho\mathbf{u}\mathbf{u}) = \nabla\cdot\sigma \ , \tag{2.16}$$

where $\mathbf{uu}$ is a dyadic product, a second rank tensor. The divergence of a second rank tensor is first order tensor field $(\nabla\cdot(\mathbf{ab}) = (\nabla\cdot\mathbf{a})b + \mathbf{a}\cdot\nabla\mathbf{b})$

$$\frac{\partial\rho}{\partial t}\mathbf{u} + \frac{\partial\mathbf{u}}{\partial t}\rho + (\nabla\cdot\rho\mathbf{u})\mathbf{u} + \rho\mathbf{u}\cdot\nabla\mathbf{u} = \nabla\cdot\sigma \ . \tag{2.17}$$

Regrouping

$$\left(\frac{\partial \rho}{\partial t} + \nabla \cdot \rho \mathbf{u}\right) \mathbf{u} + \left(\frac{\partial \mathbf{u}}{\partial t} + \mathbf{u} \cdot \nabla \mathbf{u}\right) \rho = \nabla \cdot \sigma \ . \tag{2.18}$$

If the mass is conserved then

$$\left(\frac{\partial \mathbf{u}}{\partial t} + \mathbf{u} \cdot \nabla \mathbf{u}\right) = \nabla \cdot \sigma \ , \tag{2.19}$$

which can be written in terms of the material derivative of velocity

$$\rho \frac{D\mathbf{u}}{Dt} = \nabla \cdot \sigma \ . \tag{2.20}$$

For a Newtonian fluid incompressible the viscous stress tensor elements σ_{ij} are proportional to the element strain rates and the coefficient of viscosity this is $\tau_{ij} = \mu \left(\frac{\partial v_i}{\partial j} + \frac{\partial v_j}{\partial i}\right)$ where μ is the dynamic viscosity of the fluid. Substituting in Eq. (2.20)

$$\rho \frac{D\mathbf{u}}{Dt} = -\nabla P + \mu \nabla^2 \mathbf{u} \ . \tag{2.21}$$

These are the incompressible Navier-Stokes equations. They are 3 second-order nonlinear partial differential equations governing four unknowns P and the three components of $\mathbf{u}$. To solve them it should be considered the incompressible continuity relation$\nabla \cdot \mathbf{u} = 0$ and the appropriate boundary conditions.

Even though the Navier-Stokes equations have only a limited number of known analytical solutions, numerical solutions can be founded and in this thesis the GeoDict software is implemented to solve them into the 3D images of the sand obtained from the μCT.

Stokes equation

Flow can be better understood based on the characteristic dimensions where it occurs. In this sense, the Reynold's number, Re, is used as a criterion to distinguish between laminar flow occurring at low velocities and turbulent

flow occurring at velocities. It is defined as the ratio between inertial and viscous forces:

$$\begin{aligned} Re &= \frac{Inertial \quad forces}{Viscous \quad forces} \\ &= \frac{\rho u l}{\mu} \ , \end{aligned} \tag{2.22}$$

where ρ, u, μ, l correspond to the characteristic dimensions of the phenomena: density, velocity, dynamic viscosity, and length (Adler, 2013). In porous media

$$Re = \frac{u d_p}{\nu} \ , \tag{2.23}$$

where u is the maximum pore velocity, d_p is the size of the pore where the 50% of the flux occurs[1], and ν is the kinematic viscosity of the fluid. At low Re, there is a region where the flow is creeping, meaning that the viscous forces are predominant, and as long as Re does not exceed some value between 1 and 10 the Darcy's law is valid (Bear, 1988, 1979). As Re increases, there is a transition zone. At this region the flow is still laminar but not linear. And at high Re the flow is turbulent.

Writing Eq. (2.21) in terms of the dimensionless quantities that are indicated by primes:

$$\mathbf{x} = l\mathbf{x}', \quad \mathbf{u} = u\mathbf{u}', \quad t = \frac{l}{u}t', \quad P = \frac{\mu u}{l}P' \tag{2.24}$$

we obtain

$$Re\frac{D\mathbf{u}'}{Dt'} = -\nabla' P' + \nabla'^2 \mathbf{u}'. \tag{2.25}$$

When the inertia term is neglected, the Navier-Stokes equations reduce to

$$-\nabla' P' + \nabla'^2 \mathbf{u'} = 0 \ , \tag{2.26}$$

which is known as the Stokes equation and is generally suitable to describe flow in porous media at low Re.

[1]The value can be computed using the distribution of flow proposed in(Ramírez et al.).

2.2.3 Numerical modelling on velocity and pressure fields

To compute the velocity field a commercial software was used its name is GeoDict and it comes from the abbreviation for Geometric material designer and material property preDictor. It describes itself as a complete solution for multi-scale 3D image processing, modeling of materials, visualization, material property characterization, simulation-based material development, and optimization of processes (www.geodict.de). GeoDict was chosen because it offers a finite volumes solver for a fast and accurate numerical solution of the Stokes equation via its module FlowDict. On this module the option called Explicit Jump Stokes solver (Wiegmann and Bube, 2000b) was implemented. The module FlowDict uses a cubic mesh conformed to the image voxels. It computes the three components of the velocity vector $\vec{u}$ and the pressure P in each voxel on a staggered grid. The Stokes problem (Eqs. (4.3) and (4.4)) is decomposed into four Poisson problems solved iteratively using a Fast Fourier Transform based algorithm (Wiegmann, 2007) An explicit jump approach of the immersed boundary concept is used to force the no-slip boundary condition as suggested by (Rutka, 2008). A relative error of 10^{-3} on the computed permeability was set as convergence criterion.

The EJ solver was complemented by the inflow and outflow conditions of pressure, lateral and tangential periodic boundary conditions. To do it the discretization is done by means of a finite difference method. Resulting a velocity and pressure fields. The EJ solver is recommended for this kind of experiment due that it is very fast for highly porous materials.

2.3 Solute transport modelling

2.3.1 Solute conservation

The last conservative quantity that is going to be presented here, is the solute concentration $c = c(\mathbf{x}, t)$, which represents the number of solute present in a control volume V. Following the same formalism derived in section 2.2.1,

the local equation governing the concentration field is given by

$$\frac{\partial}{\partial t}\int_V c dV + \int_S \mathbf{j}_c \cdot \hat{\mathbf{n}} dS \ , \tag{2.27}$$

with $\mathbf{j}_c$ the solute flux. Applying the divergence theorem in the surface integral, and because it holds for any volume we obtain

$$\frac{\partial c}{\partial t} + \nabla \cdot \mathbf{j}_c = 0 \ , \tag{2.28}$$

where $\mathbf{j}_c$ is the total flux of solute through the surface of V element and is equal to the sum of the diffusion flux and the advective flux that is $\mathbf{j}_c = \mathbf{j}_{diff} + \mathbf{j}_{adv}$. Given the linearity of the equation these are two phenomena that can be treated separately. Thus in the following paragraphs we will present the diffusion and the advection phenomena. Always assuming that we are in a situation of no creation or destruction of solute.

In the absence of flow, the flux is just due to diffusion and obeys an empirical formulation done by Adolph Fick in 1855 (Fick, 1855)

$$\mathbf{j}_{diff} = -D_0 \nabla c \ . \tag{2.29}$$

This equation states that the flux of solute mass is proportional to the gradient of solute concentration. The minus sign holds the fact that the solute flux goes from the regions with more concentration to the region with less concentration. The diffusion coefficient D_0 is a positive constant dependent on molecule size and other properties of the diffusing substance like the temperature and pressure is positive with units L^2/T it depends on the temperature which in this study is considered to be constant. A typical value of D_0 for small ions in water is $D_0 = 2 \times 10^{-9} m^2/s$.

Introducing Fick's law into the conservation Eq. (2.28), the local conservation law is reduced to the diffusion conservation equation

$$\frac{\partial c}{\partial t} - \nabla \cdot (D_0 \nabla c) = 0 \ . \tag{2.30}$$

In the presence of flow, the fluid with its motion, drags the solute and its properties. This phenomena is called advection. Physically it is not possible

to avoid the diffusion effects, but theoretically it is possible, in that case the flux is $\mathbf{j}_c = \mathbf{j}_{adv}$, the advective flux and it is given by

$$\mathbf{j}_{adv} = \mathbf{u}c \ . \tag{2.31}$$

Introducing the advective flux into the conservation equation we obtain the advection conservation equation.

$$\frac{\partial c}{\partial t} - \nabla \cdot \mathbf{u}c = 0 \ . \tag{2.32}$$

Taking Eq. (2.30) and Eq. (2.32) into Eq. (2.28) we obtain the advection diffusion equation (ADE)

$$\frac{\partial c}{\partial t} - \nabla \cdot \nabla D_0 c + \nabla \cdot \mathbf{u}c = 0 \ . \tag{2.33}$$

Peclet number

Similar to Section 2.2.2, doing an adimensional analysis of the diffusion advection equation, a dimensionless number can be defined which relates the advective transport rate with the diffusive transport rate. This is the Peclet number given by:

$$\begin{aligned} Pe &= \frac{Advective \quad transport \quad rate}{diffusive \quad transport \quad rate} \ , \\ &= \frac{ul}{D_0} \ , \end{aligned} \tag{2.34}$$

where u, l, D are the characteristic dimensions of the phenomena. If the Pe number is much smaller than 1, diffusion dominates over advection and transport may be modeled considering diffusion only. Up to 10 different Pe number definitions exist and for a particular case these different definitions lead to very diverse Pe number values, differing several orders of magnitude from each other (Huysmans and Dassargues, 2005). In porous media at the pore scale and particularly in this study, the microscale Pe number will be defined as

$$Pe = \frac{uD_{50}}{D_0} \ , \tag{2.35}$$

where v is the average pore velocity, D_{50} is the average of the solid phase particle size and, D is the diffusion coefficient (Dullien, 2012a).

2.3.2 Development of a transport code

FV and the time split operator

To solve the ADE Eq. (2.33) the operator splitting is used. This is a method commonly used in the solution of linear or non-linear partial differential equations which complexity makes difficult to find a solution accurate enough for a reasonable time step. The main idea of this method is to decouple the equation into simpler equations and solve them separately with a method *ad hoc* to them. The splitting method here implemented splits the time evolution into partial steps to separate the physical process of convection and diffusion. The cost of this splitting is an error which is zero if the operators of the new equations commute (more on splitting operators can be find in Tanoğlu et al. (2010); Csomós et al. (2005)). This method is a common process while solving the ADE problem (see for example (Zaretskiy et al., 2010b)). Applying the splitting operator to Eq. (2.33) results in the sum of the advective and the diffusion process in one step time. Allowing us to use the most convenient method for each physical process.

To solve the advection and diffusion problem separately, the finite volume method (FVM) was used for both cases, with an adequate scheme for each case.

The FVM is a popular method to solve conserved PDE. It consists in dividing the solution domain into a finite number of control volumes. The local solution is defined in the center of the finite volume as the average of the conserved quantity into the finite volume which is updated by approximations to the flux through each edge of the finite volume.

An interesting feature of FVM is that the mesh is not obliged to be Cartesian. However, in this study and as is typically done while studying 3D images we will associate each finite volume to a voxel of the 3D image (for example see (Bijeljic et al., 2013a; Yang et al., 2016b)).

Boundary conditions

Two types of boundary conditions were implemented in the program

- Dirichlet BC: it imposes a fixed value of the concentration. In the discretized space, it is imposed in the center if the voxel under

consideration. It generally concerns the inlet face of the VOI with a value of 1 during the solute injection and 0 otherwise.

- Neumann BC (or second type): it imposes a value on the derivatives. Particularly the condition set here is $\nabla c \cdot \hat{\mathbf{n}} = 0$ meaning that there is no flux in the direction normal to the boundary. This condition in the advection case is straightforward imposed due to the fact that the velocity is zero in the solid voxels. In the diffusion case was used in each voxel in function of the existence of some of its neighbours be a solid. Setting in the diffusion matrix the corresponding coefficient A_x and/or A_y and/or A_z equal to 0 (see Eq. (2.50)). This condition is also applied in the lateral face of the VOI to mimic a periodic BC and limit the spreading of the diffusion matrix. It is also used at the outlet face of the VOI since a free flow BC (or purely advective BC) is selected.

Diffusion model

After the splitting operator was applied we can solve separately the problem of pure diffusion and later the problem of only advection. Let's start with the pure diffusion.

$$\frac{\partial c}{\partial t} = D_0 \nabla^2 c \ . \tag{2.36}$$

Which in integral form is

$$\int_V \frac{\partial c}{\partial t} dv = \int_V D_0 \nabla^2 c dv \ , \tag{2.37}$$

where dv is a control volume with center at ijk. Assuming the grid is not changing with time the temporal derivative of the l.h.s. can go out of the spatial integral, and applying the divergence theorem[2] to the r.h.s. yields to

$$\frac{\partial}{\partial t} \int_V c dv = \oint_S D_0 (\nabla c \cdot \hat{\mathbf{n}}) ds \ . \tag{2.38}$$

[2]The divergence theorem or Gauss's theorem states that the outward flux of a tensor field through a closed surface is equal to the volume integral of the divergence over the region inside the surface. $\int_V (\nabla \cdot \mathbf{F}) dv = \oint_S (\mathbf{F} \cdot \mathbf{n}) ds$

The left hand side (l.h.s.) can be written in terms of the average concentration on the grid element[3]. The r.h.s. is now an integral over a closed surface, $\hat{\mathbf{n}}$ is the outer pointing unit normal vector defined at each point on the cell interface. Since our cell has 6 flat faces $\hat{\mathbf{n}}$ takes 6 different values, thus the right hand side (r.h.s.) can be written as a sum of integrals where λ counts for each normal vector of the surface.

$$\Delta x \Delta y \Delta z \frac{\partial c_{i,j,k}}{\partial t} = \sum_{face_\lambda}^{6} \int_{S_\lambda} D_0 (\nabla c \cdot \hat{\mathbf{n}}_\lambda) ds \ . \tag{2.39}$$

Notice that c_{ijk} does not depend of any particular point inside the cell, thus the partial temporal derivative can be exchanged for a total time derivative.

$$\Delta x \Delta y \Delta z \frac{dc_{i,j,k}}{dt} = \sum_{face_\lambda}^{6} \int_{S_\lambda} D_0 (\nabla c \cdot \hat{\mathbf{n}}_\lambda) ds \ . \tag{2.40}$$

It can be noticed that $D_0 \nabla c$ is the vector flux $\mathbf{j}_{diff}$ due to diffusion, therefore the integral in each face is the flux between two adjacent grid elements in the direction of the normal vector of the face at the face center. Using the average concentration at the grid element i, j, k and it neighbors, the flux will be computed at the center of each face and multiplied by its area. For the face 1 (see Fig. 2.1) the integral of the flux will be given by:

$$\int_1 = \int_{S_1} D_0 (\nabla c_{i,j,k} \cdot \mathbf{n}_1) ds = \frac{Do \Delta y \Delta z}{\Delta x} c_{i,j,k} - c_{i+1,j,k} \ . \tag{2.41}$$

Similar for the remaining 5 integrals. Attention must be paid due to the

[3] c_{ijk} is the average value of c into the grid given by $(\int_V c dv)/dv$ where $dv = \Delta x \Delta y \Delta z$ is the grid volume

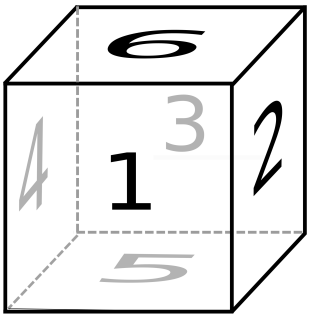

Figure 2.1: Grid element showing the faces setting where the flux is going to be computed.

direction of the flux and the surface normal vector.

$$\int_2 = \int_{S2} D_0(\nabla c \cdot \mathbf{n}_2) ds = \frac{Do\Delta y\Delta z}{\Delta x} c_{i,j,k} - c_{i+1,j,k} \tag{2.42}$$

$$\int_3 = \int_{S3} D_0(\nabla c \cdot \mathbf{n}_3) ds = \frac{Do\Delta x\Delta y}{\Delta z} c_{i,j,k} - c_{i,j,k+1} \tag{2.43}$$

$$\int_4 = \int_{S4} D_0(\nabla c \cdot \mathbf{n}_4) ds = \frac{Do\Delta y\Delta z}{\Delta x} c_{i,j,k} - c_{i-1,j,k} \tag{2.44}$$

$$\int_5 = \int_{S5} D_0(\nabla c \cdot \mathbf{n}_5) ds = \frac{Do\Delta x\Delta z}{\Delta y} c_{i,j,k} - c_{i,j-1,k} \tag{2.45}$$

$$\int_6 = \int_{S6} D_0(\nabla c \cdot \mathbf{n}_6) ds = \frac{Do\Delta x\Delta z}{\Delta y} c_{i,j,k} - c_{i,j+1,k} \ . \tag{2.46}$$

Therefore the r.h.s. of Eq. (2.39) is the sum of $\int_1$ to $\int_6$ representing the flux going out the cell. Till now we have a semi-discrete equation. To discretize the temporal part, it was chosen an implicit scheme. On this kind of schemes the numerical solution depends upon the values of c at both old and new time steps. Differently of an explicit scheme, an implicit scheme is unconditionally stable, and it is expressed as

$$\frac{\partial c_{i,j,k}^{t+1}}{\partial t} = \frac{c_{i,j,k}^{t+1} - c_{i,j,k}^{t}}{\Delta t} \ . \tag{2.47}$$

Here the upper index count for the time and the lower for the position.

Therefore Eq. (2.40) can be written as

$$c_{i,j,k}^{t+1} - c_{i,j,k}^{t} = \frac{\Delta t}{\Delta x \Delta y \Delta z} \sum_{\lambda}^{6} \int_{\lambda} \ . \tag{2.48}$$

Eq. (2.48) can rewritten as

$$\begin{aligned} c_{i,j,k}^{t} = \mathcal{B} c_{i,j,k}^{t+1} &- \mathcal{A}_x c_{i-1,j,k}^{t+1} - \mathcal{A}_x c_{i+1,j,k}^{t+1} \\ &- \mathcal{A}_y c_{i,j-1,k}^{t+1} - \mathcal{A}_y c_{i,j+1,k}^{t+1} \\ &- \mathcal{A}_z c_{i,j,k-1}^{t+1} - \mathcal{A}_z c_{i,j,k+1}^{t+1} \ , \end{aligned} \tag{2.49}$$

where

$$\mathcal{A}_x = \frac{D_0 \Delta t}{\Delta x^2}; \qquad \mathcal{A}_y = \frac{D_0 \Delta t}{\Delta y^2}; \qquad \mathcal{A}_z = \frac{D_0 \Delta t}{\Delta z^2}; \tag{2.50}$$

$$\mathcal{B} = 1 - 2\mathcal{A}_x - 2\mathcal{A}_y - 2\mathcal{A}_z \ . \tag{2.51}$$

The discretized diffusion equation for all the 3D space, is a system of equations with Eq. (2.49) as the corresponding equation to each element of the grid. In order to write this system in a matrix form, a linearization of the ijk indexes was done (congruence most exist between this linearization and the order at allocating the volume in the code).

$$c_{ijk} \rightarrow c_{\alpha} = c_{(j-i)N_z + (i-1)N_z N_y + k} \ . \tag{2.52}$$

This means that we are filling first in the i direction, secondly in the j direction and finally in the k direction The system of equations of diffusion in all the space yields to the linear system of equations in matrix form

$$\mathbf{A}\mathbf{c}^{t+1} = \mathbf{c}^{t} \ , \tag{2.53}$$

where

$$\mathbf{c}^{t} = \begin{pmatrix} c_1^t \\ c_2^t \\ \vdots \\ c_{\alpha}^t \\ \vdots \\ c_{N_x N_y N_z}^t \end{pmatrix} \tag{2.54}$$

$$\mathbf{A} = \begin{bmatrix} \mathcal{B} & -\mathcal{A}_z & & -\mathcal{A}_y & & -\mathcal{A}_x & & & \\ -\mathcal{A}_z & \mathcal{B} & -\mathcal{A}_z & & -\mathcal{A}_y & & -\mathcal{A}_x & & \\ & -\mathcal{A}_z & \mathcal{B} & -\mathcal{A}_z & & -\mathcal{A}_y & & -\mathcal{A}_x & \\ -\mathcal{A}_y & & -\mathcal{A}_z & \mathcal{B} & -\mathcal{A}_z & & -\mathcal{A}_y & & -\mathcal{A}_x \\ & -\mathcal{A}_y & & -\mathcal{A}_z & \mathcal{B} & -\mathcal{A}_z & & -\mathcal{A}_y & \\ -\mathcal{A}_x & & -\mathcal{A}_y & & -\mathcal{A}_z & \mathcal{B} & -\mathcal{A}_z & & \\ & -\mathcal{A}_x & & -\mathcal{A}_y & & -\mathcal{A}_z & \mathcal{B} & -\mathcal{A}_z & \\ & & -\mathcal{A}_x & & -\mathcal{A}_y & & -\mathcal{A}_z & \mathcal{B} \end{bmatrix} . \tag{2.55}$$

The matrix $\mathbf{A}$ is a $N_x N_y N_z \times N_x N_y N_z$ spare matrix with 7 non zero diagonals. There are N_z spaces between the diagonals $\mathcal{B}$ and $-\mathcal{A}_y$, and $N_z N_y$ spaces between the diagonals $\mathcal{B}$ and $-\mathcal{A}_x$. The elements of these diagonals depend of the nature of the evaluated mesh element and the chosen boundary conditions.

If the mesh element corresponding to the index $ijk \rightarrow \alpha$ is pore, then the element of the matrix $\mathbf{A}_{\alpha\alpha}$ is non zero and equal to $\mathcal{B}$ (2.51), as in Section 2.3.2 was explained Neumann boundary condition were chosen for diffusion. And here it is translated to set zero to the elements of the row α if it correspond to a solid neighbor. For example: if the only solid neighbor is the one with center at $i+1, j, k$, then the elements of the row α will take its values as indicated in Eq. (2.50) except for the element at $\mathbf{A}_{\alpha\alpha} = 1 + \mathcal{A}_x + 2\mathcal{A}_y + 2\mathcal{A}_z$ and the element $\mathbf{A}_{\alpha+N_y N_z,\alpha} = 0$.

Given the big size of the matrix system Eq. (2.53) a solver has to be implemented. In general there are many solvers focused on solve linear systems containing spar matrices, some of them are PaStiX, SuperLU, Eigen. In this study we chose the package called MUMPS (MUltifrontal Massively Parallel Solver) it was specially designed to solve linear equations like Eq. (2.53) with a A a spare square matrix on parallel computers, using a multifrontal method. It was written in FORTRAN 90 and uses MPI for message passing (for more details see (Amestoy et al., 1998)). The frontal method is based in a Gaussian elimination or LU decomposition. Which consists on factorizing the matrix $\mathbf{A}$ into a lower and upper matrix

$$\mathbf{A} = \mathbf{L}\mathbf{U} \ . \tag{2.56}$$

Rewriting the system Eq. (2.53)

$$\mathbf{L}\mathbf{U}\mathbf{c}^{t+1} = \mathbf{c}^{t} \ , \tag{2.57}$$

renaming

$$\mathbf{U}\mathbf{c}^{t+1} = \mathbf{x} \ , \tag{2.58}$$

simplifies (2.57)

$$\mathbf{L}\mathbf{x} = \mathbf{c}^{t} \ , \tag{2.59}$$

solving last equation for $\mathbf{x}$ it can be substituted in Eq. (2.58) to finally solve for $\mathbf{c}^{t+1}$. Following these steps, approximately $\frac{N_x N_y N_z^3}{3}$ operations are required, while the classical method of Gauss-Jordan requires approximately $N_x N_y N_z^3$ operations. We chose to decompose the matrix once during all the ADE computation.

Advection model

After the splitting operator was applied, the advection equation part is given by

$$\frac{\partial c}{\partial t} = -\mathbf{u} \cdot \nabla c \ , \tag{2.60}$$

which integral form is

$$\int_V \frac{\partial c}{\partial t} dv = -\int_V \mathbf{u} \cdot \nabla c dv \ , \tag{2.61}$$

and in the 1D case choosing the direction of the water flow, x, the integral advection part can be written as

$$\int_{x_{i-1/2}}^{x_{i+1/2}} \frac{\partial c}{\partial t} dx = -\int_{x_{i-1/2}}^{x_{i+1/2}} u_x \frac{\partial c}{\partial x} dx \ . \tag{2.62}$$

Using the mean value theorem and remembering the the advective flux expression Eq. (2.31), Eq. (2.62) could be rewritten in the semi-discrete form as:

$$\Delta x_i \frac{\partial c_i}{\partial t} = -[j^t_{adv_{i+1/2}} - j^t_{adv_{i-1/2}}] = 0 \ . \tag{2.63}$$

By taking a first order scheme in time

$$\frac{1}{\Delta t}(c_i^{t+1} - c_i^t) = -\frac{1}{\Delta x_i}[j^t_{adv_{i+1/2}} - j^t_{adv_{i-1/2}}] \ . \tag{2.64}$$

The fact that the advection equation is a conservation equation means that c_i can only be modified by exchanges with the neighboring cells. Therefore,

the change in c_i can be seen as in- and out- fluxes through the cell interfaces. Therefore $j^t_{adv_{i+1/2}}$ and $j^t_{adv_{i-1/2}}$ are the flux at the cell interface at time t.

Many methods have been proposed to approximate the solution of Eq. (2.64), however it is well known that linear schemes in time are strongly affected by numerical diffusion (Fanchi et al., 1983; Lantz et al., 1971) while high order schemes in time (≥ 2), which have been successful in eliminating the numerical diffusion, give rise to non physical oscillations near regions of large gradients (jumps) (Patel et al., 1985).

A solution is to build an hybrid method where a high order numerical scheme changes to a low order scheme depending on some critical conditions like a steep gradient or a discontinuity. This condition is imposed by a flux limiter. Lets define the flux as a combination of high and low order fluxes as

$$j_{adv\, i+1/2} = j^L_{adv\, i+1/2} + \Psi_{i+1/2}\left(j^H_{adv\, i+1/2} - j^L_{i+1/2}\right) \ , \tag{2.65}$$

where $j^H_{adv\, i+1/2}$ is the high order numerical flux, $j^L_{adv\, i+1/2}$ is the low order numerical flux and $\Psi_{i+1/2}$ is the flux limiter. Which in function of the neighbor solutions allows the flux be high or low order. Therefore, the limiter $\Psi_{i+1/2}$ depends locally on a nonlinear function Θ_{i+1}, which is the ratio of solution slopes at the neighborhood of the interfaces in the upwind direction.

$$\Theta^t_{i+1/2} = \begin{cases} \frac{c^t_i - c^t_{i-1}}{c^t_{i+1} - c^t_i} = \Theta^+_{i+1/2} & \text{if } u^t_{i+1/2} \geq 0 \\ \frac{c^t_{i+2} - c^t_{i+1}}{c^t_{i+1} - c^t_i} = \Theta^-_{i+1/2} & \text{if } u^t_{i+1/2} < 0 \end{cases} . \tag{2.66}$$

The limiter function is constrained to be greater or equal to zero, i.e., $\Psi(\Theta) \geq 0$. Therefore, when the limiter is equal to zero (sharp gradient, opposite slopes or zero gradient), the flux is represented by a low resolution scheme. Similarly, when the limiter is equal to 1 (smooth solution), it is represented by a high resolution scheme. Then different propositions of limiters exist, some of them are:

$$Minmod: \ \Psi(\Theta) = max(0, min(1, \Theta)) \tag{2.67}$$

$$Superbee: \ \Psi(\Theta) = max(0, min(1, 2\Theta), min(2, \Theta)) \tag{2.68}$$

$$VanLeer \ \Psi(\Theta) = (0 + |\Theta|)/(1, |\Theta|)) \tag{2.69}$$

$$MUSCL: \ \Psi(\Theta) = max\left(0, min\left(\frac{1+\Theta}{2}, 2, 2\Theta\right)\right) \tag{2.70}$$

More details about these limiters can be found in (Durran, 2010).

The purpose of the flux limiters method is to avoid the creation of oscillations in the solution or diffusion, to guarantee this property, (Harten, 1983) introduced a property of quantity Q specified in a numerical grid, called the total variation (TV) of the solution at a given time which is given by

$$TV(Q^t) = \sum_{i=1}^{N} |Q_{i+1}^t - Q_i^t| \ , \tag{2.71}$$

where $i = 1$ and $i = N$ are the left and right boundaries of the numerical grid respectively. For a monotonically increasing function Q the $TV(Q) = |Q_{i+1} - Q_i|$. To prevent the system from developing nonphysical maxima or minima, this must remain constant or decreasing over each time step. Then a numerical scheme is said to be TVD (total variation diminishing) if:

$$TV(Q^{t+1}) \leq TV(Q^t) \ . \tag{2.72}$$

Methods which satisfy TVD criteria also preserve monotonicity of solutions. A scheme is monotone if given $Q_i^t \geq Q_{i+1}^t$ then $Q_i^{t+1} \geq Q_{t+1}^{t+1}$. Pure second order methods cannot be monotone, therefore the goal is to use the flux limiters to control the inclusion of higher order terms, creating schemes with greater than first order accuracy, while preserving TVD (for more details see (LeVeque, 2002; Cox and Nishikawa, 1991))

Once the limiter has been chosen, the missing decision is the way the flux is going to be computed into the cell. The multidimensional upstream centered scheme for conservation laws (MUSCL) proposed by (Van Leer, 1979), assumes that the state into the cell is a linear or high order function. In this study a linear function is considered which computes the state in the cell as

$$c(x,t) = c_i(t) + S_i(t)(x - x_i) \quad x \in [(i - 1/2)\delta x, (i + 1/2)\delta x] \ , \tag{2.73}$$

where $[(i-1/2)\delta x, (i+1/2)\delta x]$ is the interval in between the cell (for a regular cell otherwise it would be $x \in [x_i - \delta x/2, x_i + \delta x/2]$) and $S_i(t)$ is a slope function of the average values of the neighbor cells and itself. A priori the function is discontinuous at the faces of the cell therefore two values $c_{i\pm1/2}^t$ are defined in each face $x_{i+1/2}$. As can be seen in (Dubois, 2010), a convenient

scheme can be defined as:

$$c_{i+1/2}^t = \begin{cases} c_i^t + \frac{1}{2}(c_{i+1}^t - c_i^t)\Psi(\Theta_{i+1/2}^+) & u_{i+1/2}^t \geq 0 \\ \\ c_{i+1}^t - \frac{1}{2}(c_{i+1}^t - c_i^t)\Psi(\Theta_{i+1/2}^-) & u_{i+1/2}^t < 0 \ , \end{cases} \tag{2.74}$$

$$c_{i-1/2}^t = \begin{cases} c_{i-1}^t + \frac{1}{2}(c_i^t - c_{i-1}^t)\Psi(\Theta_{i-1/2}^+) & u_{i-1/2}^t \geq 0 \\ \\ c_i^t - \frac{1}{2}(c_i^t - c_{i-1}^t)\Psi(\Theta_{i-1/2}^-) & u_{i-1/2}^t < 0 \ . \end{cases} \tag{2.75}$$

This are the arguments that should be taken into the flux evaluated in the faces of Eq. (2.64) and using Eq. (2.31) and Eq. (2.75) it can be written as

$$c_i^{t+1} = c_i^t - A_{i-1/2}^t(c_i^t - c_{i-1}^t) + B_{i+1/2}^t(c_{i+1}^t - c_i^t) \ . \tag{2.76}$$

with $A_{i-1/2}^t$ and $B_{i+1/2}^t$ are data dependent coefficients of neighbor cells. In (Harten, 1983) and (Sweby, 1984) it was proven that sufficient conditions for the scheme to be TVD are the inequalities:

$$A_{i+1/2}^t \geq 0, \quad B_{i+1/2}^t \geq 0, \quad \text{and} \quad A_{i+1/2}^t + B_{i+1/2}^t \leq 1 \ . \tag{2.77}$$

In our case :

$$c_i^{t+1} = c_i^t - \frac{\Delta t}{\Delta x}\left(u_{i+1/2}c_{i+1/2}^t - u_{i-1/2}c_{i-1/2}^t\right) . \tag{2.78}$$

2.3.3 Study of the numerical behaviour: effect of time step

The advection-diffusion problem, was solved treating advection with an Euler explicit scheme while diffusion was treated with an Euler implicit scheme. Implicit methods are unconditionally stables, however explicit methods are not. The time step on the solution of advection must respect the Courant–Friedrichs–Lewy (CFL) condition

$$\Delta t_{adv} \leq \frac{dx}{u_{max}} \ , \tag{2.79}$$

where dt_{adv} is the advective time step, dx is the voxel size (which in this case is the same in all directions), and u_{max} is the maximum value of velocity in

	Re=10		**Re=1**		**Re=0.1**		**Re=0.01**	
dx (μm)	$\mathbf{dt}_{CFL}$	$\mathbf{dt}_{TVD}$	$\mathbf{dt}_{CFL}$	$\mathbf{dt}_{TVD}$	$\mathbf{dt}_{CFL}$	$\mathbf{dt}_{TVD}$	$\mathbf{dt}_{CFL}$	$\mathbf{dt}_{TVD}$
4.5	0.00004	0.00001	0.00043	0.0001	0.00429	0.001	0.04286	0.01
6	0.00006	0.00001	0.00057	0.0001	0.00571	0.001	0.05714	0.01
9	0.00009	0.00001	0.00086	0.0001	0.00857	0.001	0.08571	0.01
18	0.00017	0.00001	0.00171	0.0001	0.01714	0.001	0.17143	0.01
36	0.00343	0.00001	0.03429	0.0001	0.34286	0.001	3.42857	0.01

Table 2.1: CFL condition on time step for each Re number and RF analyzed.

the velocity field. In this study the voxel size was fixed to six cases 4.5 μm, $6\mu m$, $9\mu m$, $18\mu m$ and 36 μm according to the respective RF. The maximum velocity is constrained to the velocity field of a creeping flow process $Re \leq 10$. Here four cases were chosen those corresponding to Re=10, 1, 0.1, and 0.01. Using Eq. (2.23) we observe that those Re number correspond to velocity fields with maximum velocity given by:

$$u_{max} = \frac{\nu Re}{d_{50}} = Re\, 1.05 \times 10^{-2} m/s \ , \tag{2.80}$$

with $\nu = 1.05 \times 10^{-6} m^2/s$, and d_{50} is the pore corresponding to the maximum velocity obtained from (Ramírez et al.) as $1 \times 10^{-4} m$. In this way we obtained a v_{max} as a function of the Re number chosen. According to the CFL condition we can obtain maximum time step dt_{CFL} that leads to a convergent solution if we substitute this velocity into Eq. (2.79) for each RF and each Re number. For simplicity and following the CFL condition for all the RF at a fixed Re number it was chosen as the TVD time step dt_{tdv} the immediately smaller round decimal of the best resolution case at the given Re number. These results are displayed in Table 2.3.3.

The chosen Re numbers of 10, 1, 0.1, and 0.01, following Eq. (2.35) with v the averaged velocity computed into the ADE code for each velocity field (obtained from the GeoDict software), $D_{50} = 5.4 \times 10^{-5} m$ ([4]) the average pore size lead us to the Peclet numbers 165, 16.5, 1.65, and 0.165.

$$Pe = \frac{uD_{50}}{D_0} \ . \tag{2.81}$$

[4]computed via the flux analysis proposed in (Ramírez et al.)

Number of dt_{tdv} iterations per dt_{diff} iterations	dt_{tdv} **(s)**	dt_{diff} **(s)**	t_{tot} **(s)**	**Error %**
1	0.0001	0.0001	100	0
10	0.0001	0.001	100	0.00044
100	0.0001	0.01	100	0.00431
1000	0.0001	0.1	100	0.02500
10000	0.0001	1	100	0.11502

Table 2.2: Study of the number of advection time step for one diffusion time step

Given that most of the Pe numbers chosen are bigger than one, the no conditioned time step of diffusion and the constant necessity to minimize the computing steps, we searched for the biggest possible diffusion time step, dt_{diff}.

We run the ADE code with different number (1,10,100,1000,10000) of dt_{TDV} per dt_{diff}. For all these cases we compared the Concentration fields at the same two times (when at 0.5 PV and 0.75 PV), and considering each field element the normalized root mean square deviation (NRMSD) was computed. The NRMSD presented an increasing linear behavior with the number of iterations of dt_{TDV} per dt_{diff}. The same behave was observed at all the Pe numbers (keeping also the same order of magnitude at the respective number of iteration).

$$NRMSD = \frac{1}{(c_{max} - c_{min})} \sqrt{\frac{\sum_N (c_{dt_{TDV_1}} - c_{dt_{TDV_2}})^2}{N}} \ . \tag{2.82}$$

It was observed that with 10000 iterations of dt_{TDV} per dt_{diff} leaded to big times considering one PV of the studied VOIs. Since even the case of 10000 iterations of dt_{TDV} per dt_{diff} presented a NRMSD smaller than 1% it was chosen for all the experiments developed a reason of

$$1000 \ dt_{TDV} \ per \ dt_{diff} \ .$$

An example of this analysis is shown in Table 2.3.3 for the case of Pe=16.5

2.3.4 General structure of the code

The solute transport is modelled at a microscale by the advection diffusion Eq. (2.33)

$$\frac{\partial c}{\partial t} - \nabla \cdot \nabla D_0 c + \nabla \cdot \mathbf{u} c = 0 \ ,$$

where c is the solute concentration, $\mathbf{x}$ is a coordinate vector, D_0 is the molecular diffusion coefficient, and $\mathbf{u}$ is the velocity field obtained from the Stocks Equation in (2.21). As a boundary condition we kept c at a constant value at the inflow boundary and allow it to undergo pure advection at the outflow boundary

$$\begin{aligned} c|_{in} &= c_0 && \text{inlet} \\ (c\mathbf{u} - D_0 \nabla c) \cdot \mathbf{n}|_{out} &= c\mathbf{u} \cdot \mathbf{n} && \text{outlet} \\ (c\mathbf{u} - D_0 \nabla c) \cdot \mathbf{n}|_{out} &= 0 && \text{walls .} \end{aligned} \tag{2.83}$$

Once the steps for the modelling of the solute transport were presented, we can synthesize the whole process in the flux diagram Fig. 2.2.

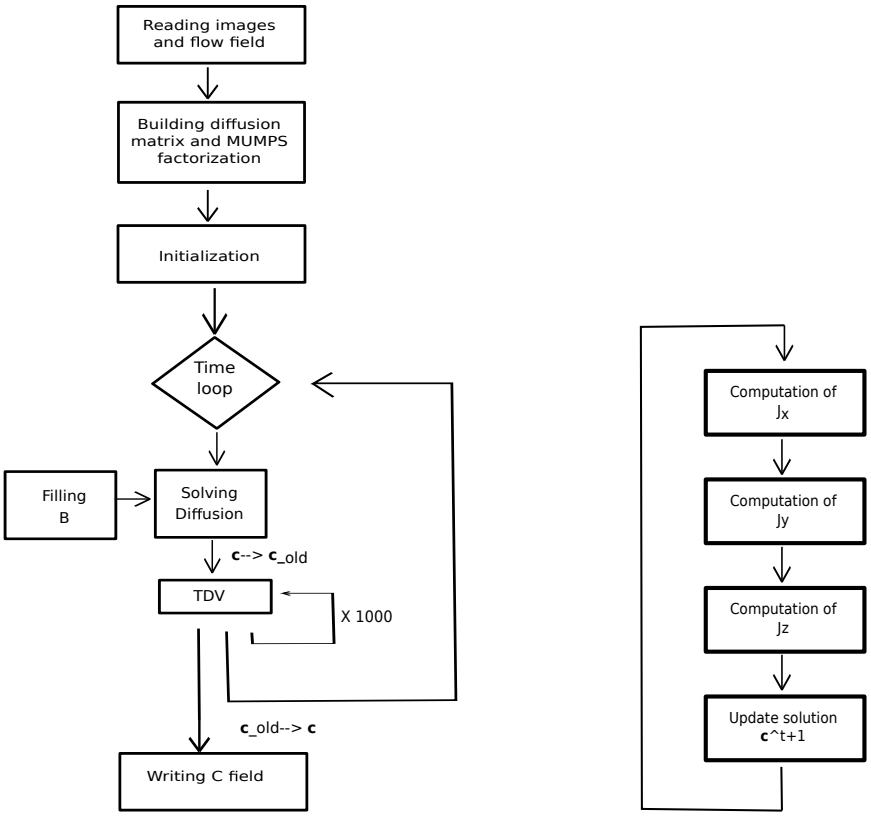

Figure 2.2: (a) Flow chart of the ADE code and (b) details of the TVD iterations of the ADE code.

Chapter 3

Modelling flow and solute transport at the macroscale

In the previous chapter the conservation equations were presented at microscale. However, we want to make the transition from the discrete pore space to the continuum and to macroscopic field variables which describe the observed phenomena. Here in this section it is presented the macroscopic scale ones.

3.1 Darcy's law and permeability

Darcy's law describes the flow of a fluid through a porous medium. It first was formulated on empirical results (Darcy, 1856). It suggests a linear relationship between flux and the gradient of hydraulic head height difference between the water levels at the inlet and outlet ends of a column of pore media.

$$\mathbf{U}_{Darcy} = \frac{\mathbf{Q}}{A} = -\frac{\mathbf{k}}{\mu}(\nabla P + \rho g \mathbf{e}_z) \ , \tag{3.1}$$

where P is the pressure $[Pa]$, μ is the fluid dynamic viscosity, $\mathbf{U}_{Darcy}$ the average velocity of the flow into the porous media known also as the Darcy velocity $[m/s]$, Q is the flow rate $[m^3/s]$, A is the cross-sectional area $[m^2]$ and $\mathbf{k}$ is the permeability tensor $[m^2]$, and $\mathbf{e}_z$ is a vertical unit vector (Bear, 2018).

The permeability tensor is a material property of the porous material. It characterizes the resistance of the material to let flow the fluid. Math-

ematically it is a second rank, symmetric tensor if the material is not homogeneous. For microscopically anisotropic media, $\mathbf{k}$ is also anisotropic and causes the flux direction to deviate from that of its driving force. For isotropic media $\mathbf{k}$ may be replaced by a scalar. Typical values of permeability range as high as $10^{-7}m^2$ for gravel, to values less than$10^{-20}m^2$ for granite. In our case the permeability of sand normally is around $10^{-12}m^2$.

It can be shown that Darcy's law could also be deduced from the Stokes equations (Whitaker, 1986).

Because flow only takes place within the pore spaces of the porous medium, for a given Darcy velocity $\mathbf{U}_{Darcy}$ the average pore velocity $\mathbf{U}_{pore}$ is increased compared to the Darcy velocity by the reciprocal of the porosity (Lichtner et al., 1996).

$$\mathbf{U_{pore}} = \frac{\mathbf{U}_{Darcy}}{\phi} \ . \tag{3.2}$$

It is important to clarify that the average pore velocity is quite different from the micro scale fluid velocity within individual pore spaces.

According to Darcy's law the fluid velocity depends only on macroscale properties of the porous medium. While the microscale complexity is conveniently described by the permeability.

3.1.1 Computation of permeability

To compute permeability it was used commercial software GeoDict. It uses the microscale velocity field to compute the mean flow velocity, $\mathbf{U}_{Darcy}$, for a given pressure drop, ΔP. In a post-processing step, Darcy's law, is used to compute the material permeability, k, using mean flow velocity, fluid viscosity, μ, pressure drop, and media thickness. For slow and faster flows, FlowDict assumes a steady flow regime, without time-dependent behavior. Thus, velocity and pressure drop cannot be arbitrarily high. It should guarantee that the Re number remains small (Re<10) in order to prevent the appearance of inertial effects.

3.2 Macroscale ADE and hydrodynamic dispersion

The study of solute transport through a porous media leads us to the study of the macroscopic phenomena called dispersion. It can be described as the spread out of the transported species under the combined action of molecular diffusion and the non uniform velocity field. It was originally studied in pipes by Taylor and Aris (Taylor, 1954) and (Aris, 1956). Finding that the dispersion along a tube is governed by a coefficient of diffusivity which can be calculated from observed distributions of concentration. However this task is more complex for a porous media, and is the subject of the following paragraphs. For the writing of this section the books of (Bear, 1979) and (Bear and Verruijt, 1987) were mainly used.

To understand this process we must observe what happens at the pore scale. The dispersion that occurs along the streamline of the fluid flow is called longitudinal dispersion and in porous media can be caused by

- Changes in the fluid velocity due to the radial position into the pore (the fluid moves faster through the center of the pore than along the solid surface).
- The pathway size variations of the fluid along the porous media.
- Differences in the fluid velocities due to the size of the pore (the fluid that travels through large pores will travel faster than fluid moving in smaller pores).

The dispersion that occurs perpendicular to the fluid flow is called lateral dispersion in the porous media can be caused due to

- The resulting gradient of concentration along the microscopic streamline due to the fluid velocity variations which induces lateral diffusion.
- Lateral spreading due to the shape of flow path.

To obtain the macroscopic equation of solute conservation in a porous media, following the conservation equation Eq. (2.8) we need to find an expression for the macroscopic flux of solute $\mathbf{J}_c$. This flux should describe the contribution of diffusion and advection at the microscale. For this

purpose it is chosen a REV in order to compute reliable averaged quantities. A quantity x is defined by its average as $x = \langle x \rangle + \tilde{x}$, where $\langle x \rangle$ is the average of the quantity x, and $\tilde{x}$ represent the deviation from the average of the quantity. Therefore $\langle \tilde{x} \rangle = 0$.

In the velocity case it is computed the average pore velocity as

$$\langle \mathbf{u} \rangle = \frac{1}{v_{pore}} \int \mathbf{u} dv = \mathbf{U}_{pore} \tag{3.3}$$

where v_{pore} is the pore volume and the average total velocity as

$$\langle \mathbf{u} \rangle_{Darcy} = \frac{1}{v_{total}} \int \mathbf{u} dv = \mathbf{U}_{Darcy} \tag{3.4}$$

where v_{tot} is the total volume.

Lets consider the average pore velocity and average concentration (the mass of the substance per unit volume of the liquid) and compute the average product

$$\langle \mathbf{u}c \rangle \quad = \quad \langle \mathbf{u} \rangle \langle c \rangle + \langle \tilde{c}\tilde{\mathbf{u}} \rangle \ . \tag{3.5}$$

Here $\langle \mathbf{u}c \rangle$ is the average of the microscale advective flux, $\langle \tilde{c}\tilde{\mathbf{u}} \rangle$ is the dispersive flux $\mathbf{J}_{disp}$, and $\langle \mathbf{u} \rangle \langle c \rangle$ is the macroscopic advective flux that taking into acount that $\langle c \rangle$ is the macroscopic concentration C and Eq. (3.3) it can be writen as

$$\mathbf{J}_{adv} = \langle \mathbf{u} \rangle \langle c \rangle = \mathbf{U}_{pore} C \tag{3.6}$$

The dispersive flux is a macroscopic flux that expresses the effect of the microscopic variations of the velocity in the vicinity of a considered point and therefore, it is responsible of the spreading. Being a result of the averaging it does not exist at a microscopic level. It is assumed that it obeys a Fickian type law with a coefficient of dispersion $\mathbf{D}$.

$$\mathbf{J}_{disp} = \langle \tilde{c}\tilde{\mathbf{u}} \rangle = -\mathbf{D} \cdot \nabla \langle c \rangle = -\mathbf{D} \cdot \nabla C \ , \tag{3.7}$$

where $\mathbf{D}$ is a second rank tensor $[m^2/s]$. Authors like (Scheidegger, 1961) developed an expression for the relationship between the dispersion coefficient

D, and the flow velocity.

$$D_{ik} = \frac{\alpha_{iklm} u_l u_m}{|\mathbf{U}_{pore}|} \ , \tag{3.8}$$

where α is called dispersivity, it is a fourth rank tensor with units [m] which expresses the microscopic configuration of the porous media. Thus, it is considered to be a characteristic property of the porous medium.

The dispersion tensor can be transformed so that the only elements of the major diagonal remains non zero if its principal axes are oriented to parallel and transverse to the mean direction of the flow. This simplification leads to the dispersion coefficient components:

$$D_{ik} = \alpha_T \mathbf{U}_{pore} \delta_{ij} + (\alpha_L - \alpha_T) u_i u_j |\mathbf{U}_{pore}| \ , \tag{3.9}$$

where parameters α_L and α_T are called longitudinal and transversal dispersivities of the isotropic porous medium respectively.

At this point we can observe that dispersion is a macroscopic process similar to the microscopic, however, unlike diffusion, it occurs only during water movement.

The second average flux to compute is the average flux due to diffusion. Based on the microscopic expression of diffusion Eq. (2.29) in (Bear and Bachmat, 1983) and (Bear and Bachmat, 1984) was derived an expression for the macroscopic flux in the form

$$\mathbf{J}_{diff} = \langle \mathbf{j} \rangle_{diff} = -\mathbf{D}_d^* \cdot \nabla \langle c \rangle \ , \tag{3.10}$$

where $\mathbf{D}_d^* = D_0 \mathbf{T}^*$ and $\mathbf{T}^*$ is known as tortuosity, a second order rank that expresses the effect of the configuration of the pore space in the REV.

Adding the dispersive flux and the diffusive flux, we obtain the flux known as the hydrodynamic flux ($\mathbf{J}_{disp} + \mathbf{J}_{diff}$)

$$\mathbf{J}_{hydrod} = -(\mathbf{D} + \mathbf{D}_d^*) \cdot \nabla \langle c \rangle = -\mathbf{D}_h \cdot \nabla \langle c \rangle \ , \tag{3.11}$$

where $\mathbf{D}_h$ is the coefficient of hydrodynamic dispersion.

$$\mathbf{D}_h = D_0 \mathbf{T}^* + \frac{\alpha_{iklm} u_l u_m}{|\mathbf{U}_{pore}|} \ . \tag{3.12}$$

Finally adding the advective flux and the hydrodynamic flux we obtain the desired total macroscopic solute flux $\mathbf{J}_c$

$$\mathbf{J}_c = \mathbf{U}_{pore} C - \mathbf{D}_h \cdot \nabla C \ . \tag{3.13}$$

Substituting this flux into the continuity Eq. (2.8) we obtain the macroscopic advection-dispersion equation

$$\frac{\partial C}{\partial t} = -\nabla \cdot (\mathbf{U}_{pore} C - \mathbf{D}_h \cdot \nabla C) \ . \tag{3.14}$$

In practice it easier to measure the Darcy velocity then substituting Eq. (3.2) into Eq. (3.14) leads to

$$\frac{\partial C}{\partial t} = -\nabla \cdot (\frac{\mathbf{U}_{Darcy}}{\phi} C - \mathbf{D}_h \cdot \nabla C) \ . \tag{3.15}$$

Which can be simplified to

$$\frac{\partial \phi C}{\partial t} = -\nabla \cdot (\mathbf{U}_{Darcy} C - \phi \mathbf{D}_h \cdot \nabla C) \ . \tag{3.16}$$

Eq. (3.14) in 1D reduces into an isotropic media to

$$\frac{\partial \phi C}{\partial t} = -\frac{\partial}{\partial x}(C U_{Darcy} - \phi D_h \frac{\partial C}{\partial x}) \ , \tag{3.17}$$

with

$$D_h = T^* D_0 + \alpha_L U_{Darcy_x} \ . \tag{3.18}$$

In the studies of solute transport, it is common use (3.17) with the dispersivity like a fitting parameter to match the behavior of curve of concentration function of the time through a porous media. However, even dispersivity is a characteristic of the porous material, studies have reported it is scale dependent. It increases with the travel distance of the solute. For example(Huang et al., 1995; Pickens and Grisak, 1981a) reported dispersivities of 0.1 to 5 cm for homogeneous sandy columns of 12.5 m long with cross section of $100 cm^2$. In (Kim et al., 2002) dispersivity was obtained at multiple positions in a aquifer revealing that dispersivity length is proportional to the travel distance by a factor of 0.3, which was moderately higher than the value of 0.1 given in (Lallemand-Barres and Peaudecerf, 1978).

3.3 BTC analysis

The soil column experiments provide a tool to quantify the mixing, spreading or attenuation of a solute. Therefore, they have been widely used to evaluate solute transport models, to understand the fate and migration of contaminants through soils, to evaluate the properties of the soil, or bacteria transport, among others. They consist in setting a column of porous media and injecting in one side a solute solution with concentration C_0 which gradually will displace the preexisting solution of concentration C_i. Analysis of the collected effluent from the pore media at a given depth shows a change in composition of effluent solution with respect to time. The graphical representation of the fraction of the incoming solute $(C - C_i)/(C_0 - C_i)$ (or C/C_0 in case of initial concentration equals zero) with respect to time is known as breakthrough curve (BTC) (Kutílek et al., 1994).

A frequent term here used is the pore volume (PV), which is the ratio at a given time between the cumulative effluent volume and the total pore volume of the material. This means that 1PV corresponds to the time needed to fill the pore volume space of the material with the injected solute. Another way to represent a BTC is the incoming solute fraction in function of the PV.

BTCs can have different shapes depending upon the solute application and the nature of the process in between the pore media. A solute introduced as a step input, will displace all the preexisting solution gradually (normally). Therefore, the concentration of applied solution increases whereas that of the preexisting solution decreases with time. If the application of displacing or applied solution continues, it attains the maximum concentration equal to C_0. The sharpest is the output curve the lower the effect of dispersion or interaction between the solute and the soil matrix.

3.3.1 CXT FIT

In order to obtain the dispersivity coefficient from a BTC the CXTFIT 2.0 software may be used in its inverse problem function. The CXTFIT 2.0 is a public domain software for estimating solute transport parameters using a nonlinear least-squares parameter optimization method. It can be used to solve the inverse problem by fitting a variety of analytical

solutions of theoretical transport models, based upon the one-dimensional advection-dispersion equation (ADE), to given concentration function of time data. Therefore given the concentration, time, pore average velocity at the outlet of out simulation we obtained the hydrodynamic coefficient for our sample. The program may also be used to solve the direct or forward problem to determine concentrations as a function of time and/or position. Here the necessary data are the hydrodynamic coefficient and pore velocity in order to obtain a BTC. We used this mode also to check the behaviour of our resulting BTCs (Toride et al., 1995).

3.3.2 Computation of the hydrodynamic coefficient and dispersivity

In this thesis we used the algorithm here developed to simulate column sand experiments. In our simulation we injected to a volume of interest (VOI) of Fontainebleau sand solute concentration during 1PV, 2PV and 3PV. We chose four positions where to study the solute mimicking four different sizes of the column sand and we saved the concentration field each 10 Δt_{diff}. Being L the size of the VOI we studied, the positions were at $L_1 = L/4$, $L_2 = L/2$, $L_3 = 3L/4$ and $L_4 = L$. At these positions we compute the solute flux average

$$C_{flux}(\lambda) = \frac{\sum_{j,k}^{N_y,N_z} u_x(\lambda,j,k)c(\lambda,j,k)}{\sum_{j,k}^{N_y,N_z} u_x(\lambda,j,k)}\ , \tag{3.19}$$

with the flux going in the x direction, λ the grid element corresponding to the chosen position for instance L_1. N_y, N_z are the maximum number of voxels in the y and z direction and j, k are indexes that run on the grid elements in the direction y and z respectively. We computed in this way the averaged concentration from time equals zero till three times the injection time. We obtained BTCs like are shown in Fig. 3.1 with this data and CXTFIT we computed the hydrodynamic coefficient for each case.

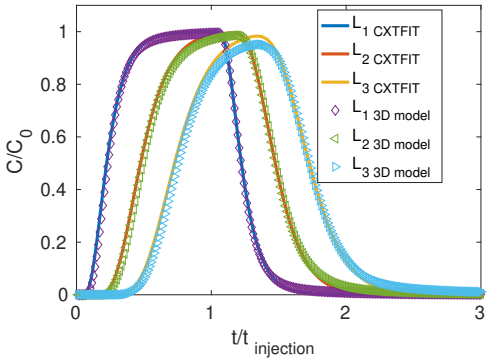

Figure 3.1: Example of a BTC for RF=0.75 and 1PV injection time

3.4 Analytical analysis

One of the main purposes of this thesis is to generate a 3D model which reads a segmented 3D image and taking it as the geometry, solves the advection diffusion Eq. (2.33). In order to validate this model we drew on analytic solutions of Advection, diffusion and dispersion on simple geometries and boundary conditions where the solution is known.

As it was presented in Section 2.3.1, in the presence of only diffusive flux, the transport equation Eq. (2.30) is a linear parabolic partial differential equation. In the following paragraphs three cases with known analytical solution will be presented. All of them occur in a 1D bar of size L, with constant diffusion coefficient D_0, but different boundary and initial conditions. In this case Eq. (2.30) can be simplified to

$$\frac{\partial c}{\partial t} - D_0 \frac{\partial^2 c}{\partial x^2} = 0 \ . \tag{3.20}$$

3.4.1 1D Diffusion at stationary case

$\frac{\partial^2 c}{\partial x^2} = 0$, with Dirichlet boundary conditions:

$$c(x = 0) = c_1 \quad c(x = L) = c_2 \ . \tag{3.21}$$

with $c_1 = 1$ and $c_2 = 0$ arbitrary constants. In the static case Eq. (3.20) simplifies to

$$\frac{\partial^2 c}{\partial x^2} = 0 \ , \tag{3.22}$$

integrating it two times in x leads to its general solution

$$c(x) + xc_1 + c_2 = 0 \ , \tag{3.23}$$

where c_1 and c_2 are integration constants, using the c_1 and c_2 we get the particular solution

$$c(x) = 1 - \frac{x}{L} \ . \tag{3.24}$$

Code application

To simulate this case (1D diffusion with Dirichlet BC c(0)=1 c(L)=0), the transport phenomena was simulated to pass through a bar of 301×3×3 with a given voxel size of 18 μm (however this computation must be independent of the voxel size) with water as the fluid which has diffusion coefficient $D_0 = 1 \times 10^{-9}$.

The diffusion computation is unconditional stable, therefore this test was used to verify the convergence of the code. If it is good our model should be fine with any diffusion time step, the time input used was: diffusion time step dt=1, total number of iterations Nt=30001 (however the convergence was reached since iteration 24000). A function called *M_layer* was used to compute the average concentration at a given layer i (perpendicular to the flux). In this case 16 positions were computed (i=18,36,54,72,...,288). The code results and the theoretical results can be seen in the Fig 3.2. Physically

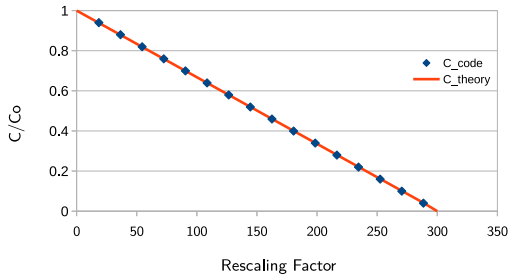

Figure 3.2: Case 1

this problem represents a source that is always present at x=0, and a well at x=L, being the stationary case, a linear behaviour is expected, It is observed a perfect agreement between the theoretical behavior and the computed results is observed.

3.4.2 1D Diffusion at non stationary case

Boundary and initial conditions:

$$c(0,t) = c_1, \quad c(L,t) = c_2 \quad \text{and} \quad c(x,0) = f(x)\ . \tag{3.25}$$

With $f(x) = 0$ for $x \neq 0$ and $f(x) = 1$ for $x = 0$.

If the conditions were homogeneous (not a function like here) the classical approach to solve the equation would be to use the method of variable separation. However, this is a partial equation with inhomogeneous conditions, one approach to solve it consists in solving the equilibrium case, and rewrite the problem in a more favorable way.

When $t \to \infty$ we can expect that the concentration is stationary then the problem becomes

$$\frac{\partial^2 c_{eq}}{\partial x^2} = 0, \qquad c_{eq}(0) = c_1, \qquad c_{eq}(L) = c_2 \ , \tag{3.26}$$

which is known from to the previous case, just using the appropriate BC ($c_1 = 1$, $c_2 = 0$)we get

$$c_{eq}(x) = c_1 - (c_2 - c_1)\frac{x}{L} \ . \tag{3.27}$$

We now define an auxiliary function $A(x,t) = c(x,t) - c_{eq}$, then we can write c and its derivatives in terms of A and c_{eq}

$$\begin{aligned} c(x,t) &= A(x,t) + c_{eq} \\ \frac{\partial c}{\partial t} &= \frac{\partial A}{\partial t} + \frac{\partial c_{eq}}{\partial t} \\ \frac{\partial^2 c}{\partial x^2} &= \frac{\partial^2 A}{\partial x^2} + \frac{\partial^2 c_{eq}}{\partial x^2} \ . \end{aligned} \tag{3.28}$$

On the one hand $\frac{\partial^2 c_{eq}}{\partial t} = 0$ because c_{eq} is the equilibrium concentration and it is independent of time. In the other, according to (3.26) $\frac{\partial^2 c_{eq}}{\partial x^2} = 0$ then

$$\frac{\partial c}{\partial t} = \frac{\partial A}{\partial t} \qquad \frac{\partial^2 c}{\partial x^2} = \frac{\partial^2 A}{\partial x^2} \ . \tag{3.29}$$

Which means that $A(x,t)$ should obey the diffusion Eq. (3.20). In order to be capable to solve A, we need to know its boundary and initial conditions.

$$\begin{aligned} A(x,0) &= c(x,0) - c_{eq}(x) = f(x) - c_{eq}(x) \\ A(0,t) &= c(0,t) - c_{eq}(0) = c_1 - c_1 = 0 \\ A(L,t) &= c(L,t) - c_{eq}(L) = c_2 - c_2 = 0 \ . \end{aligned} \tag{3.30}$$

The problem of A is given by

$$D_0 \frac{\partial^2 A}{\partial x^2} = \frac{\partial A}{\partial t} \ , \tag{3.31}$$

with boundary and initial conditions

$$A(x=0,t)=0, \qquad A(x=L,t)=0 \qquad A(x,0)=f(x)-c_{eq} \ . \tag{3.32}$$

It is the problem of a partial differential equation with homogeneous boundary conditions, where we can apply the method of separation of variables and get

$$A(x,t) = \sum_{n=1}^{\infty} B_n \sin\left(\frac{n\pi x}{L}\right) \exp^{-D_0\left(\frac{n\pi}{L}\right)^2 t} \ , \tag{3.33}$$

with

$$Bn = \frac{2}{L}\int_0^L (f(x)-c_{eq}(x)) \sin\left(\frac{n\pi x}{L}\right) dx \quad n=1,2,... \tag{3.34}$$

Due to the boundary conditions (3.25) and (3.27), B_n is simplified to $B_n = \frac{-2}{n\pi}$. Substituting the solution of A from Eq. (3.33) and c_{eq} from Eq. (3.27) into Eq. (3.28) we obtain the solution of the initial problem (3.31) (For more details in solving these kind of equations see (Dawkins, 2018))

$$c(x,t) = 1 - \frac{x}{L} + \sum_{n=1}^{\infty} \left(\frac{-2}{n\pi}\right) \sin\left(\frac{n\pi x}{L}\right) \exp^{-D_0\left(\frac{n\pi}{L}\right)^2 t} \ . \tag{3.35}$$

This solution as time grows tends to the linear solution of case 1. in Fig 3.3.

Code application

To simulate this case (1D diffusion with Dirichlet BC c(0,t)=1 c(L,t)=0), the transport phenomena was simulated through a bar of 301×3×3 with a given voxel size of 18 μm (however this computation must be independent of the voxel size), with water as the fluid which has a diffusion coefficient at $D_0 = 1 \times 10^{-9}$.

The diffusion computation is unconditionally stable, thus the code should be fine with any diffusion time step, the time input used were: diffusion time

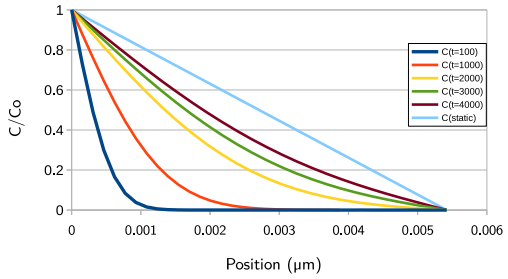

Figure 3.3: Evolution in time of concentration through the bar for the case 2 of diffusion.

step dt=1 second. Again the average concentration was computed via the function M_layer. In this case we are interested in the evolution on time of the concentration, thus it was computed at 5 layers i of the length L of the bar (i=L/6, L/3, L/2, 2L/3, 5L/6) at different times.

In Fig. 3.3 is plot the concentration distribution along the bar at different times, observing its behaviour at big times converges to the 1D diffusion static case solution. In Fig. 3.4 are compared the results from the code and the analytic solution. Again an excellent agreement is observed.

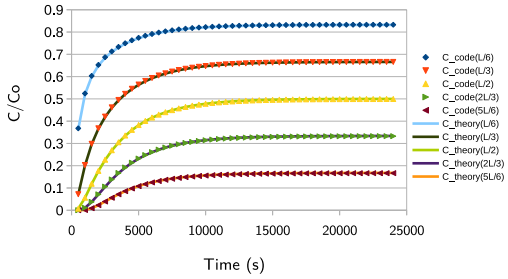

Figure 3.4: Case 2

Physically the boundary conditions can be represented as a source at x=0 that is always present injecting concentration to the bar and a well at x=L absorbing the concentration. At the beginning the bar is empty, and as time

passes it is filled till it reaches the equilibrium (see Fig 3.3) which should correspond to the linear case 1. In Fig. 3.4 we can see how the layers closer to the source converge to a value bigger than the ones further of the source. In all cases the agreement between the code and the theory is excellent.

3.4.3 1D ADE stationary case

Stationary advection-diffusion transport along a 1D bar of size L and concentration boundary conditions:

$$c(0) = c_1 = 0 \qquad c(L) = c_2 = 1 \ . \tag{3.36}$$

Rewriting (3.38) with the change of variable $\frac{\partial c}{\partial x} = f(x)$ we obtain an equation with a known solution given by

$$f(x) = c_1 \exp^{\mathbf{u}x/D_0} \tag{3.37}$$

This case simplifies Eq. (3.14) into

$$0 = \left(\frac{udc}{dx} + D_0 \frac{d^2c}{dx^2} \right) \ . \tag{3.38}$$

Inserting into Eq. (3.38)

$$c_1 \exp^{ux/D_0} = \frac{dc}{dx} \tag{3.39}$$

$$c_1 \int \exp^{ux/D_0} dx = \int dc \tag{3.40}$$

$$\frac{D_0}{u} c_1 \exp^{-ux/D_0} + c_2 = c \ . \tag{3.41}$$

Substituting the BC into the last expression we obtain

$$c(x) = \frac{\exp^{ux/D_0} - 1}{\exp^{uL/D_0} - 1} \ . \tag{3.42}$$

Code application

To compare the result of our 3D code with the analytical case of the 1D stationary ADE transport through a bar with BC c(0)=0 and c(L)=1 at $U > 0$ in a bar of $300 \times 3 \times 3$ voxels, with voxel size 1 μm with water as the fluid which has diffusion coefficient $D_0 = 1 \times 10^{-9} m^2/s$ was implemented to simulate the transport phenomena at four different velocities corresponding to the Pe=100,10,1,0.01. In Fig 3.5 we observe an excellent agreement between our numerical 3D computation and the analytical solution (3.42).

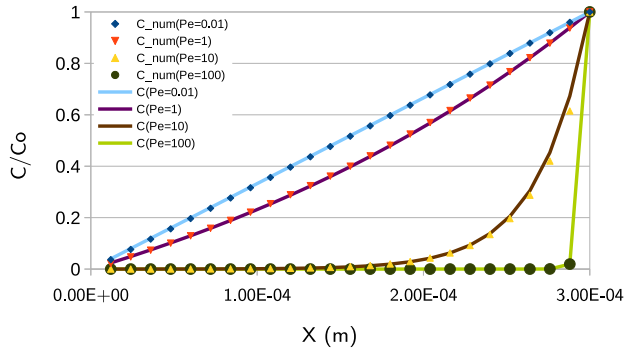

Figure 3.5: Case 1D ADE for different Pe numbers

3.4.4 3D ADE case along a pipe

Non stationary case of ADE along a pipe with boundary and initial conditions:

- Imposed concentration on the inlet

$$c|_{in} = c_0 = 1 \ . \tag{3.43}$$

- Free flow at the outlet which remains the more natural way to impose the tricky outlet boundary condition

$$D_0 \nabla c \cdot \mathbf{n}|_{out} = 0 \ , \tag{3.44}$$

with $\mathbf{n}|_{out}$ a unit vector normal to the outlet face.

- No flux at the wall interface taking advantage of the null velocity imposed in Stokes equation

$$D_0 \nabla c \cdot \mathbf{n} = 0 \ , \tag{3.45}$$

  with $\mathbf{n}$ the unit vector normal to the interface.

To compare the solution to this problem given by our 3D model we used the multiphysics simulation software called Comsol.

Code application

To compare the code and analytical results, we simulate the solute transport in a pipe of length $300\mu m$ and radius $20\mu m$ at three different average velocities[1], integrating this expression over the axial angle and the radius we obtain the average velocity in the pipe given by $u(r) = \frac{\Delta P}{L}\frac{R^2}{8\mu}$ ($u = 3.18 \times 10^{-6}, 3.18 \times 10^{-5}, 3.18 \times 10^{-4}$). Using the radius as the length scale of the problem in (2.34), the corresponding Pe numbers for those velocities are: Pe=0.06,0.6,6. The evolution of concentration in time at 3 different positions in the pipe are plotted in Fig 5.5.

[1] In a pipe the velocity field is given by $u(r) = \frac{\Delta P}{L}\frac{1}{4\mu}(R^2 - r^2)$ where P is the pressure, R is the pipe radius, L is the length of the pipe and μ is the Dynamic viscosity

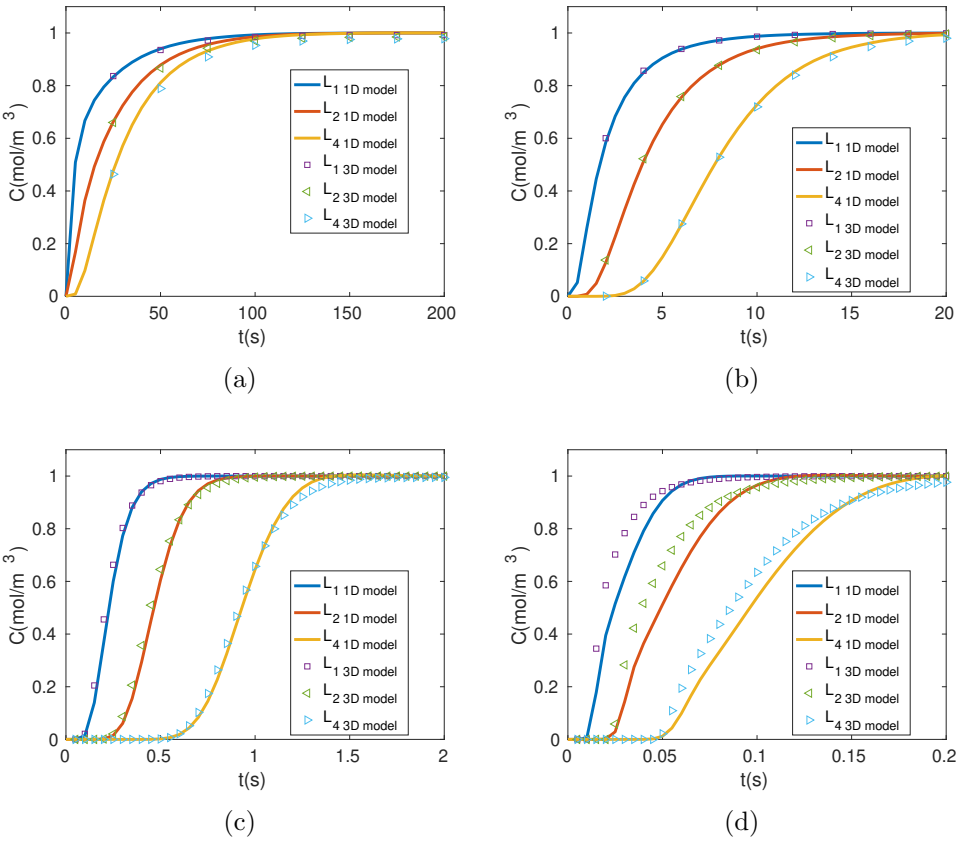
C(mol/m 3)
t(s)
L1 1D model
L2 1D model
L4 1D model
L1 3D model
L2 3D model
L4 3D model
(a)
(b)
(c)
(d)

Figure 3.6:

Chapter 4

Effect of X-ray CT resolution on the quality of permeability computation for granular soils: Definition of a criterion based on morphological properties

Miriam Patricia Ortega Ramírez[1], Laurent Oxarango[1] and Alfonso Gastelum-Strozzi[2]
1. Université Grenoble Alpes, CNRS, IRD, Grenoble-INP, IGE, F-38000 Grenoble, France
2. Instituto de Ciencias Aplicadas y Tecnologia, Universidad Nacional Autónoma de Mexico, Mexico, D.F., Mexico

Abstract

In this study, the quality of soil permeability estimation based on Computational Fluid Dynamics is discussed. Two types of 3D geometries were considered: an image of Fontainebleau sand obtained from X-ray Computed micro-Tomography and a virtual pack of spheres. Numerical methods such as Finite Difference or Lattice Boltzmann can conveniently use the image voxels as computational mesh elements. In this framework, the image resolution is directly associated with the quality of the numerical computation. A higher resolution should promote both a better

Abbreviation	Meaning
BRZ	Bad Resolution Zone
DNS	Direct Numerical Simulation
FDM	Finite Difference Method
LBM	Lattice Boltzmann Method
μCT	Micro Computed Tomography
PEEK	PolyEtherEtherKetone
PSD	Pore Size Distribution
RF	Rescaling Factor
REV	Representative Elementary Volume
SE	Structural Element
SREV	Statistical Representative Elementary Volume
SVOI	Statistical Volume of Interest
VPS	Virtual Pack Of Spheres
VOI	Volume Of Interest

Table 4.1: Table of abbreviations

morphological description and discretization. However, increasing the resolution may prevent the studied volume to be representative. Here, each sample is scaled and analyzed at five resolutions. The dependence of soil properties with respect to the image resolution is discussed. As resolution decreases, the permeability and specific surface values tend to diverge from the reference value. This deterioration could be attributed to the shift of the pore size distribution toward badly resolved pores in the voxelized geometry. As long as granular soils are investigated, the volume fraction of pores smaller than six voxels in diameter should not exceed 50% to ensure the validity of permeability computation. In addition, based on an analysis of flow distribution, the volume fraction of pores smaller than four voxels should not exceed 25% in order to limit the flow rate occurring in badly discretized pores under 10%. For the Fontainebleau sand and virtual pack of spheres, the maximum voxel size meeting this criterion corresponds to $1/14^{th}$ and $1/20^{th}$ of the mean grain size D_{50} respectively.

Keywords: Digital Rock Physics, soil permeability, soil morphology, image resolution

4.1 Introduction

Understanding fluid flow but also mass and energy transport in soils remains a challenging problem. The difficulty lies in the complexity of the material porous micro-structure. One of the key parameters required to understand these processes is the soil permeability. This macroscopic property describing saturated flow using the Darcy law is studied in many research fields involving flow in porous media such as: soil science studying tillage compaction effects on transport properties of water and gas (Chen et al., 2014) or the contribution of soil aggregates to water flow (Khan et al., 2012); civil engineering in dams construction (Nakaya et al., 2002) or aging of concrete material (Chatzigeorgiou et al., 2005); petroleum engineering in the estimation of efficiency in methane gas production (Liang et al., 2010), petroleum reservoirs (Ahmadi, 2015); or environmental science, in CO_2 geological storage (Juanes et al., 2006b). There have been numerous attempts to establish a relationship between some microstructural properties of the porous media, and permeability (Bear, 2013). However, no explicit function appears totally satisfying to correlate permeability accurately. Thus, to estimate permeability, a currently popular approach consists in solving flow equations within the pore space by Direct Numerical Simulation (DNS) (Mostaghimi et al., 2013). This strategy has been significantly improved by the generalization of detailed characterization of the pore space based on X-ray Micro Computed Tomography (μCT).

The μCT is a non destructive and three dimensional (3D) technique to visualize and quantify the internal structures of materials. It provides a 3D image stack which is a discrete representation in gray scale of volume data linked with the material local density. After a numerical treatment, called segmentation, each discrete 3D element (or voxel) can be assigned to a material phase. An image of dry soil is then composed of solid and void (or pore) voxels. The voxel size defines the spatial resolution of the 3D image (i.e. the smaller the voxel size, the higher the resolution). The total number of voxels mainly depends on the μCT apparatus sensor and the type of X-rays source. In every case, the better is the resolution the smaller has to be the sample.

When studying soils, the μCT technique is able to provide a totally resolved image of the pore and grain system for granular sandy soils (Fonseca et al.,

2012). When clayey soils are studied, it generally allows an analysis of the macro-porosity only with the micro-porosity consisting of pores smaller than the scan resolution (Peng et al., 2014). In both cases, the estimation of morphological properties (such as porosity, specific surface, pore size distribution, tortuosity or connectivity) should benefit from higher resolution to obtain a very detailed description of surfaces and volumes (Vogel et al., 2010; Kumar et al., 2010a). However, reaching the best possible resolution may not be the best solution to characterize soil due to theoretical principles of scale change in porous media. In order to estimate relevant macroscopic properties of a porous medium, the studied volume should remain larger than the representative elementary volume (REV) (Cnudde and Boone, 2013). For a given image size, it is thus convenient to select the worst resolution ensuring a relevant estimation of the studied properties in order to obtain the largest possible physical domain size. (Lehmann et al., 2006) computed various morphological properties (Pores Size Distribution and Minkowski functionals) of glass beads as a function of the resolution. This study concluded that the computation of these properties is converging provided that the ratio between the mean particle radius (d_{50}) and the voxel size is in the range of 5 to 10, 10 being a reasonable quality criterion. (Al-Raoush et al., 2003) proposed that this ratio should be at least of 25 to capture accurately the pore network structure (pore and throat size distributions and pore connectivity) of both ordered and disordered Virtual Pack of Spheres (VPS). (Al-Raoush and Willson, 2005) applied the same pore network analysis to μCT images of glass beads and Ooid marine sand at two resolutions. They concluded that some properties (pore throat number and sizes) drastically deteriorated for a ratio close to 10. This effect was more sensitive for glass beads since it presented a narrow distribution of grain sizes. These studies put forward that such a quality criterion should be chosen for each property of interest.

The question of selecting an appropriate μCT resolution is an even more sensitive issue if the computation of flux properties is considered since it implies a very high computational cost. Moreover, while applying DNS methods, the voxel space is generally used as a computational mesh (Finite Difference Method (FDM); (Wiegmann, 2007) or Lattice Boltzmann Method (LBM); (Khan et al., 2012)). In this case, the image resolution has both an effect on the morphology of the computational domain and on the quality of the numerical solution since it affects the size of mesh elements. Studying

this last effect independently, (Guibert et al., 2015a) suggested that a finer mesh improves the quality of the permeability computation for a given μCT image of Dausse sandstone. The coupled effect of resolution on both the geometry and the mesh size has been addressed in several studies. (Fredrich et al., 2006) showed a good agreement concerning the permeability value of sandstones computed with LBM on synchrotron tomography images at two resolutions (1.67 μm and 3.34 μm). (Borujeni et al., 2013) showed that the lower-quality image had a lower permeability computed with both LBM and Finite Element methods on a computer-generated consolidated porous medium at two resolutions. These studies did not address the question of the minimum acceptable resolution. (Yoon and Dewers, 2013) proposed an interesting approach to study the effect of resolution on permeability while studying Cretaceous Selma Chalk samples. They numerically reduced the resolution of 3D segmented images obtained by the Focus Ion Beam-Scanning Electron Microscopy (FIB-SEM) technique. They concluded that a resolution of 80 nm was enough to compute accurately morphological properties and permeability from LBM with an error lower than 10% compared to the original image which has a resolution of 15.6 nm. In a very detailed study, (Shah et al., 2016) analyzed the morphology and permeability of five sandstones and five carbonates samples scanned with μCT at $four$ resolutions ranging from 4.4 μm to 10.2 μm. They reported drastic changes in these properties in the relatively narrow range of studied resolution. In this study, a numerical deterioration (or coarsening) of the image was also applied to the segmented image obtained at the best resolution. The resulting computed properties were in much better agreement with the best resolution results than the ones obtained from the corresponding μCT images. This difference was attributed to the discrete coarsening method which limited the partial volume effect observed on real scans since it was based on a segmentation including the information at the finer resolution. Based on these results, the discrete numerical coarsening was proposed as a suitable method to decrease the computational time for permeability computation based on μCT images. However, this study did not define a maximum coarsening level.

The present paper proposes a method to determine the minimum image scan resolution required to obtain an adequate estimate of the permeability. It applies to granular material with fully imaged porosity (i.e. with no inner micro-porosity). Two materials are studied within a large range of numeri-

cally scaled resolutions: a sample of Fontainebleau sand scanned with a μCT and a stochastically generated VPS.

4.2 Material and methods

In this section, the image acquisition and processing are presented. The computation of material properties (porosity, specific surface, PSD and permeability) is described. Finally, a new combination of PSD and local flow field is introduced in order to derive the distribution of flow rate with respect to the pore size.

4.2.1 Sand sample preparation and image analysis

Sample

A cylindrical PEEK cell with size specifications of inner radius $\approx$ 7 mm, wall thickness $\approx$ 0.65 mm and height $\approx$ 7.5 mm, was used to store the sand during the tomography. The experimental volume, measured by filling the cell with water, was 356 $\pm$ 6 mm^3, 23.34% bigger than the theoretical volume which is 288.63 mm^3. The cell was filled with 555 $\pm$ 6 mg of Fontainebleau NE34 sand, which is a fine well graded sand of uniformity coefficient 1.6 with d_{50} = 210 μm, $d_0 \approx 100$ μm and $d_{100} < 450$ μm. The porosity is estimated by

$$\phi = \frac{V_{void}}{V_{Total}} = \frac{V_{Total} - V_{solid}}{V_{Total}}\,. \tag{4.1}$$

Knowing the mass of the empty cell, the mass of the cell filled with sand, the volume of the cell and the sand grain density, 2650 kg/m^3, the porosity was computed as 0.41$\pm$0.03 (using the experimental volume value).

X-ray CT

The sample was scanned with a laboratory tomograph EasyTom XL from RXSolutions. The LaB6 X-ray source was set to 70 kV and 67 μA with an exposure time of two seconds and four-frame averaging. A 1 mm aluminum foil was set on the X-ray source in order to filter inappropriate wavelength. The acquisition sequence consisted of 1600 projections of 2058 $\times$ 2058 pixels resulting in a scan time of approximately two hours. The 3D reconstruction stage was based on a cone-beam algorithm. It produced a serial of 1700 slides of 1850 $\times$ 1850 pixels cross-section. The corresponding voxel size was

4.5 μm. A cubic volume of interest (VOI) of 1200 voxels (or 5.4 mm) was extracted from the center of the initially cylindrical sample. A process of enhance contrast and a median filter (radius two voxels) were applied to clean the image. This VOI constitutes the reference material used for the analysis.

Image rescaling

In order to define a criterion able to determine if an image resolution is good enough to realize a dynamical computation, the same image was studied at different resolutions following a methodology inspired from (Shah et al., 2016). Rescaling or resizing is the process of increasing or decreasing the number of pixels in an image or voxels in a volume. It is rigorously defined by the image processing community if applied to a gray scale image before segmentation. This process is not lossless. Rescaling a volume to a smaller number of voxels, and then rescaling it back to the original resolution, results in an image sightly different from the original (Danahy et al., 2007). The rescaling process can be divided conceptually into two processes: 3D interpolation of the discrete volume to a continuous volume and then sampling the interpolated volume to the desired resolution (Parker et al., 1983). Various forms of interpolating functions have been developed. Reviews, and catalogs of methods can be found in (Lehmann et al., 1999) and (Grevera and Udupa, 1996). A comprehensive application of the rescaling method on μCT images of bones can be found in (Cooper et al., 2007). This study put forward a certain level of divergence between the morphological properties computed from rescaled images compared and μCT scans at the corresponding resolution. However, it should mimic partial volume effects in a more realistic way than the discrete rescaling presented by (Shah et al., 2016).

In the present study, the VOI was rescaled with four rescaling factors[1](RF) using the 3D bicubic interpolation algorithm (Imagej 2.34 software) with RF of 0.75, 0.50, 0.25, and 0.125 (The original image is considered to be scaled with RF = 1). The number of voxels per side of the obtained rescaled VOIs were: 900, 600, 300, and 150 voxels respectively, corresponding to voxel sizes of 6, 9, 18, and 36 μm. In Fig. 4.1 a square section of the VOIs is shown at the different RFs. As can be seen, a small RF significantly alters the image.

[1]Here the RF will be the same in the three directions. An image with RF = 0.5 has a number of voxels in each direction decreased to the half of the original image.

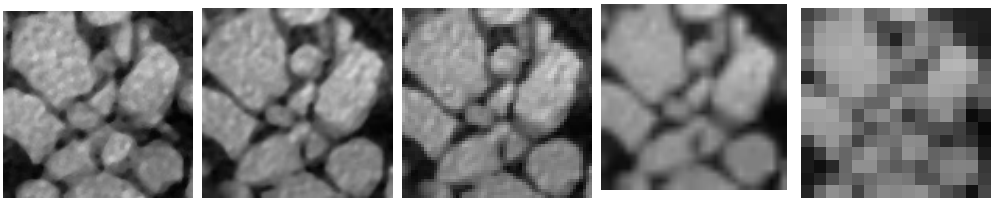

(a) Voxel size 4.5 μm, RF 1 (b) Voxel size 6 μm, RF 0.75 (c) Voxel size 9 μm, RF 0.50 (d) Voxel size 18 μm, RF 0.25 (e) Voxel size 36 μm, RF 0.125

Figure 4.1: Zoom on a square section of an arbitrary slide of the gray scale VOI at different rescaling factors for the Fontainebleau sand (side size 540 μm).

Segmentation

In order to compute morphological and transport properties of the sample, a segmentation between solid and void volumes has to be performed. This process aims at converting the gray scale into distinct phases, by identifying different populations in the image based on their intensity values. In this paper, the segmentation was done to distinguish between the solid and the void phases. The default Isodata algorithm of the software Imagej 2.34 was used (Ridler et al., 1978). It performs a simple thresholding based on the histogram of the full 3D image. In Fig. 4.2, the same section shown in Fig. 4.1 is presented after segmentation. Again the given shape is significantly altered for small rescaling factors. Even if the shape is visually preserved until a RF of 0.5, it can be seen that small spaces between grains are lost even for the RF of 0.75 which may limit a part of the flux in the permeability computation.

4.2.2 Virtual pack of spheres

The second material under consideration is a virtual pack of spheres (VPS) proposed by (Reboul et al., 2008). It is a numerical assembly of spheres in loose state designed originally to study filtration and internal erosion of soils. The VPS was obtained by depositing 10,000 spheres under gravity in a parallelepiped generating box. In order to match approximately the characteristic sizes of the Fontainebleau sand, the original dimensions were divided by a

(a) Voxel size 4.5 μm, RF 1 (b) Voxel size 6 μm, RF 0.75 (c) Voxel size 9 μm, RF 0.50 (d) Voxel size 18 μm, RF 0.25 (e) Voxel size 36 μm, RF 0.125

Figure 4.2: Zoom on a square section of an arbitrary slide of the segmented VOI at different rescaling factors for the Fontainebleau sand (side size 540 μm).

factor 10. The VPS presents a narrow grain size distribution (uniformity coefficient is equal to 1.5) with d_{50} being 440 μm (d_0 = 300 μm, d_{100} = 1.2 mm). The number of spheres was calibrated to ensure that the sample is a REV: each size of the box must consist of 10 to 100 mean particle diameters. The rationale behind using this virtual material is that its geometry is perfectly described by the 3D location of each individual sphere of known radius. Thus a binary image could be reconstructed at any chosen resolution by a simple Eulerian distance computation. Any voxel which center is contained in a sphere is attributed to the solid phase. In order to compare the VPS with the Fontainebleau sand sample, the reference image voxel size (RF = 1) was chosen arbitrarily as 7.5 μm for a cubic VOI with 3.6 mm length. Scaled images with RF = 0.5, 0.25, 0.125 and 0.0625 were considered (See an exemplary 2D slide in Fig. 4.3). The VPS geometry visually starts deteriorating for RF = 0.125. Shape and connectivity are apparently lost for RF = 0.125 and 0.0625. Some of the smaller spheres also disappear in these low resolution images (their diameter is smaller than the resolution).

4.2.3 Computation of morphological and dynamical properties

The computation of geometrical and dynamical properties is performed on the segmented images. Based on the analysis described in Appendix A, a cubic subsample (2.7x2.7x2.7 mm) was chosen as statistical representative elementary volume (SREV) for porosity, specific surface, and permeability.

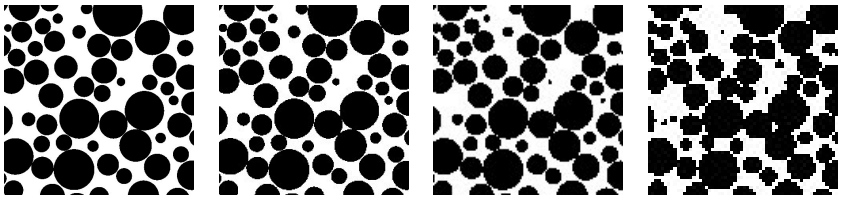

(a) Voxel size $7.5\mu m$, RF 1

(b) Voxel size $15\mu m$, RF 0.50

(c) Voxel size $30\mu m$, RF 0.25

(d) Voxel size $60\mu m$, RF 0.125

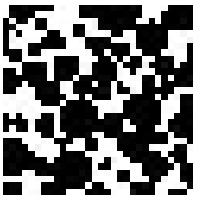

(e) Voxel size $120\mu m$, RF 0.0625

Figure 4.3: Square section of an arbitrary slide of the VPS at different rescaling factors (side size 3.6mm).

The computation of those quantities was performed on eight sub volumes of interest (SVOI) (see Fig. 4.4) for each rescaling factors. This approach provides a straightforward estimate of the discrepancy of the computed properties. In order to simplify the readability, the analysis of pore size distributions and the corresponding flow rate distribution are presented in a single SVOI of the same dimension located in the center of the VOI.

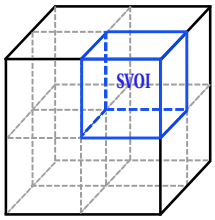

Figure 4.4: Scheme of the cubic VOI of 5.4 mm of side size, divided on 8 independent SVOIs of 2.7mm of side size.

Considering that the VPS sample's geometry is perfectly defined and designed to be representative, all analyses of this material were performed on the full sample.

Porosity, specific surface and Pore size distribution
The porosity, Eq. 4.1, was computed as the number of void voxels divided by the total number of voxels in the image.

The specific surface S_s is the ratio between the surface between solid and void phases and the total volume. It is defined as:

$$S_s = \frac{S}{V_{Total}} \tag{4.2}$$

where the surface S $[m^2]$ is the boundary between the solid and the void phases. It was computed using the discrete extension in 3D of the integral geometry theorem of Cauchy Crofton. This method is based on counting the intersections of a surface, with lines spread parallel to 13 directions in the entire 3D volume (Legland et al., 2011; Lehmann and Legland, 2012).

Pore size distribution is a common porous media property that classifies the porous phase into a set of discrete classes of pore size. Several methods have been proposed to compute the PSD of soils. Recently, (Houston et al., 2017) presented a detailed comparison of existing methods implemented in commercial or free software (Maximum Inscribed Balls, morphological closing, object separation or skeleton computation). Based on its good performance for granular soils, the method of morphological closing was used in the current study following the pioneer work of (Doughty and Tomutsa, 1996), who analyzed the pore size and connectivity of Fontainebleau and Bentheim sandstones. The method was applied on soils by (Vogel and Roth, 2001) to study a German Orthic Luvisol and more recently by (Muñoz-Ortega et al., 2015) to estimate the effect of tillage on soil structure.

The method requires a segmented image, where one phase is defined as the background (normally the void space), the other as the foreground (normally the solid space), and a structural element (SE). In the case of PSD in a 3D image, a natural SE choice is a sphere of diameter D_i. The morphological operation to be applied is the closing over the solid phase with the chosen SE. This operation consists of a dilatation step followed by an erosion step

using the same SE. The resulting image has a background where regions smaller than the SE have been removed, and consequently the foreground is increased.

In order to compute the PSD the closing operation is applied successively while increasing SE diameters D_i, which results in a progressive reduction of the pore phase or pore volume (Fig. 4.5). At each closing step, the remaining pore volume is computed which corresponds to pores with diameter bigger or equal to D_i. The difference between the pore volume in the original image and the pore volume after the closing operation gives the volume associated to pores with diameter between 0 and D_i. This technique provides the cumulative pore volume as a function of the pore size diameter. It is presented as percentage of the total pore volume.

(a) Original image before closing

(b) SE diameter of 10 μm

(c) SE diameter of 20 μm

(d) SE diameter of 30 μm

(e) SE diameter of 40 μm

(f) SE diameter of 50 μm

Figure 4.5: Zoom on a square section of the Fontainebleau sand of an arbitrary slide for RF 1 (size: 540 μm): Progressive closing operation.

Permeability computation

The partial differential equations that describe the mass and momentum balance of the fluid flow within an arbitrary domain are the classical

Navier-Stokes equations. While considering the small characteristic length of sandy soils (i.e. Reynolds number typically lower than 10^{-1}); (Happel and Brenner, 2012), the creeping flow assumption is generally used to simplify the set of PDE by neglecting inertial effects. The Stokes equations are then expressing the mass and momentum balances for an isothermal incompressible Newtonian fluid flow in steady state condition and neglecting gravity forces as:

$$\nabla \cdot \vec{u} = 0, \tag{4.3}$$

$$\mu \nabla^2 \vec{u} = \nabla P, \tag{4.4}$$

where $\vec{u}$ [m/s] is the pore scale velocity field, P [Pa] is the pressure and μ [Pa/s] is the dynamic viscosity of the fluid.

Solving equations 4.3 and 4.4 requires the introduction of appropriate boundary conditions which we set as:

- Uniform pressures applied on two opposite faces of the SVOI in order to impose a pressure drop ΔP of 0.02 Pa.
- Periodic boundary conditions on the lateral faces.
- No slip boundary conditions on the solid/void interfaces inside the domain.

Numerical computations were performed using the FDM, called Explicit Jump-Stokes solver (Wiegmann and Bube, 2000b), implemented in the GeoDict software package. The module "*FlowDict*" uses a cubic mesh conformed to the image voxels. It computes the three components of the velocity vector $\vec{u}$ and the pressure P in each voxel on a staggered grid. The Stokes problem (Eqs. 4.3 and 4.4 is decomposed into four Poisson problems solved iteratively using a Fast Fourier Transform-based algorithm (Wiegmann, 2007) An explicit jump approach of the immersed boundary concept is used to force the no-slip boundary condition as suggested by (Rutka, 2008). A relative error of 10^{-3} on the computed permeability was set as convergence criterion.

At the macroscale the governing equation of flow is the Darcy's law (Eq.4.5). Applied to the studied SVOI, it can be written as:

$$\frac{Q}{S} = -\frac{k}{\mu}\frac{\Delta P}{L}, \tag{4.5}$$

where Q is the volumetric flow rate $[m^3/s]$, S is the cross-section area orthogonal to the average pressure gradient $[m^2]$, k is the permeability $[m^2]$ (sometimes referred to as intrinsic or geometric permeability) and L [m] is the distance between the inlet and outlet faces of the SVOI.

In order to compute the permeability k in Eq.4.5, the flow rate Q is integrated numerically from the local flow field as:

$$Q = \int_S \vec{u} \cdot (\psi d\vec{A}), \tag{4.6}$$

where S $[m^2]$ is an arbitrary cross section of the SVOI, $d\vec{A}$ is the differential area vector, orthogonal to the average pressure gradient and ψ is a pore phase indicator (where 1 is the pore phase and 0 is the solid phase).

Distribution of flow rates in the pore classes

The local velocity field and the PSD allow to compute the contribution of each size of pore to the total flow rate Q (Eq. 4.6). The flow rate Q_i occurs in pores of diameters between D_{i-1} and D_i. In order to capture the contribution of each pore class, fluxes Q_i are computed as an average in the direction of the pressure gradient as:

$$Q_i = \frac{1}{Z}\int_z \int_S \vec{u} \cdot (\psi_i d\vec{A}) dz, \tag{4.7}$$

Where Z [m] is the length of the SVOI in the pressure gradient direction and ψ_i is the phase indicator associated with the pore class i. ψ_i is assigned to each voxel during the PSD computation process.

4.3 Results and discussion

In this section, the influence of resolution on porosity, specific surface and permeability are discussed. A detailed analysis based on the evolution of cumulative pore size distribution and the related distribution of flow rate in the sample is performed in order to relate the evolution of the permeability with the pore morphology. A criterion was then defined to estimate the quality of the permeability computation based only on morphological properties.

4.3.1 Effects of resolution on morphological and dynamical properties

The results are presented in Fig. 4.6 and detailed in Table 4.2. The computation of eight SVOI for Fontainebleau sand provided a measurement of the discrepancy of the data based on the standard deviation. It should be noticed that the standard deviation never exceeded 6% of the average value for the permeability, 1.5% for the porosity and 1% for the specific surface. These results support our assumption that the size of SVOI is large enough to be considered representative of the full VOI.

The property least affected by resolution was porosity for both materials (Fig. 4.3.a and b). The difference to the value of the best resolution was less than 7.7% even at a RF of 0.125 for Fontainebleau sand. In the case of VPS, the influence of resolution was even less sensitive with a maximum difference of about 0.2% for a RF of 0.0625. The artificial building of the VPS geometry partly explains this result but the disappearing of some grains observed on Fig. 4.3 was also compensated by the voxelization promoting some grain enlargement.

The specific surface exhibited a decreasing trend with decreasing RF for both materials (Fig. 4.3.c and 4.3.d). This behavior was attributed to a progressive smoothing of the solid phase roughness (i.e. a loss of the surface details) as the resolution decreased. Small solids disappearing and the merging of some solid surfaces at the lower RF probably contributed to the stronger decrease observed for RF lower than 0.5. At the worst resolution, the specific surface was underestimated by 38% for the Fontainbleau sand (RF = 0.125) and 42% for the VPS (RF = 0.0625). In the VPS, an exact value of S_s was computed explicitly from the known sphere radii. At the

Fontainebleau sand							
RF	voxel size μm	ϕ $\times 10^{-1}$	Relative error %	S_s $\times 10^{2} m^{-1}$	Relative error %	k $\times 10^{-11} m^{2}$	Relative error %
1	4.5	3.90 ± 0.01	-	2.16 ± 0.02	-	2.02 ± 0.10	-
0.75	6	3.86 ± 0.05	0.9	2.09 ± 0.02	3	2.01 ± 0.11	0.4
0.50	9	3.86 ± 0.05	0.9	2.00 ± 0.02	7	2.17 ± 0.12	7.7
0.25	18	3.90 ± 0.04	0.3	1.75 ± 0.01	19	2.77 ± 0.12	38
0.125	36	4.19 ± 0.04	7.7	1.34 ± 0.01	38	5.36 ± 0.16	166
Virtual pack of spheres							
RF	voxel size μm	ϕ $\times 10^{-1}$	Relative error %	S_s $\times 10^{2} m^{-1}$	Relative error %	k $\times 10^{-10} m^{2}$	Relative error %
1	7.5	3.798	-	6.63	-	2.15	-
0.50	15	3.799	0.01	6.32	4	2.19	0.4
0.25	30	3.797	0.04	5.93	10	2.25	5
0.125	60	3.802	0.09	5.17	22	2.62	22
0.0625	120	3.805	0.18	3.87	42	3.1	44

Table 4.2: Average properties computed in the rescaled SVOIs for Fontainebleau sand and the VPS.

best resolution (RF = 1), the numerical value was in good agreement with the exact value with an underestimation of less than 3%. This result confirms the capability of the Cauchy-Crofton method to estimate the surface area of spherical objects in discrete geometries (Legland et al., 2011). The decrease in resolution tended to modify the grain shape promoting a decrease of S_s. For RF lower than 0.25, the specific surface diverged strongly.

Permeability exhibited an increasing trend with decreasing RF for both materials (Fig. 4.3.e) and 4.3.f). An error smaller than 10% of the reference value is observed for RF larger than 0.5 and 0.25 for the Fontainebleau sand and the VPS respectively. This error is significant for smaller RF. The opposite behave between specific surface and permeability is due to the fact that permeability strongly depends on the viscous friction on the solid surface associated with fluid flow. Less specific surface means less friction leading to an increment in permeability. However, the relationship between decreasing surface and increasing permeability was not linear. Permeability exhibited a larger change with the reference value than the specific surface,

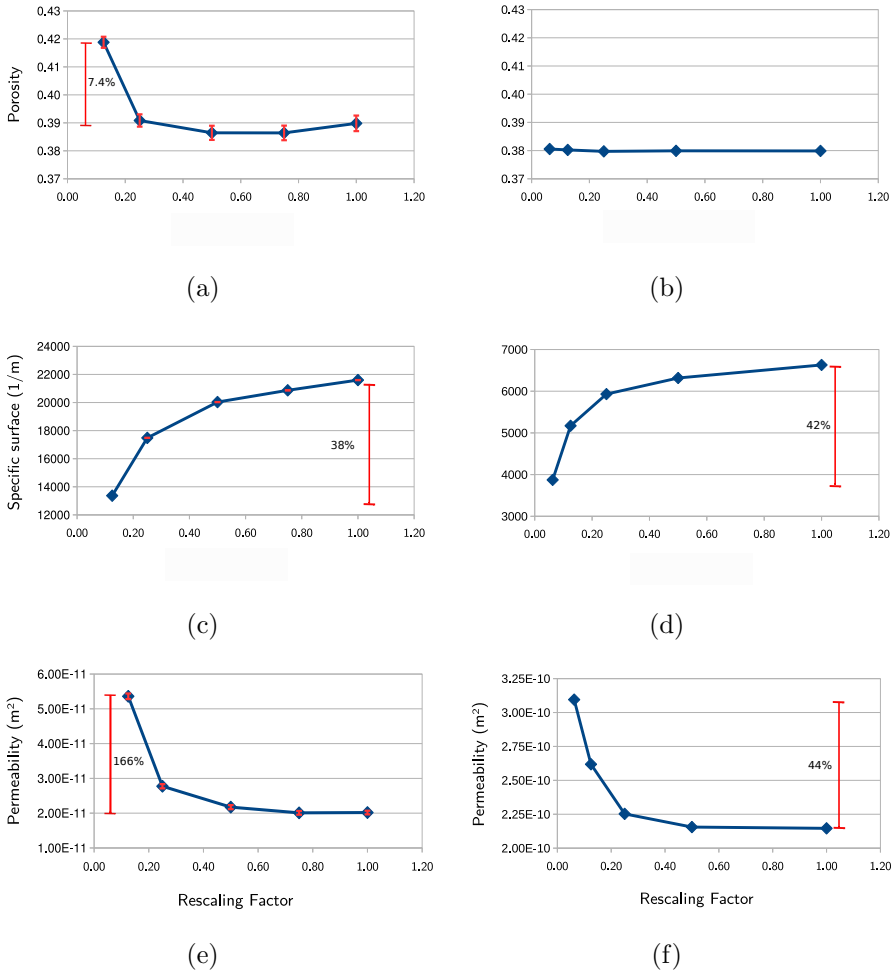

Figure 4.6: Porosity, specific surface and permeability at different RF for Fontainebleau sand (a,c,e) and the virtual pack of sphere (b,d,f).

up to 166% for Fontainebleau sand and 48% for the VPS. The effect of flow computation on a very coarse mesh probably contributed to this larger deviation of permeability values at low resolution.

These results show a noticeable effect of the image resolution on specific surface and permeability. However, analyzing the specific surface and porosity of a given image does not provide a straightforward estimate of the quality of the permeability computation. In order to provide a better

insight on the effect of the microstructure on the permeability computation, a deeper analysis of the pore size distribution and flow distribution within the pore volume was performed.

4.3.2 Analysis of pore size distribution

In Fig. 4.7.a and 4.7.b the cumulative PSD is plotted as a function of the pore diameter for the Fontainebleau sand and VPS respectively. Depending on the RF under consideration the pore size classes were ranging from 9 μm (which at the best scale represents the smallest possible SE) to 180 μm for the Fontainebleau sand. The mean pore diameter D_{50} was 46 μm and the ratio between the mean pore diameter and the mean grain diameter ($\frac{D_{50}}{d_{50}}$) was 0.22. The corresponding values for the VPS were a range from 15 μm to 450 μm; D_{50} was 190 μm and $\frac{D_{50}}{d_{50}}$ was 0.43. The very loose state of the VPS promoted the presence of larger pores in the VPS compared to the Fontainebleau sand.

For Fontainebleau sand, a very good agreement was observed for RF between 0.5 and 1. For RF = 0.25, the small underestimation of the pore volume contained in pores sizes between 50 μm and 80 μm was due to the lack of available SE in this range. In the worst resolution case (RF = 0.125), the cumulative pore size distribution clearly deviated from the reference case: A translation toward the larger sizes of pore was observed and more than 60% of the pore volume was contained in pores smaller or equal to 72 μm, corresponding to one or two voxels in diameter. This behavior was due to the loss of accuracy in the geometrical description of the surfaces of solid grains. Rescaling and segmentation processes tend to promote the merging of solid grains. On the other hand, since the total porosity was well preserved, larger pores tended to be overestimated corresponding to an effect of coalescence of pores. The VPS exhibited a very similar trend with a good agreement for all RF. However, at the worst resolution (RF = 0.0625), the PSD was only composed of three points depicting the loss of details in the pore morphology.

These results prove that rescaling mostly preserved the distribution of pore sizes until very low resolutions. The good agreement between PSDs computed for the range of RF suggests that the error in permeability observed at low RF was not mainly related to a degradation of pore size distribution

with decreasing resolution. In order to obtain a better understanding of the effect of image resolution on the permeability computation, we plot the PSD with respect to the number of voxels per pore diameter (Fig. 4.7.c and 4.7.d respectively).

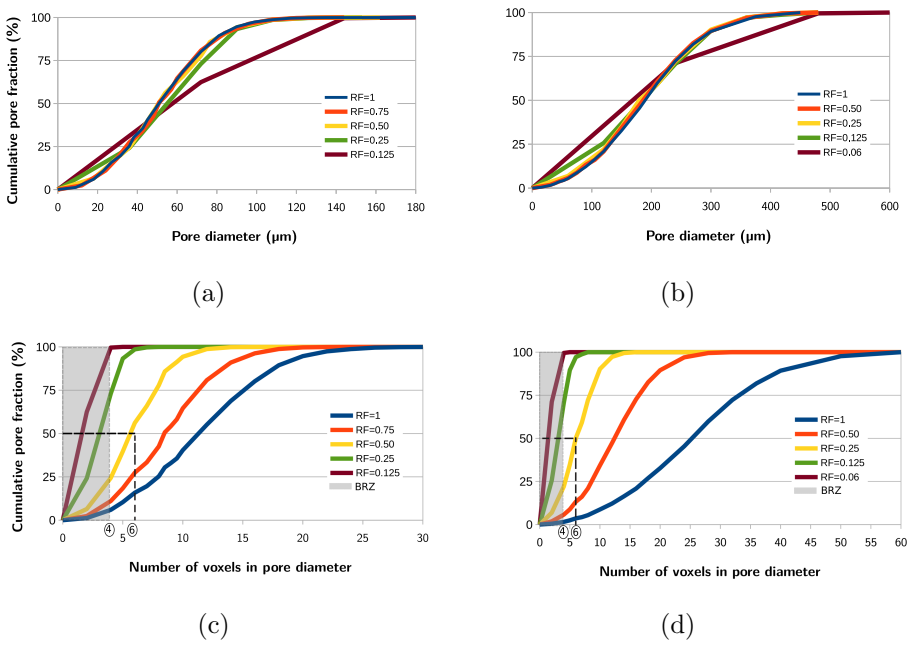

Figure 4.7: Cumulative pore volume fraction in function of the dimensional pore size (a,b) and adimensional pore size (c,d). BRZ is the zone of bad resolution.

The behavior of the cumulative pore volume fraction as function of number of voxels in pore diameter at the original scale image was similar to Fig. 4.7.a and 4.7.b respectively.

The fraction of the pore volume described by a small number of voxels per diameter increased as the RF decreased. This means that with decreasing resolution, the pores were described with less voxels. Steeper curves correspond to a loss of detail.

On one hand, for the lower RF (0.125 and 0.25 for the Fontainebleau sand

and 0.0625 and 0.125 for the VPS) associated with 20% to 166% error in permeability, more than 70% of the pore volume was contained in pores with diameters smaller or equal to four voxels. The low resolutions did not allow a satisfying description of the pore geometry and promoted a very coarse mesh, leading to a loss of accuracy of the numerical method. On the other hand, RF ≥ 0.5 for the Fontainebleau sand and RF ≥ 0.25 for the VPS were associated with an error $\leq$ 10% in the permeability estimate (Table 4.2). Considering this error acceptable, it could be noticed that less than 25% of the pore volume was contained in pores with four voxels or less in diameter (24.38% for Fontainebleau sand and 22.08% for VPS), i.e. $D_{25} > 4$ voxels, and the D_{50} corresponded to about six voxels for both materials.

The last two observations indicate which pore sizes are necessary to achieve acceptable permeability calculations. However, in order to confirm this observation, a new analysis of the distribution of flow field per pore class is proposed in the next section.

4.3.3 Distribution of flow between pore size classes

Eq. 4.7 was solved numerically to obtain the flow rate associated with each pore class. The velocity field was extracted from the flow computation results (the velocity component u_z is in the pressure gradient direction [Fig. 4.8.b]) and the index ψ_i was assigned to to each voxel in a 3D map of the VOI (Fig. 4.8.a), during the morphological closing computation. The cumulative flow rate distribution was then plotted as a percentage fraction of the total flow rate Q for the Fontainebleau sand and the VPS at each RF (Fig. 4.9.a and 4.9.b).

When compared to the cumulative pore fraction (Fig. 4.7.c and 4.7.d), the cumulative distribution of flow rates tended to be higher in pores of larger diameters. Mean diameters, containing 50% of the flow rate, were 60 μm and 220 μm for the Fontainebleau sand and the VPS respectively which was larger than D_{50} (respectively 46 μm and 190 μm). In other words, more than 50% of the total flux occurred in pores larger than D_{50} thus giving more weight to well described pores.

It is interesting to analyze how the flow distribution supports the observations about the PSD described in the last section. Main attention was

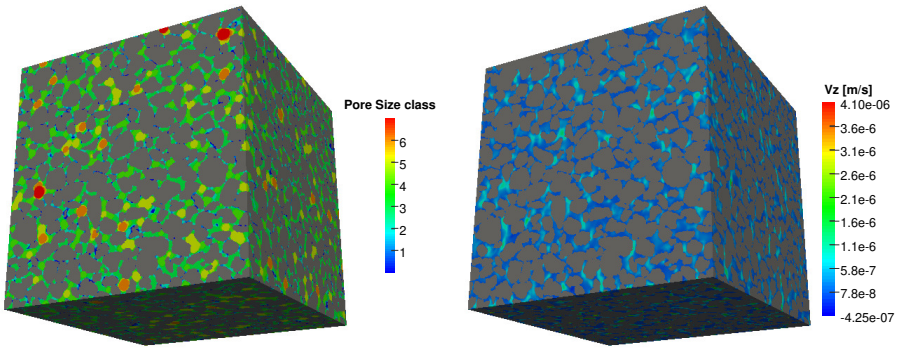

(a) 3D map of pore class indexes ψ_i (b) 3D map of velocity u_z

Figure 4.8: Pore class indexes map and velocity field for the Fontainbleau sand at RF = 0.5

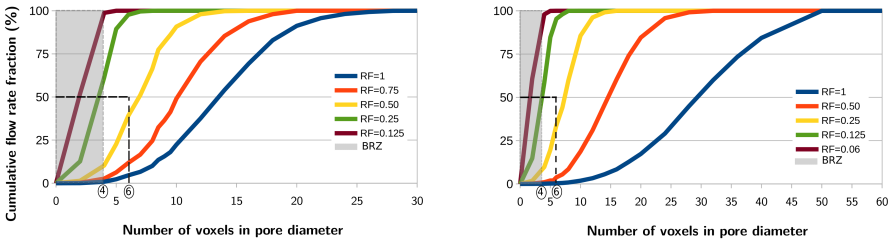

(a) (b)

Figure 4.9: Cumulative flow rate fraction as function of the adimensional pore diameter: for (a) the Fontainebleau sand, and (b) VPS. Where BRZ is the zone of bad resolution

paid to pores with diameters smaller or equal to four voxels. For cases of a poor permeability estimates, most of the flow occurred in these pores in the Fontainebleau sand (with 61.3% and 99% of the flux for RF of 0.125 and 0.25 respectively) and in the VPS (with 58.4% and 97% of the flux for RF of 0.0625 and 0.125 respectively). Meaning that more than 50% of the flux occurred in pores badly described. On the contrary, for cases of good permeability estimates, less than 10% of the total flux occurred in these pores. In the lower acceptable RFs cases (RF = 0.5 for Fontainebleau sand and

RF = 0.25 for VPS), this contribution was 10.25% and 9.75% respectively. Since the small pores promote higher viscous friction (or head loss), the flow then tends to favor the easier paths. Even if this effect is relatively small, this property limits the effect of numerical errors that occurred mainly in small pores due to their bad discretization. For lower RF, most of the flow occurred in badly discretized pores. In this situation, errors in the numerical solution of Stokes equation probably increased resulting in an overall decreased quality of the flow solution.

4.3.4 Proposition of a scan quality criterion for permeability computation

The previous comments denote that the cumulative PSD, can be used to decide if a 3D scan of a studied granular media is suitable to perform a reliable computation of permeability. A quality criterion based on this property benefits from the much lower numerical cost of PSD computation compared with that of permeability computation.

We propose that the following two characteristics have to be fulfilled to achieve an accurate computation of permeability:

- D_{50} should correspond to a number of voxels large enough to ensure a satisfying description of the pore space. For both studied granular materials, D_{50} should be larger or equal to six voxels.
- The volume fraction of pores badly described should not exceed 25% of the total volume in order to limit their contribution to less than 10% of the total flow rate. For both studied granular materials, D_{25} should be larger or equal to four voxels.

Following these rules, the suitable resolution estimated for Fontainebleau sand description was about 10 μm and 30 μm for the VPS. For Fontainebleau sand and VPS, the d_{50} was thus 20 and 14 times the minimum resolution respectively. This indicates that a material whit a looser grain packing (and a simpler grain geometry in our case) can be scanned at a lower resolution, relatively to its grain size, because it presents a comparatively more opened pore space. Our study suggests a slightly less restrictive condition than the criterion proposed by (Al-Raoush et al., 2003). They suggested that a ratio of 25 was required to preserve accurately the pore

throat morphology. On the contrary, it is more restrictive than the ratio of 10 proposed by (Lehmann et al., 2006) for preserving PSD. One should note that PSD computed for Fontainebleau sand at RF = 0.25 and VPS at RF = 0.125, with respective ratio of 10 and 7, were also in good agreement with the reference. Computing of permeability clearly requires a better resolution determining the PSD, which is supported our proposed criterion for D_{25}.

4.4 Conclusions

We studied the effect of X-ray CT resolution on the quality of permeability computation based on direct numerical simulation for granular soils. The particular case of a finite difference approach considering the image voxels as computational mesh was considered with the FlowDict module of the GeoDict software package. In this situation, the decrease in resolution promoted both a degradation of the pore space geometry description and an increase of badly resolved pores promoting numerical errors. The sample of Fontainebleau scanned with X-ray CT and the VPS behaved very similar. Computing permeability proved to be reliable for a wide range of resolutions. An inverse relationship between permeability and specific surface was found. However, the specific surface was not suitable as a quality estimator for computing permeability computation. Instead a detailed analysis of the PSD was used. Provided that the pore diameter D_{50} was larger than six times the image resolution, permeability was calculated with an error smaller than 10% was observed on the permeability value. Analyzing the flow rate distribution in the different classes of pore size explained permeability results: For the lower resolution with an error in permeability lower than 10%, pores discretized by four or less voxels in diameter only drove 10% of the total flow even if they represent 25% of the pore volume ($D_{25} = 4$ voxels). Considering the very good connectivity of the studied granular materials, this limit corresponded to a situation where the water flux mainly occurred in well discretized pores, the higher friction in small pores limited the amount of flow occurring in these regions. The good agreement between results obtained for the real geometry of Fontainebleau sand and for the synthetic data of VPS suggests that the proposed criterion can be applied to fully resolved scans of granular media. Its validity concerning more structured soils should be the subject of further studies.

4.5 Acknowledgements

This study was supported by the PROTINUS funded in the framework of the European Union's Horizon 2020 research. It benefited from a PhD Grant from the CONACYT reference no. 240912/383935. The authors thank Eric Vincens, Professor at École centrale Lyon, for supplying the file used to generate the Virtual Pack of Sphere. permeability computations were performed using the FlowDict module of the Geodict software package. The paper benefited from very constructive contributions of reviewers and the associate editor.

4.6 Conflicts of Interest

The authors declare no conflicts of interest.

Appendices

A REV

The REV was defined as the volume of heterogeneous material that is sufficiently large to be statistically representative of the complexity of the porous structure i.e., to effectively include a sampling of all micro structural heterogeneities that compose the porous medium (Kanit et al., 2003). The SREV is then supposed to be achieved when the standard deviation of the distribution is smaller than an arbitrarily chosen value (Calonne et al., 2012; Yoon and Dewers, 2013; Rozenbaum and du Roscoat, 2014). Both the REV and its approximation by SREV depend on the property under consideration. It tends to be smaller for a geometric property (Porosity, specific surface,..) than for a flux property (permeability, diffusivity,...) (Guibert et al., 2015a).

A SREV analysis was performed on the porosity of the Fontainebleau sand at the best resolution (RF = 1). For the analysis five different sizes of sub

volumes of interest (SVOI) were chosen ranging from 450 μm to 1350 μm (from the (5.4x5.4x5.4 mm) image originally obtained from the tomograph). The porosity, ϕ, was calculated in the full volume providing a reference value = 0.39. The position of each SVOI was then determined stochastically in the full volume. For each SVOI, the porosity, ϕ_i, was calculated as well as, the porosity average $\langle\phi\rangle$ and the standard deviation $\sigma(\phi)$ of the SVOIs distribution. This calculation was iterated until the difference between the calculated average $\langle\phi\rangle$ and the reference value ϕ was lower than 1%.

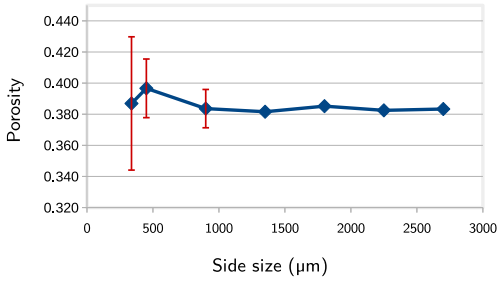

Figure A: SREV analysis on the porosity of Fontainebleau sand

The standard deviation $\sigma(\phi)$ appeared to decrease progressively with increasing SVOI size (Fig. A). It was approximately 5% of the average value for a SVOI of 450 μm reflecting a relatively low discrepancy and a satisfying representativeness. For a SVOI of size of 1350 μm, which was a quarter part of the VOI side, the standard deviation $\sigma(\phi)$ was below 0.25% of the average value.

Chapter 5

Effect of the μCT resolution on the numerical simulation of the transport of a tracer

Keywords : Advection-diffusion, Digital Rock Physics

5.1 Introduction

Solute transfers in underground water are of main interest in a wide range of situations. In the case of aquifer pollution, understanding and predicting the spreading of solute and its interactions with the solid matrix is crucial to elaborate strategies in order to preserve the water resource and drinking water production facilities (Keesstra et al., 2012). The design of remediation systems such as Permeable Reactive Barriers strongly relies in transport modelling both at the scale of the contaminated aquifer and at the scale of the barrier itself (Wanner et al., 2012; Weber et al., 2013). In the field of agronomy, the fate of nutrients and herbicide strongly depends on the combination of water flow conditions and the nature and structure of soils (Vanclooster et al., 2005; Puckett and Hughes, 2005). Recent soil engineering processes such as bio-induced calcite precipitation is also an example where the transport of solute drives the efficiency of the resulting soil reinforcement (Barkouki et al., 2011).

The classical modeling approach for such processes is based on the use of macroscopic models for porous media including Darcy's law for flow and advection-dispersion equation (macro-ADE) for solute transport. The underlying complexity of the pore system is described by the permeability and the dispersion coefficient which are effective properties of the porous medium. The estimation of such properties is generally based on the analysis of laboratory scale experiments or on the solution of inverse problems using field monitored data.

Reliable measurement or prediction of dispersivity is fundamental to the simulation of solute fate and transport. Many studies have aimed at identifying relationships between dispersivity and morphological properties of the porous medium, both theoretically and empirically (e.g (Passioura and Rose, 1971; Klotz and Moser, 1974; Brusseau, 1993)). For granular media, it is well established that dispersivity is mainly dependent on the mean grain diameter (Bear, 1972).

In a more fundamental point of view, these macroscopic models and their effective properties could be derived from the equations of fluid mechanics applied at the pore scale using scale change methods such as volume averaging (Whitaker, 2013) or homogenization (Auriault et al., 2010; Bruining et al., 2012). These equations have the benefit to use only well established thermodynamic properties: The fluid density and viscosity in the Stokes equation of flow and the molecular diffusion coefficient in the advection-diffusion (micro-ADE) equation of solute transport. Classical scale change methods aim at estimating effective properties, but avoid solving explicitly pore scale equations since their mathematical developments include a step of "small" terms neglected. Concerning the transport equation, the volume averaging method leads to the definition of a stationary vectorial closure problem. This problem could be solved numerically and has been used to analyze processes in 2D or simple 3D periodic geometries. More recently, it has been applied to realistic geometries obtained from pore scale imaging (Yang et al., 2016a).

In the last decade, the development of imaging techniques, specially X-ray computed tomography (CT), associated with the increase of computational power opened new perspectives in the field of porous media study. X-ray CT produces 3D images of the internal structure of porous media. Applying

image analysis techniques allowed computing morphological properties of soils such as porosity, specific surface, pores size distribution or pore connectivity (REF). More recently, direct numerical simulation methods have been applied to X-ray CT images in order to simulate flow and transport processes (Bultreys et al., 2016). Being the Stokes equation linear, the flow equation could be solved in stationary condition using Finite Difference (FD, (Wiegmann and Bube, 2000a)), Finite Volume FV, (Guibert et al., 2015a), Lattice Boltzmann Method (LBM, (Khan et al., 2012)) or Smooth Particle Hydrodynamics SPH, (Dal Ferro et al., 2015). The average flow velocity could then be selected by a simple scaling of the velocity field. Less attention has been given to the simulation of transport since its unstationary nature requires a stronger numerical effort. One approach combines a Lagrangian description of advection combined with a random walk algorithm to mimic diffusion (Bijeljic et al., 2013b). It has been recently coupled with a reaction model (Alhashmi et al., 2015). A more straightforward approach is based on the FV method which benefit from a direct derivation from the micro-ADE equation provided. However, the treatment of advection with FV method requires a particular care, such as total variation diminishing (TVD) scheme, to prevent numerical diffusion (Zaretskiy et al., 2010a). This approach is also well adapted to take into account custom reaction terms (Jiang and Tsuji, 2014). These simulations could be used to estimate the corresponding effective properties but also to provide a detailed description of the pressure, velocity and concentration fields inside the pore system (Ovaysi and Piri, 2011). Understanding the local distribution and dynamics of concentrations in real geometries provides an interesting insight on the origin of dispersion. It is also a requirement to describe accurately heterogeneous reactions since these reactions are generally strongly influenced by the transport of reactants and products close to the solid surfaces.

An X-ray CT image is characterized by its resolution, i.e. the size and number of its constitutive voxels. In order to be reliable, the computation of morphological or transport properties of a porous medium requires a resolution high enough to capture accurately the complexity of surface and pore structure. It should also allow studying a sample volume large enough to ensure its representativity, i.e. to capture the heterogeneity of the pore system. The effect of X-ray CT resolution on morphological properties and permeability estimation has been the topic of several studies (Al-Raoush and Papadopoulos, 2010). Concerning granular media, it allowed the definition

of quality criterion based on grain size distribution (Kumar et al., 2010a; Vogel et al., 2010; Yoon and Dewers, 2013; Shah et al., 2016). Concerning granular media, it allowed the definition of quality criterion based on grain size distribution (Al-Raoush and Willson, 2005; Lehmann et al., 2006; Ramírez et al.). To our knowledge, the case of transport simulation did not received a similar attention.

In this study, a sample of Fontainebleau sand was scanned at 4 resolutions. In addition, the best resolution image was numerically scaled to 4 lower resolutions. The morphology and permeability was computed for each image in order to provide a first insight on the effect of the scan resolution. The computation of virtual tracer tests were then performed in order to analyze the transport process and to assess the behavior of the dispersivity with respect to the resolution.

5.2 Material and methods

This study followed the previous work of (Ramírez et al.) that was dedicated to analyzing the effect of X-ray CT resolution on the estimation of permeability. Where the Fontainebleau sand sample under consideration was already studied extensively with respect to its morphological properties and permeability.

5.2.1 Sample description X-ray CT acquisition and image processing

The granular material studied here was a sample of Fontainebleau NE34 sand. It is a fine well graded sand of uniformity coefficient 1.6 with D_{50} = 210 μm, $D_{10} \approx 100$ μm and $D_{100} < 450 \mu m$ (where $d_x = y$ means that the $x\%$ of pores have a diameter size of y). A cylindrical PEEK cell (inner radius $\approx$ 7 mm, wall thickness $\approx$ 0.65 mm and height $\approx$ 7.5 mm) full of dry sand was scanned at the laboratory tomograph EasyTom XL (RX Solutions) at University Grenoble Alpes.

The sample was scanned at four resolutions corresponding to four increasing voxel sizes: 4.5 μm, 6 μm, 9 μm, and 18 μm; which will be referenced as "CT scaling" with rescaling factor RF=1, RF=0.75, RF=0.50, and RF=0.25

RF	Voxel size (mm)	X-ray source	Tube voltage (kV)	Tube current (mA)
1	4.5	LaB6	70	67
0.75	6	W	70	142
0.5	9	W	70	142
0.25	18	W	70	142

Table 5.1: Settings for X-ray CT scans

respectively.

The table 5.1 sums up the settings for each scan. One should note that the apparatus was switched to a LaB6 X-ray source with specific current and voltage to obtain the best resolution image. In all cases, a 1mm aluminum foil was used as physical filter in front of the source. Each image acquisition sequence consisted of 1600 projections of 2084 x 2084 voxels.

The 3D reconstruction stage was based on a cone-beam algorithm. The resulting 3D gray-scale images was treated using enhance contrast and a median filter (Imagej 2.34 software). A cubic volume of interest (VOI) of 2.7 mm (i.e. 600 voxels at RF =1) was extracted in the center of the initially cylindrical sample. A second set of images was created applying the rescaling[1] treatment (Shah et al., 2016) to the best resolution image. This numerical rescaling was performed using the 3D bicubic interpolation algorithm (Imagej 2.34 software). It consisted of four images with RF = 0.75, RF = 0.50, RF = 0.25 and RF = 0.125. The same VOI imaged at 4 resolutions with CT scaling and 4 resolutions with numerical scaling constitutes the material used for all the proposed analysis (see example on Fig. 5.1). Each image thus was segmented in two phases (i.e. void and solid) using the default Isodata algorithm of the software Imagej 2.34 (Ridler et al., 1978).

[1]Rescaling or resizing is the process of increasing or decreasing the number of pixels in an image or voxels in a volume. This process is not lossless. Rescaling a volume to a smaller number of voxels, and then rescaling it back to the original resolution, results in an image sightly different from the original one (Danahy et al., 2007).

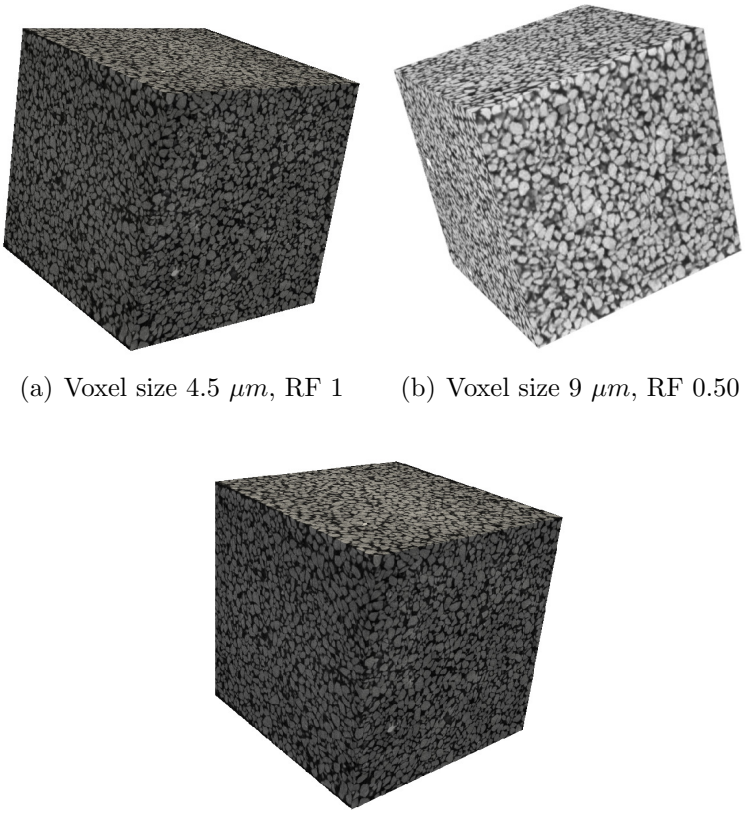

(a) Voxel size 4.5 μm, RF 1 (b) Voxel size 9 μm, RF 0.50

(c) Voxel size 9 μm, RF 0.50

Figure 5.1: Example of 3D gray scale images: 5.1(a) RF = 1 5.1(b) RF = 0.5 (μCT scaling) 5.1(c) RF = 0.5 (numerical rescaling).

5.2.2 Morphological properties, permeability and flow field

The detail of numerical procedures used to analyze the morphology and the permeability of the sample can be found in (Ramírez et al.). The porosity was computed by a simple counting of void voxels. The specific surface was estimated with the discrete extension in 3D of the integral geometry theorem of Cauchy Crofton (Lehmann and Legland, 2012). The pore size distribution was computed using a sequential application of the morphological closing algorithm (Muñoz-Ortega et al., 2015). The computation of the flow field inside the void volume of the sample was performed using the FlowDict

module of the GeoDict software package. This software solves the classical set of Stokes equations in steady state condition :

$$\Delta \cdot \mathbf{u} = 0 \tag{5.1}$$

$$\mu \Delta^2 \mathbf{u} = -\Delta P \tag{5.2}$$

where $\mathbf{u}$ [m/s] is the pore scale velocity field, P [Pa] is the pressure and μ [= 1.005 Pa/s] is the dynamic viscosity of water.

Uniform pressures were applied on the inlet and outlet faces of the sample in order to impose a pressure difference ΔP of 0.02 Pa. Periodic conditions were imposed on lateral faces. No slip boundary conditions were imposed of internal solid/void interfaces. The numerical solver, called Explicit Jump-Stokes solver (Wiegmann and Bube, 2000b), uses the image voxel as mesh element. The pressure P is computed in the center of each voxel while each component of the velocity vector is computed in the center of voxel faces. This staggered grid configuration associated to uniform voxel sizes makes the FD approach congruent with FV. The solver is based on the decomposition of the Stokes problem (equations 1 and 2) into four Poisson problems. They are solved iteratively using a Fast Fourier Transform-based algorithm (Wiegmann, 2007). An explicit jump immersed boundary method is used to impose accurately the no-slip boundary condition (Rutka, 2008). In this study, a strong convergence criterion was selected in order to reach a voxel relative mass balance lower than 10^{-6}. It was chosen in order to limit mass balance error in the treatment of advective fluxes in the tracer transport simulation. The velocity field was integrated numerically in order to estimate the flow rate Q in the sample. A straightforward use of Darcy law then allowed the computation of the intrinsic permeability k $[m^2]$:

$$k = \frac{\mu Q L}{S \Delta P} \tag{5.3}$$

Where S $[m^2]$ is cross-section area orthogonal to the average pressure gradient and L $[m]$ is the distance between the inlet and outlet faces.

5.2.3 Computation of tracer transport numerical column test

The Advection diffusion equation (5.4) is solved numerically into the porous structure of the studied granular media :

$$\frac{\partial c(\mathbf{x},t)}{\partial t} + \nabla \cdot (c(\mathbf{x},t)\mathbf{u}) = \nabla \cdot \mathbf{D}_0 \nabla c(\mathbf{x},t)) \tag{5.4}$$

where c is the solute concentration, $\mathbf{x}$ is a coordinate vector, D_0 $[m^2/s]$ is the molecular diffusion coefficient, and $\mathbf{u}$ [m/s] is the velocity field obtained from the Stockes Equation. The initial concentration is $c(t=0)=0$. The associated boundary conditions are:

- Imposed concentration on the inlet face

$$c|_{in} = c_0 \tag{5.5}$$

  Where c_0 is set to one during the tracer injection time, then to zero till the end of the test.

- Free flow at the outlet which remains the more natural way to impose the tricky outlet boundary condition

$$D_0 \nabla c \cdot \mathbf{n}|_{out} = 0 \tag{5.6}$$

  with $\mathbf{n}|_{out}$ a unit vector normal to the outlet face

- No flux at the solid/void interface taking advantage of the null velocity imposed in Stokes equation

$$D_0 \nabla c \cdot \mathbf{n}|_{wall} = 0 \tag{5.7}$$

  with $\mathbf{n}$ the unit vector normal to the interface

The equation (5.4) is discretized using the FV method. Taking advantage of the linearity of the equation, advective et diffusive terms are solved separately applying the splitting operator technique (Csomós et al., 2005). The advection part is solved using a first order explicit scheme in time which in 1D is writen as.

$$\frac{1}{\Delta t}(c_i^{t+1} - c_i^t) = -\frac{1}{\Delta x_i}[j^t_{adv_{i+1/2}} - j^t_{adv_{i-1/2}}] \ . \tag{5.8}$$

The fact that the advection equation is a conservation equation means that c_i can only be modified by exchanges with the neighboring cells. Therefore, the change in c_i can be seen as in- and out- fluxes through the cell interfaces. Therefore $j^t_{adv_{i+1/2}}$ and $j^t_{adv_{i-1/2}}$ are the flux at the cell interface at time t.

A total variation diminishing (TVD) method is used to ensure a second order scheme in space in the smooth regions to limit numerical diffusion. It degrades to first order near discontinuities in order to prevent non-physical oscillations.

$$j_{adv\,i+1/2} = j^L_{adv\,i+1/2} + \Psi_{i+1/2}\left(j^H_{adv\,i+1/2} - j^L_{i+1/2}\right) \ , \tag{5.9}$$

where $j^H_{adv\,i+1/2}$ is the high order numerical flux, $j^L_{adv\,i+1/2}$ is the low order numerical flux and $\Psi_{i+1/2}$ is the flux limiter. Which in function of the neighbor solutions allows the flux be high or low order. Therefore, the limiter $\Psi_{i+1/2}$ depends locally on a nonlinear function Θ_{i+1}, which is the ratio of solution slopes at the neighborhood of the interfaces in the upwind direction (see Smaoui et al. (2008)).

$$\Theta^t_{i+1/2} = \begin{cases} \frac{c^t_i - c^t_{i-1}}{c^t_{i+1} - c^t_i} = \Theta^+_{i+1/2} & \text{if } u^t_{i+1/2} \geq 0 \\ \frac{c^t_{i+2} - c^t_{i+1}}{c^t_{i+1} - c^t_i} = \Theta^-_{i+1/2} & \text{if } u^t_{i+1/2} < 0 \end{cases} . \tag{5.10}$$

The limiter function is constrained to be greater or equal to zero, i.e., $\Psi(\Theta) \geq 0$. Therefore, when the limiter is equal to zero (sharp gradient, opposite slopes or zero gradient), the flux is represented by a low resolution scheme. Similarly, when the limiter is equal to 1 (smooth solution), it is represented by a high resolution scheme. The limiter here implemented was Superbee:

$$Superbee: \ \Psi(\Theta) = max(0, min(1, 2\Theta), min(2, \Theta)). \tag{5.11}$$

As can be seen in (Dubois, 2010), a convenient scheme can be defined as:

$$c^t_{i+1/2} = \begin{cases} c^t_i + \frac{1}{2}(c^t_{i+1} - c^t_i)\Psi(\Theta^+_{i+1/2}) & u^t_{i+1/2} \geq 0 \\ \\ c^t_{i+1} - \frac{1}{2}(c^t_{i+1} - c^t_i)\Psi(\Theta^-_{i+1/2}) & u^t_{i+1/2} < 0 \ , \end{cases} \tag{5.12}$$

$c^t_{i-1/2}$ is obtained by substituting the index i by $i-1$ in the previous equation. Substituting Eq.(5.10) and Eq.(5.12) into Eq. (5.8)(see Smaoui et al. (2008)):

$$c_i^{t+1} = c_i^t - \frac{\Delta t}{\Delta x}\left(u^t_{i+1/2}c^t_{i+1/2} - u^t_{i-1/2}c^t_{i-1/2}\right). \tag{5.13}$$

which in the 3D case is:

$$\begin{aligned} c_{i,j,k}^{t+1} = c_{i,j,k}^t &- \frac{\Delta t}{\Delta x}\left(u^t_{i+1/2,j,k}c^t_{i+1/2,j,k} - u^t_{i-1/2,j,k}c^t_{i-1/2,j,k}\right) \\ &- \frac{\Delta t}{\Delta y}\left(u^t_{i,j+1/2,k}c^t_{i,j+1/2,k} - u^t_{i,j-1/2,k}c^t_{i,j-1/2,k}\right) \\ &- \frac{\Delta t}{\Delta z}\left(u^t_{i,j,k+1/2}c^t_{i,j,k+1/2} - u^t_{i,j,k-1/2}c^t_{i,j,k-1/2}\right). \end{aligned} \tag{5.14}$$

As a boundary condition we kept c at a constant value at the inflow boundary and allow it to undergo pure advection at the outflow boundary, near the walls there is no BC due to the null velocity imposed at the solid surface, the BC on the side of the domain is periodic to match the BC of the Stokes problem. A high level of convergence is required on the velocity field in order to guarantee the mass balance.

The diffusion part is solved by a first order implicit in time and second in space. Integrating over a control volume the diffusion part of the Eq. 5.4 and applying the divergence theorem leads to the discrete equation:

$$c_{i,j,k}^{t+1} = c_{i,j,k}^t - \frac{\Delta t_{diff}}{\Delta x \Delta y \Delta z}\sum_{face_\lambda}^{6}\int_{S_\lambda} D_0(\nabla c_{i,j,k}\cdot\hat{\mathbf{n}}_\lambda)ds \tag{5.15}$$

where Δt_{diff} is the time step of diffusion, $\Delta x, \Delta y, \Delta z$ are the voxel sizes in the respective direction, and $\mathbf{n}_\lambda$ is the unit normal vector of the λ face. Introducing a linear estimate of diffusive fluxes on each voxel face considering that the average voxel concentration is imposed in the center of each voxel leads to:

$$\begin{aligned} \mathcal{B}c^{t+1}_{i,j,k} &- \mathcal{A}_x c^{t+1}_{i-1,j,k} - \mathcal{A}_x c^{t+1}_{i+1,j,k} \\ &- \mathcal{A}_y c^{t+1}_{i,j-1,k} - \mathcal{A}_y c^{t+1}_{i,j+1,k} \\ &- \mathcal{A}_z c^{t+1}_{i,j,k-1} - \mathcal{A}_z c^{t+1}_{i,j,k+1} = c^t_{i,j,k} \end{aligned} \tag{5.16}$$

where

$$\mathcal{A}_x = \frac{D_0 \Delta t_{diff}}{\Delta x^2}; \qquad \mathcal{A}_y = \frac{D_0 \Delta t_{diff}}{\Delta y^2}; \qquad \mathcal{A}_z = \frac{D_0 \Delta t_{diff}}{\Delta z^2}; \tag{5.17}$$

$$\mathcal{B} = 1 - 2\mathcal{A}_x - 2\mathcal{A}_y - 2\mathcal{A}_z \tag{5.18}$$

It can be noticed that no flux BC simply corresponds to null value of A_i associated to wall our outlet voxel faces. The set of discretized diffusion equation (5.16) for all the pore voxels generates a large linear system of equations:

$$\mathbf{A}\mathbf{c}^{t+1} = \mathbf{c}^t \tag{5.19}$$

with $\mathbf{A}$ a $(N_x N_y N_z)^2$ sparse matrix with 7 non zero diagonals. Taking advantage of the constant nature of the matrix, the solver package MUMPS (MUltifrontal Massively Parallel Solver (Amestoy et al., 1998)) was chosen to perform a LU factorization while ensuring an efficient use of the memory and parallel capabilities. This numerically costly factorization step is performed once while initializing the computation. Subsequent calls to the MUMPS package consists in solution steps using the computed LU matrix.

The general work flow of the program is presented in Fig. (5.2). In the initialization step, the 3D segmented image and the corresponding velocity field are read. The diffusion matrix is built and factorized. The CFL condition is a strong constraint on Δt_{adv}. After a sensitivity analysis performed on all the Peclet number range, a ratio of 1000 was chosen between Δt_{adv} and Δt_{diff}. It ensured less than 1% of normalized root mean square deviation compared with the results using $\Delta t_{diff} = \Delta t_{adv}$. The concentration field and relevant integrated values (such as the flux averaged concentrations) are saved along the computation in order to generate numerical breakthrough curves (BTC).

5.2.4 Computation of numerical column experiments

The Fontainebleau sand cubic volume of interest (VOI) of side size $L = 2.7$ mm was studied in eight different configurations: Four images, refereed to as "CT scaling" were directly taken from the μCT with rescaling factors RF=1,

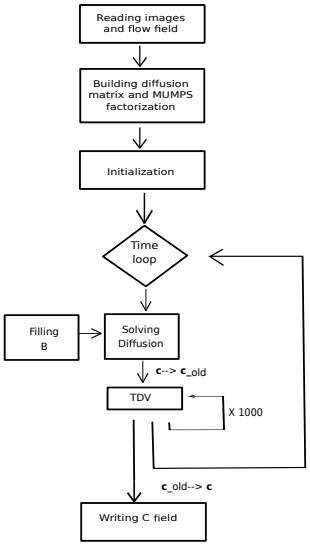

Figure 5.2: Algorithm of the 3D-microADE solver

0.75, 0.50, and 0.25; and four images, refereed to as "numerical scaling", were numerically generated with rescaling factors RF=0.75, 0.50, 0.25, and 0.125. Their analysis is performed in a wide range of Peclet number keeping in mind theoretical and mechanical limitations of the studied material: the flow regime is kept in creeping flow condition (Re $<$ 10) which also corresponds to non soil boiling conditions.

The Peclet number characterizes the relative weight of advection and diffusion processes. It was computed as:

$$Pe = \frac{\langle u \rangle D_{50}}{\phi D_0} \tag{5.20}$$

Where $\langle u \rangle$ [m/s] is average pore velocity, ϕ is the porosity, and D_{50} [m] is the average grain size.

The velocity field obtained from the flow simulations was scaled linearly in order to impose selected value of U_{Darcy} (or average fluid flow Q). Considering an imposed value of the molecular diffusion coefficient $D_0 = 10^{-9} m^2/s$, the numerical breakthrough curves (BTC) experiments were performed

at four different Pe numbers: 165, 16.5, 1.65 and 0.165. The numerical column experiment consisted in applying a step of concentration $c_0 = 1$ in the initially concentration free domain. The concentration was injected during 1 pore volume (PV) and the experiment duration was 3PV (in order to come back to an almost null concentration in the all the pore volume). Thus, the injection time and total duration of the experiment were inversely proportional to selected Darcy velocity. Flux averaged concentrations were explored at three different positions along the VOI in the direction of the flux in order to generate numerical BTC. The positions are called $L_1 = L/4$, $L_2 = L/2$, $L_3 = 3L/4$ and L as can be seen in Fig. (5.3(b)).

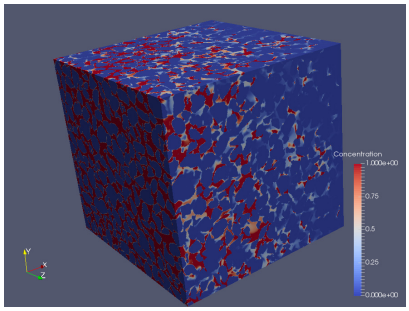

(a) 3D image of the tracer front at 0.5 PV travelling.

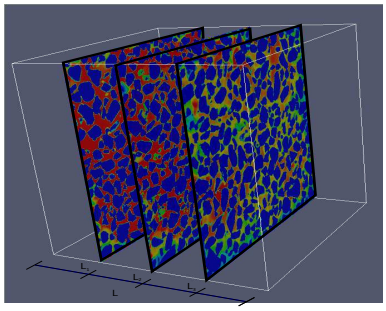

(b) VOI showing the three planes perpendicular to the flux direction.

Figure 5.3: Concentration field for a VOI of 2.7 mm at resolution of 6 μm (RF=0.75).

We obtained BTC at the mentioned locations for each case (Fig. 5.4) except for the RF = 1 except for the RF = 1 where our computational capacity was limited to a maximum length L_1.

The numerical BTC are analyzed in similar way as BTC generated by A column experiment. Where the effective coefficients are computed from the one dimensional macroscale advection dispersion equation (1D-macroADE):

$$\frac{\partial \phi C}{\partial t} = -\frac{\partial C U_{Darcy}}{\partial x} + \frac{\partial}{\partial x}\left(\phi D_h \frac{\partial C}{\partial x}\right) \tag{5.21}$$

Where C is the macroscale concentration, U_{Darcy} [m/s] is the Darcy velocity

in direction of flow x, ϕ is the porosity, and D_h $[m^2/s]$ is the coefficient of hydrodynamic dispersion (and all the quantities are scalars due that it is a 1D equation).

In 3D, the coefficient of hydrodynamic dispersion is a second order rank tensor, classically considered as the sum of effective diffusion reflecting the macroscopic effect of molecular diffusion in the pore space and mechanical dispersion reflecting the fickian (or mixing) effect due to the heterogeneity of the microscale velocity field.

$$\mathbf{D}_h = \tau \mathbf{D}_0 + \alpha \mathbf{U} \tag{5.22}$$

where τ is the tortuosity and α $[m^{-1}]$ is the dispersivity, and $\mathbf{U}$ $[m/s]$ is the pore velocity. In a general context, α should be a tensor including dispersion effect in the transverse direction of flow. In this study, the dispersion is studied only in the longitudinal direction of flow.

From our simulated column experiment, the hydrodynamic dispersion coefficient was estimated using the public domain software Stanmod/CXTFIT 2.0 (Toride et al., 1995). Which uses an analytical solution of the macroADE, this software performs a least-squares minimization inverse problem. On it one column experiment can me analyzed through the information given at one or many output positions. However, because the dispersion depends on the distace traveled by the concentration, we called D_{h_1}, D_{h_2}, D_{h_3}, and $\langle D_h \rangle$ to the hydrodynamic dispersion coefficient computed with the output information at position L_1, L_2, L_3, and with the set of the three output positions respectively.

5.3 Results and discussion

5.3.1 Analysis of the dispersive effect in the sample

In this section are discussed the results obtained for the numerical scaling RF = 0.75, which is the best resolution containing all the cases.

The figure 5.4 presents three groups of BTCs, the first, second, and third group correspond to the simulation output located at positions $L1$, L_2, and

L_3 respectively. The members of these groups are the curves corresponding to Pe=165, 16.5, 1.65 and 0.165.

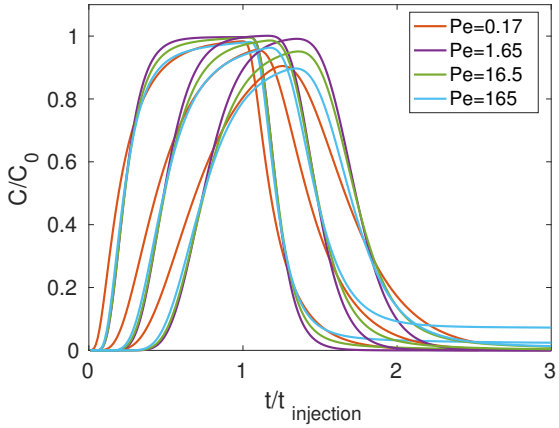

Figure 5.4: Adimensional BTC for a simulation with injection time of 1PV, at four Pe numbers and three outlet locations.

The Fickian effect, i.e., the conjugate effect of diffusion and dispersion, could be identified as the spreading of the BTC and the subsequent decrease of the maximum observed concentration. This fickian behavior appears minimum for Pe = 1.65 which corresponds to a situation where advective and diffusive processes are of the same order of magnitude and is increased as Pe increases. Interestingly, the adimensional behavior observed for Pe = 0.165 and Pe = 165 appears of the same order of magnitude even if the BTC at the lower value appears more symmetrical (or normal). This apparent similitude denotes in practice two distinct behavior. For Pe = 165, the column test lasted only 3.8s, promoting a fickian process driven only by the mechanical dispersion due to the strong heterogeneity of the flow field. On the contrary, for Pe = 0.165, the column test lasted 3800s. In this case the advection and mechanical dispersion processes have a very small effect compared to the molecular diffusion. For Pe = 1.65, the effect of translation due to the advection is non-negligible: the small average velocity tends to limit the mechanical dispersion and the effect of molecular diffusion is less sensitive than for Pe = 0.165 promoting finally a limited spreading of the BTC.

The estimation done with the CXTFIT software of $\langle D_h \rangle$ was performed for Pe=165, 16.5, 1.65 and 0.165 ; shows and increase of $\langle D_h \rangle$ from $6.6110^{-10} m^2/s$ up to $3.7110^{-7} m^2/s$ well scaled with the increase of Pe from 0.165 to 165. In fig. 5.5 is presented together the output of the 3D simulations with the output of the 1D macroADE computed with the corresponding fitted value of $\langle D_h \rangle$ [2]. We observe that the BTCs obtained from the 3D model respect the shape of 1D macro ADE problem. The good general agreement between both models reflects the good quality of the inverse problem fit ($R^2 > 0.989$ in all cases). The studied material did not exhibited abnormal dispersive effects at the pore scale. There is an excellent agreement for $Pe \leq 1.65$, and as the Pe number increases the disagreement grows. It affected more the BTC corresponding to the largest outlet position (L_3). In other words, discrepancies increased with the transport distance and high Pe number. The BTC predicted by the 1D macroADE tended to underestimate the dispersion effect (or overestimate the concentration).

[2]The CXTFIT software has the option to given the effective coefficients of a column experiment, compute the corresponding BTC (direct problem).

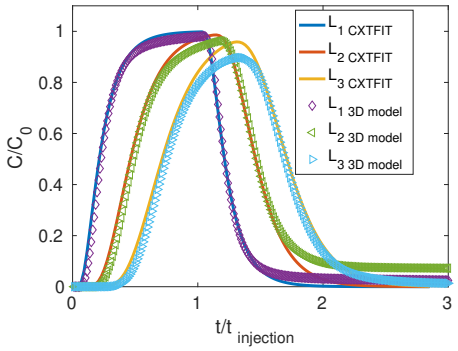

(a) Pe=165, $\langle D_h \rangle = 3.7110^{-7} m^2/s$

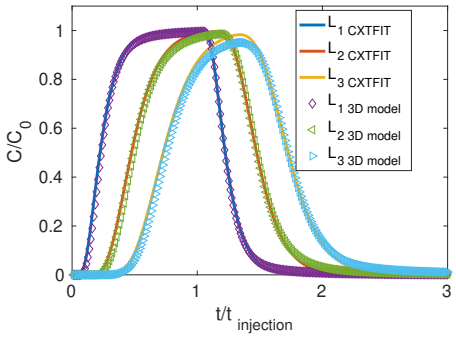

(b) Pe=16.5, $\langle D_h \rangle = 2.5310^{-8} m^2/s$

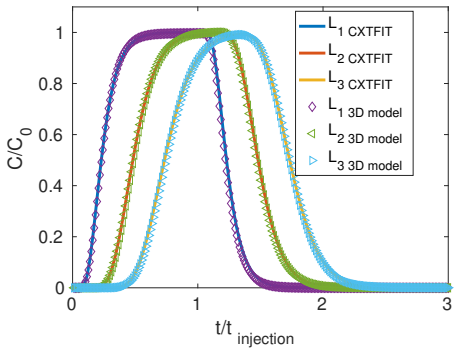

(c) Pe=1.65, $\langle D_h \rangle = 1.9110^{-9} m^2/s$

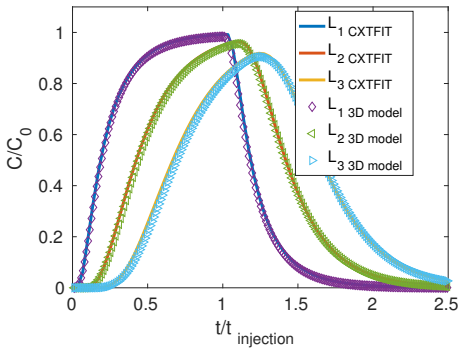

(d) Pe=0.165, $\langle D_h \rangle = 6.6110^{-10} m^2/s$

Figure 5.5: BTC at L1, L2 and L3 for RF = 0.75 with numerical rescaling. With diamonds and triangles are presented the results from the 3D-microADE model, and in continuous lines the results of the 1D macroADE direct problem using the fitted $\langle D_h \rangle$

The Figure 5.6 presents the evolution of $\langle D_h \rangle$ with the Peclet number. The increasing trend presents a linear behaviour around $Pe > 1.65$ reflecting the increase of mechanical dispersion with increasing velocity. The inflection observed at Pe = 0.165 is characteristic of the transition toward the diffusion dominated regime. This behaviour is in perfect agreement with the literature (Saffman, 1960; Bear, 2018). In the linear region $\langle D_h \rangle$ can be identified as $\langle D_h \rangle = \alpha U$. Therefore for $Pe > 1.65$ through the slope and, the associated Darcy velocity it could be identified the material dispersivity as $\alpha = 3.3110^{-4} m$. Which is approximately $1/10^{th}$ of the sample length

(Pickens and Grisak, 1981b). Considering that the mechanical dispersion is negligible at Pe = 0.165, the coefficient of hydrodynamic dispersion $\langle D_h \rangle$ could be identified to the effective diffusion coefficient (τD_0). The material tortuosity τ is then approximately 0.66 which appears also in agreement with a granular media.

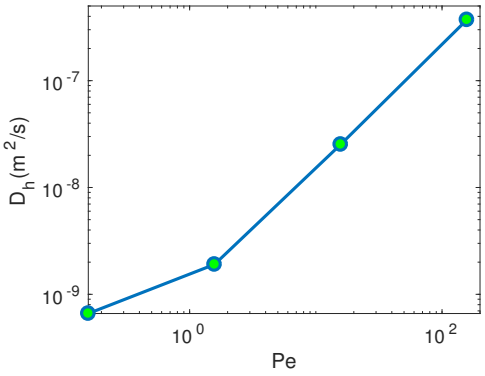

Figure 5.6: Effect of the Pe on $\langle D_h \rangle$ for the numerical scaling at RF = 0.75

In order to get a better insight on the discrepancy between the output of the 3D- microADE and of the 1D-macroADE observed in figure 5.4, each individual BTC was fitted separately, obtaining the corresponding D_{hi}. In figure 5.7 is plotted the error between D_{hi} and the corresponding $\langle D_h \rangle$. Observing no clear trend for Pe = 0.165 and 1.65, remaining around zero with the travel distance. In this case molecular diffusion processes tend to homogenize concentration fields at the pore scale. In the cases for Pe=16.5 and Pe=165 we observer a linear tendency (with $R^2 = 0.97$ and 0.99 respectively), the error is bigger in the extremes but negative for the beginning of the column and positive for the end of the column, the slope of the line is more steep for the biggest Pe number. The increase of dispersion with the travel distance is thus more sensitive as the velocity increase. This observation explains the behaviour observed in Fig. 5.7. Using a single averaged hydrodynamic coefficient thus promote a stronger discrepancy between the 1D-macroADE and the 3D-microADE as the travel distance increase at high Pe numbers.

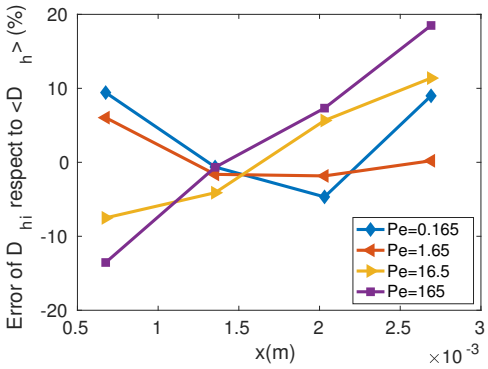

Figure 5.7: Effect of the travel distance on the hydrodynamic coefficient D_h for the studied Pe numbers

5.3.2 Effect of the resolution on the estimation of morphological and transport properties

The main goal of this research is to analyze the effect of μCT resolutions on subsequent computation of morphological and transport properties. The figure 5.8 reports the relative error on the computed properties with respect to the best resolution available value taken as reference. The porosity obviously appeared as the most robust property since it never exhibited more than 15% error. A significant divergence from the reference occurred at RF = 0.25 for the CT scaling and RF = 0.125 for the numerical scaling. Specific surface and permeability (Fig. 5.8.b and 5.8.c respectively) exhibited opposite trend with an increase of specific surface corresponding to a decrease of permeability. This behaviour is coherent with an increase of flow friction on the solid surface. With about 15% error on both quantities, the CT scaling at RF = 0.5 exhibited approximately twice the difference with the reference case observed for the numerical scaling (7% error). Even if the numerical scaling procedure partially mimics the partial volume effect associated with the interface location on μCT images, it is likely that the interpolation procedure used in the scaling process better preserve underlying information than the CT apparatus. A similar trend was reported by (Cooper et al., 2007) in their study of bone morphology.

In the case of numerical scaling, the error associated on D_{h1} compared to the

reference at RF = 1 were plotted on Figure 5.8.e. The behavior at low Peclet number ($Pe \leq 1.65$) could obviously be attributed to the inconsistency of the outlet boundary condition used for the RF = 1 case. The effect of molecular diffusion was predominant in this Peclet regime. The concentration field for RF = 1 was thus strongly influenced by the zero concentration gradient imposed at the outlet. It was thus irrelevant to consider RF = 1 as a reference. However, for higher Peclet numbers ($Pe \geq 16.5$), very good agreement was found for RF as low as 0.25 which exhibited errors of 8% and 12% at Pe = 16.5 and 165 respectively. These errors should be compared with the underestimation of 19% and 37% observed on specific surface and permeability for this RF. Despite an approximate description of the pore space geometry and the velocity field, D_h is estimated with a good accuracy with the numerical scaling at RF = 0.25. However, this observation should be moderated at the lowest Peclet. The figure 5.8.f presents the error on the averaged $\langle D_h \rangle$ with respect to numerical scaling at RF = 0.75. At Pe = 0.25, the error for RF = 0.25 raised up to 18% probably due to the bad definition of pore tortuosity promoting an overestimation of dispersion. The image at RF = 0.125 presented strong errors in all cases. Its geometry simplification promoted an overestimation of molecular diffusion effect at Pe = 0.25 corresponding to an underestimation of the tortuosity effect. At higher Peclet numbers, the mechanical dispersion was underestimated due to the simplification of flow paths.

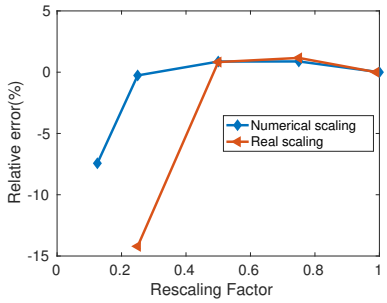

(a) Porosity for the reference value of 0.039

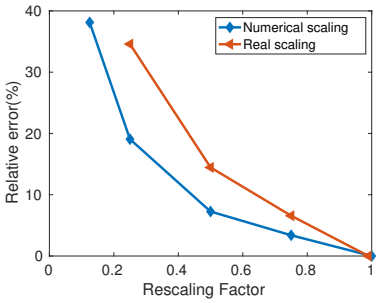

(b) Specific surface for the reference value of 21601 m^{-1}

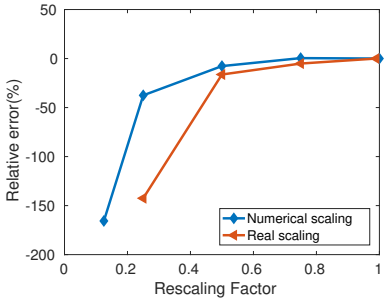

(c) Permeability for the reference value of $2.02 \times 10^{-11} m^2$

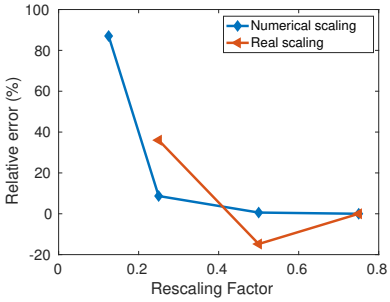

(d) $\langle D_h \rangle$ with respect to RF = 0.75 at Pe = 16.5

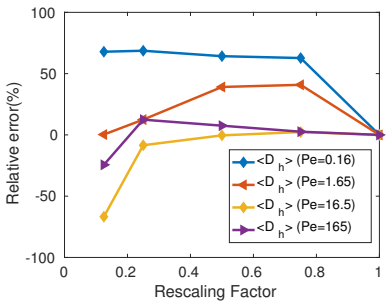

(e) D_{h1} with respect to RF = 1, only numerical scaling cases

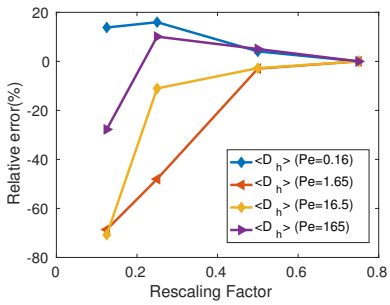

(f) $\langle D_h \rangle$ with respect to RF = 0.75 only numerical scaling cases

Figure 5.8: Relative error on morphological and transport properties with respect to the reference case (RF = 1) [except for (d) and (e) based on RF = 0.75]

Cumulative PSD are plotted on figure 5.9 with respect to the adimensional pore size (i.e. the number of voxels in pore diameter). (Ramírez et al.) put forward that the numerical scaling preserved accurately the shape of the PSD. However, the increase of voxel size associated with the decrease of RF tended mainly to a loss of accuracy in the smaller pore diameters. The CT scaling promoted stronger differences on the PSD shapes for the 3 available RF. One should note that these differencies did not exhibit a noticeable trend while compared to the corresponding numerical scaling. At RF = 0.75 the largest pores were mainly concerned with an underestimation of the volume of pores with diameters between 10 and 15 voxels (i.e. between 60 and 90 μm). At RF = 0.5, the small pores between 2 and 5 voxels (i.e. between 18 and 45 μm) are mainly underestimated by the CT scaling. The PSD of CT scaling at RF = 0.25 clearly put forward a general underestimation of all pore sizes. Changing the resolution on a μCT scanner thus implies noticeable changes of the pore structure which is most likely to promote the discrepancies observed on the computed properties.

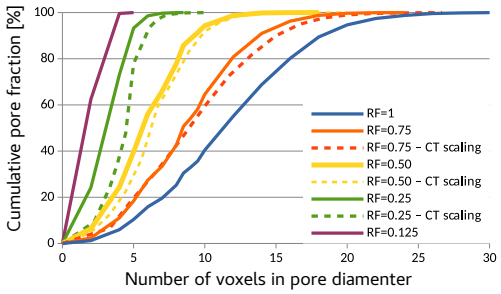

Figure 5.9: Cumulative pore size distribution with adimensional pore size

Based on numerical scaling only, (Ramírez et al.) proposed the following quality criteria to ensure that the error on permeability estimate was lower than 10 % as:

- The median pore size D_{50} should be larger or equal to six voxels to ensure that most of the pore system is well defined.
- The median pore size D_{25} should be larger or equal to four voxels to ensure that numerical errors on Stokes equation did not infer on a significant part of the total flow rate.

The CT scaling case at RF = 0.25 did not match these criteria and is clearly insufficient to perform permeability computation. It also exhibited significant errors concerning the computation of D_h. At RF = 0.75, the criteria were well respected and all the computed properties presented reasonable errors (≤ 10). The CT scaling at RF = 0.5 was clearly at the limit of the quality criteria. The error on specific surface and permeability of about ≤ 15 probably remained acceptable. Once again, the coefficient of hydrodynamic dispersion was estimated with a smaller error than permeability.

5.4 Conclusions

In this paper, a sample of Fontainebleau sand was scanned with a μCT in a large range of resolution. Additionally, the best resolution image had been scaled numerically in order to generate virtual images at lower resolutions. The rationale behind this approach was to study the effect of the scan resolution on the quality of morphological and transport properties. Image morphology concepts were used to compute the porosity, specific surface and pore size distribution of each image. The permeability and pore velocity field were computed using the commercial FV software GeoDict. The Coefficient of hydrodynamic dispersion was estimated based on numerical column BTC experiments performed with a dedicated software. The analysis of theses numerical BTC was performed with the classical inverse problem approach of the Stanmod/CXTFit program.

The dispersive behavior of the sand sample exhibited classical trend including a linear increase of the mechanical dispersion with increasing Peclet number and with increasing travel distance. The rate of increase with the travel distance appeared to increase with the Peclet number. In the diffusion dominated regime, the travel distance did not promote a significant increase of the coefficient of hydrodynamic dispersion.

Both morphological and transport properties exhibited increasing errors as the resolution decreased. The porosity appeared the least affected quantity probably because this property is volumetric by essence and only weakly depends on the pore space configuration. The specific surface and permeability exhibited a coherent opposite trends that could be explained

by the mechanism of fluid friction on the solid surfaces. The computation of the hydrodynamic dispersion coefficient proved to be more robust than the permeability. Even if the flow field is the main driver of dispersion at high Peclet number, the observed error on D_h remained significantly lower than the error on permeability. The FV modelling of transport thus appeared efficient to perform detailed studies of pore scale transport.

Finally, the comparison of μCT images at different resolution exhibited more discrepancy than numerically scaled images. Even if the criteria proposed by (Ramírez et al.) to assess the quality of a given image from its PSD remained globally valid, significant discrepancy had been observed between the scans performed on a single sample of sand. This observation should temper the confidence on μCT images since they could be influenced by the CT apparatus itself but also by the 3D reconstruction or the subsequent segmentation processing step.

5.5 Acknowledgements

This study was supported by the PROTINUS funded in the framework of the European Union's Horizon 2020 research. It benefited from a PhD Grant from the CONACYT reference no. 240912/383935. Permeability computations were performed using the FlowDict module of the Geodict software package .

5.6 Conflicts of Interest

The authors declare no conflicts of interest.

Conclusions and perspectives

In the present thesis the structure of the porous media was studied, particularly on sandy soils and a virtual pack of spheres. Based on bibliographic references we selected and/or generated tools to compute the porous media structural properties such as the porosity, specific surface and pore size distribution.

Porosity was computed with the counting one phase type voxel technique. And for the specific surface, a C code based on the Couchy Crofton method was developed. For the PDS a code in Matlab was written using the morphological operations of closing and image subtraction.

To study flux and solute transport first it was computed the Stokes equation with the FV commercial software GeoDict. We studied the effects of the 3D image resolution on the computation of the permeability. An inverse trend between permeability and specific surface was found.

An original analysis of the flow-rate distribution between the pore size classes was proposed. It allowed us to evaluate the contribution of small, and thus badly discretized, pores on the total flow rate.

These results supported the detailed analysis of the PSD. It was then proposed two conditions to guarantee that the quality of a 3D image is good enough to perform a permeability computation in a granular media. The propositions were:

- D_{50} should correspond to a number of voxels large enough to ensure a satisfying description of the pore space. For both studied granular materials, D_{50} should be larger or equal to six voxels.

- The volume fraction of pores badly described should not exceed 25% of the total volume in order to limit their contribution to less than 10% of the total flow rate. For both studied granular materials, D_{25} should be larger or equal to four voxels.

In a second part, we developed an algorithm to solve the advection diffusion equation at the microscopic scale i.e., directly on the porous media structure. Using the splitting operator we compute the advective part with a Finite Volume (FV) method, implementing a Total Variation Diminishing (TVD) scheme. The diffusion part was computed using a FV method with the assistance of the MUMPS software to solve the resulting linear system. From the concentration field obtained with the algorithm and following a volume averaging method, we computed the macroscopic properties of dispersivity and the hydrodynamic dispersion coefficient for a sample of Fontainbleau NE34 sand. Peclet numbers ranging from 0.165 (diffusion dominant) up to 165 (advection dominant) were considered. We studied the dependence of the computed properties with the image resolution. It appeared that the solute transport macro properties are less affected by a deterioration of the resolution than the flow property of permeability (both cases computed through a FV method applied directly on the image voxels).

Finally, we studied the effect of computing structural and transport properties with numerically rescaled images and with the images directly taken from the μCT. This shows that a numerical rescaled image preserves the behavior of the macroscopic properties more than a real rescaled image. However, the proposed quality criteria appeared reasonable with images directly obtained from the μCT leading to errors on permeability and dispersion coefficient limited under 15%.

5.6.1 Perspectives

- In order to generalize our proposed criteria, it would be enlightening to test it for more granular soils such as soils presenting a spreader PSD. The analysis of finer clayley soil probably remains beyond our computation capability. However, in such cases, it is probably relevant to focus on the macro-porosity (cracks and default behind the clay constituents).

- The microADE solver is currently partially parallelized since the diffusion part is fitted with the MPI capability of MUMPS while the advection part used only OpenMP. A full parallelization of the code should be performed in MPI in order to allow computation on servers with several nodes. In order to share our 3D model a next step would be to developed an adequate interface user/code.

- The natural next step according to the 3D model here developed is to take into account reactive terms, in order to expand the range of usage possibilities. A priority for our team would be to study the transport of bacteria. The microADE is theoretically adequate to model the transport of colloids. Taking advantage of the pore size map obtained from the PSD analysis, the direct geometrical interception of bacteria by pore constrictions could be easily implemented as internal boundary conditions. This process of bacteria collection is very important, for instance, in the process of soil reinforcement by bio-induced calcite precipitation (Béguin et al. (2018)). This engineering technique also rely on calcite formation in the vicinity of the collected bacteria. Modeling this reactive mechanism should also be achievable even if it would require to transport simultaneously Urea, Calcium and ammonia which are the main reactive species and products involved. The algorithm of the transport program should include in such case a reactive term located at the solid/liquid interface that could be ponderated by the previously computed location of bacteria collection.

Bibliography

Pierre Adler. *Porous media: geometry and transports*. Elsevier, 2013.

Mohammad Ali Ahmadi. Connectionist approach estimates gas–oil relative permeability in petroleum reservoirs: application to reservoir simulation. *Fuel*, 140:429–439, 2015.

R.I. Al-Raoush and C.S. Willson. Extraction of physically realistic pore network properties from three-dimensional synchrotron x-ray microtomography images of unconsolidated porous media systems. *Journal of Hydrology*, 300(1–4):44 – 64, 2005. ISSN 0022-1694. doi: https://doi.org/10.1016/j.jhydrol.2004.05.005. URL http://www.sciencedirect.com/science/article/pii/S0022169404002355.

Riyadh Al-Raoush and Apostolos Papadopoulos. Representative elementary volume analysis of porous media using x-ray computed tomography. *Powder technology*, 200(1-2):69–77, 2010.

Riyadh Al-Raoush, Karsten Thompson, and Clinton S Willson. Comparison of network generation techniques for unconsolidated porous media. *Soil Science Society of America Journal*, 67(6):1687–1700, 2003.

Z Alhashmi, MJ Blunt, and B Bijeljic. Predictions of dynamic changes in reaction rates as a consequence of incomplete mixing using pore scale reactive transport modeling on images of porous media. *Journal of contaminant hydrology*, 179:171–181, 2015.

Patrick R Amestoy, Ian S Duff, and J-Y L'Excellent. Mumps multifrontal massively parallel solver version 2.0. 1998.

Heiko Andrä, Nicolas Combaret, Jack Dvorkin, Erik Glatt, Junehee Han, Matthias Kabel, Youngseuk Keehm, Fabian Krzikalla, Minhui Lee, Claudio

Madonna, et al. Digital rock physics benchmarks—part ii: Computing effective properties. *Computers & Geosciences*, 50:33–43, 2013.

Rutherford Aris. On the dispersion of a solute in a fluid flowing through a tube. *Proc. R. Soc. Lond. A*, 235(1200):67–77, 1956.

Jean-Louis Auriault, Claude Boutin, and Christian Geindreau. *Homogenization of coupled phenomena in heterogenous media*, volume 149. John Wiley & Sons, 2010.

Barbora Badalíková. Influence of soil tillage on soil compaction. In *Soil Engineering*, pages 19–30. Springer, 2010.

TH Barkouki, BC Martinez, BM Mortensen, TS Weathers, JD De Jong, TR Ginn, NF Spycher, RW Smith, and Y Fujita. Forward and inverse bio-geochemical modeling of microbially induced calcite precipitation in half-meter column experiments. *Transport in Porous Media*, 90(1):23, 2011.

Tom Batey. Soil compaction and soil management–a review. *Soil use and management*, 25(4):335–345, 2009.

J. Bear. *Dynamics of Fluids In Porous Media*. Number vol. 1 in Dynamics of Fluids in Porous Media. American Elsevier Publishing Company, 1972. ISBN 9780444001146. URL https://books.google.fr/books?id=9JVRAAAAMAAJ.

J. Bear. *Hydraulics of groundwater*. McGraw-Hill series in water resources and environmental engineering. McGraw-Hill International Book Co., 1979. ISBN 9780070041707. URL https://books.google.fr/books?id=N-pOAAAAMAAJ.

J. Bear. *Dynamics of Fluids in Porous Media*. Dover Civil and Mechanical Engineering Series. Dover, 1988. ISBN 9780486656755. URL https://books.google.fr/books?id=lurrmlFGhTEC.

J. Bear and A. Verruijt. *Modeling Groundwater Flow and Pollution*. Theory and Applications of Transport in Porous Media. Springer Netherlands, 1987. ISBN 9781556080142. URL https://books.google.fr/books?id=JqKGPAcpQ7wC.

Jacob Bear. *Dynamics of fluids in porous media*. Courier Corporation, 2013.

Jacob Bear. *Modeling Phenomena of Flow and Transport in Porous Media*, volume 31. Springer, 2018.

Jacob Bear and Yehuda Bachmat. On the equivalence of areal and volumetric averages in transport phenomena in porous media. *Advances in Water Resources*, 6(1):59–62, 1983.

Jacob Bear and Yehuda Bachmat. Transport phenomena in porous media—basic equations. In *Fundamentals of Transport Phenomena in Porous Media*, pages 3–61. Springer, 1984.

Jacob Bear and Yehuda Bachmat. *Introduction to modeling of transport phenomena in porous media*, volume 4. Springer Science & Business Media, 2012.

R Béguin, L Oxarango, L Sapin, A Garandet, A Viglino, E François, H Mora, F Martins, L Duchesne, D Albrecht, et al. Experimental tests of soil reinforcement against erosion and liquefaction by microbially induced carbonate precipitation. In *European Working Group on Internal Erosion*, pages 16–24. Springer, 2018.

Elena M Bennett, Stephen R Carpenter, and Nina F Caraco. Human impact on erodable phosphorus and eutrophication: a global perspective: increasing accumulation of phosphorus in soil threatens rivers, lakes, and coastal oceans with eutrophication. *BioScience*, 51(3):227–234, 2001.

Branko Bijeljic, Ali Raeini, Peyman Mostaghimi, and Martin J Blunt. Predictions of non-fickian solute transport in different classes of porous media using direct simulation on pore-scale images. *Physical Review E*, 87(1): 013011, 2013a.

Branko Bijeljic, Ali Raeini, Peyman Mostaghimi, and Martin J Blunt. Predictions of non-fickian solute transport in different classes of porous media using direct simulation on pore-scale images. *Physical Review E*, 87(1): 013011, 2013b.

Winfried EH Blum. Functions of soil for society and the environment. *Reviews in Environmental Science and Bio/Technology*, 4(3):75–79, 2005.

A Takbiri Borujeni, NM Lane, K Thompson, and M Tyagi. Effects of image resolution and numerical resolution on computed permeability of consolidated packing using lb and fem pore-scale simulations. *Computers & Fluids*, 88:753–763, 2013.

Yuri Boykov and Vladimir Kolmogorov. Computing geodesics and minimal surfaces via graph cuts. In *Computer Vision, 2003. Proceedings. Ninth IEEE International Conference on*, pages 26–33. IEEE, 2003.

GO Brown, HT Hsieh, and DANIEL A Lucero. Evaluation of laboratory dolomite core sample size using representative elementary volume concepts. *Water Resources Research*, 36(5):1199–1207, 2000.

Hans Bruining, Mohamed Darwish, and Aiske Rijnks. Computation of the longitudinal and transverse dispersion coefficient in an adsorbing porous medium using homogenization. *Transport in porous media*, 91(3):833–859, 2012.

Mark L Brusseau. The influence of solute size, pore water velocity, and intraparticle porosity on solute dispersion and transport in soil. *Water Resources Research*, 29(4):1071–1080, 1993.

Tom Bultreys, Wesley De Boever, and Veerle Cnudde. Imaging and image-based fluid transport modeling at the pore scale in geological materials: A practical introduction to the current state-of-the-art. *Earth-Science Reviews*, 155:93–128, 2016.

N Calonne, C Geindreau, F Flin, S Morin, B Lesaffre, S Rolland Du Roscoat, and P Charrier. 3-d image-based numerical computations of snow permeability: links to specific surface area, density, and microstructural anisotropy. *The Cryosphere*, 6:939–951, 2012.

George Chatzigeorgiou, Vincent Picandet, Abdelhafid Khelidj, and Gilles Pijaudier-Cabot. Coupling between progressive damage and permeability of concrete: analysis with a discrete model. *International journal for numerical and analytical methods in geomechanics*, 29(10):1005–1018, 2005.

Guihua Chen, Ray R. Weil, and Robert L. Hill. Effects of compaction and cover crops on soil least limiting water range and air permeability. *Soil and Tillage Research*, 136:61 – 69, 2014. ISSN 0167-1987. doi: https:

//doi.org/10.1016/j.still.2013.09.004. URL http://www.sciencedirect.com/science/article/pii/S0167198713001621.

Veerle Cnudde and Matthieu Nicolaas Boone. High-resolution x-ray computed tomography in geosciences: A review of the current technology and applications. *Earth-Science Reviews*, 123:1–17, 2013.

David Cooper, Andrei Turinsky, Christoph Sensen, and Benedikt Hallgrimsson. Effect of voxel size on 3d micro-ct analysis of cortical bone porosity. *Calcified tissue international*, 80(3):211–219, 2007.

Molly S Costanza-Robinson, Benjamin D Estabrook, and David F Fouhey. Representative elementary volume estimation for porosity, moisture saturation, and air-water interfacial areas in unsaturated porous media: Data quality implications. *Water Resources Research*, 47(7), 2011.

Ronald A Cox and Tracy Nishikawa. A new total variation diminishing scheme for the solution of advective-dominant solute transport. *Water Resources Research*, 27(10):2645–2654, 1991.

Silke Cram, Christina Siebe, Rutilio Ortíz-Salinas, and Andrea Herre. Mobility and persistence of petroleum hydrocarbons in peat soils of southeastern mexico. *Soil & Sediment Contamination*, 13(5):341–360, 2004.

P Csomós, I Faragó, and Á Havasi. Weighted sequential splittings and their analysis. *Computers & Mathematics with Applications*, 50(7):1017–1031, 2005.

N Dal Ferro, AG Strozzi, Céline Duwig, P Delmas, P Charrier, and F Morari. Application of smoothed particle hydrodynamics (sph) and pore morphologic model to predict saturated water conductivity from x-ray ct imaging in a silty loam cambisol. *Geoderma*, 255:27–34, 2015.

Ethan E Danahy, Sos S Agaian, and Karen A Panetta. Algorithms for the resizing of binary and grayscale images using a logical transform. In *Electronic Imaging 2007*, pages 64970Z–64970Z. International Society for Optics and Photonics, 2007.

Henry Darcy. *Les fontaines publiques de la ville de Dijon: exposition et application...* Victor Dalmont, 1856.

Paul Dawkins. Heat equation with non-zero temperature boundaries, 2018. URL http://tutorial.math.lamar.edu/Classes/DE/HeatEqnNonZero.aspx.

Pierre Delage, Yu-Jun Cui, and Anh Minh Tang. Clays in radioactive waste disposal. *Journal of Rock Mechanics and Geotechnical Engineering*, 2(2): 111–123, 2010.

Manfredo Perdigao Do Carmo and Manfredo Perdigao Do Carmo. *Differential geometry of curves and surfaces*, volume 2. Prentice-hall Englewood Cliffs, 1976.

Hu Dong and Martin J. Blunt. Pore-network extraction from micro-computerized-tomography images. *Phys. Rev. E*, 80:036307, Sep 2009. doi: 10.1103/PhysRevE.80.036307. URL http://link.aps.org/doi/10.1103/PhysRevE.80.036307.

Daryl A Doughty and Liviu Tomutsa. Multinuclear nmr microscopy of two-phase fluid systems in porous rock. *Magnetic resonance imaging*, 14(7-8): 869–873, 1996.

WJ Drugan and JR Willis. A micromechanics-based nonlocal constitutive equation and estimates of representative volume element size for elastic composites. *Journal of the Mechanics and Physics of Solids*, 44(4):497–524, 1996.

François Dubois. Nonlinear interpolation and total variation diminishing schemes. *arXiv preprint arXiv:1006.3921*, 2010.

Francis AL Dullien. *Porous media: fluid transport and pore structure*. Academic press, 2012a.

Francis AL Dullien. *Porous media: fluid transport and pore structure*. Academic press, 2012b.

Dale R Durran. *Numerical methods for fluid dynamics: With applications to geophysics*, volume 32. Springer Science & Business Media, 2010.

John R Fanchi et al. Multidimensional numerical dispersion. *Society of Petroleum Engineers Journal*, 23(01):143–151, 1983.

Feng Feng, I Yucel Akkutlu, et al. Molecular modeling of organic materials for flow simulation and digital source-rock physics. In *SPE Annual Technical Conference and Exhibition*. Society of Petroleum Engineers, 2017.

Adolph Fick. V. on liquid diffusion. *The London, Edinburgh, and Dublin Philosophical Magazine and Journal of Science*, 10(63):30–39, 1855.

J. Fonseca, C. O'Sullivan, M.R. Coop, and P.D. Lee. Non-invasive characterization of particle morphology of natural sands. *Soils and Foundations*, 52 (4):712 – 722, 2012. ISSN 0038-0806. doi: https://doi.org/10.1016/j.sandf.2012.07.011. URL http://www.sciencedirect.com/science/article/pii/S0038080612000819.

JT Fredrich, AA DiGiovanni, and DR Noble. Predicting macroscopic transport properties using microscopic image data. *Journal of Geophysical Research: Solid Earth*, 111(B3), 2006.

John Goutsias and Sinan Batman. Morphological methods for biomedical image analysis. *Handbook of medical imaging*, 2:175–272, 2000.

George J Grevera and Jayaram K Udupa. Shape-based interpolation of multidimensional grey-level images. *IEEE transactions on medical imaging*, 15(6):881–892, 1996.

R. Guibert, M. Nazarova, P. Horgue, G. Hamon, P. Creux, and G. Debenest. Computational permeability determination from pore-scale imaging: Sample size, mesh and method sensitivities. *Transport in Porous Media*, 107 (3):641–656, Apr 2015a. ISSN 1573-1634. doi: 10.1007/s11242-015-0458-0. URL https://doi.org/10.1007/s11242-015-0458-0.

R. Guibert, M. Nazarova, P. Horgue, G. Hamon, P. Creux, and G. Debenest. Computational permeability determination from pore-scale imaging: Sample size, mesh and method sensitivities. *Transport in Porous Media*, 107 (3):641–656, Apr 2015b. ISSN 1573-1634. doi: 10.1007/s11242-015-0458-0. URL https://doi.org/10.1007/s11242-015-0458-0.

J. Happel and H. Brenner. *Low Reynolds number hydrodynamics: with special applications to particulate media*. Mechanics of Fluids and Transport Processes. Springer Netherlands, 2012. ISBN 9789400983526. URL https://books.google.fr/books?id=u-ptCQAAQBAJ.

Ami Harten. High resolution schemes for hyperbolic conservation laws. *Journal of computational physics*, 49(3):357–393, 1983.

Guillermo Hauke. *An introduction to fluid mechanics and transport phenomena*, volume 86. Springer, 2008.

Steven B Hawthorne, Charles D Gorecki, James A Sorensen, Edward N Steadman, John A Harju, Steve Melzer, et al. Hydrocarbon mobilization mechanisms from upper, middle, and lower bakken reservoir rocks exposed to co. In *SPE Unconventional Resources Conference Canada*. Society of Petroleum Engineers, 2013.

Alasdair N Houston, Wilfred Otten, R Falconer, Olivier Monga, Philippe C Baveye, and Simona M Hapca. Quantification of the pore size distribution of soils: Assessment of existing software using tomographic and synthetic 3d images. *Geoderma*, 299:73–82, 2017.

K Huang, N Toride, and M Th Van Genuchten. Experimental investigation of solute transport in large, homogeneous and heterogeneous, saturated soil columns. *Transport in Porous Media*, 18(3):283–302, 1995.

Marijke Huysmans and Alain Dassargues. Review of the use of péclet numbers to determine the relative importance of advection and diffusion in low permeability environments. *Hydrogeology Journal*, 13(5-6):895–904, 2005.

Pavel Iassonov, Thomas Gebrenegus, and Markus Tuller. Segmentation of x-ray computed tomography images of porous materials: A crucial step for characterization and quantitative analysis of pore structures. *Water Resources Research*, 45(9):n/a–n/a, 2009. ISSN 1944-7973. doi: 10.1029/2009WR008087. URL http://dx.doi.org/10.1029/2009WR008087.

Fei Jiang and Takeshi Tsuji. Changes in pore geometry and relative permeability caused by carbonate precipitation in porous media. *Physical Review E*, 90(5):053306, 2014.

Ruben Juanes, EJ Spiteri, FM Orr, and MJ Blunt. Impact of relative permeability hysteresis on geological co2 storage. *Water Resources Research*, 42(12), 2006a.

Ruben Juanes, EJ Spiteri, FM Orr, and MJ Blunt. Impact of relative permeability hysteresis on geological co2 storage. *Water Resources Research*, 42(12), 2006b.

Avinash M Kadam, Pravin D Nemade, GH Oza, and HARIHARAN S Shankar. Treatment of municipal wastewater using laterite-based constructed soil filter. *Ecological Engineering*, 35(7):1051–1061, 2009.

A Kaestner, E Lehmann, and M Stampanoni. Imaging and image processing in porous media research. *Advances in Water Resources*, 31(9):1174–1187, 2008.

T Kanit, S Forest, Ia Galliet, Va Mounoury, and D Jeulin. Determination of the size of the representative volume element for random composites: statistical and numerical approach. *International Journal of solids and structures*, 40(13):3647–3679, 2003.

Saskia Deborah Keesstra, Violetta Geissen, K Mosse, S Piiranen, E Scudiero, M Leistra, and Loes van Schaik. Soil as a filter for groundwater quality. *Current Opinion in Environmental Sustainability*, 4(5):507–516, 2012.

Richard A. Ketcham and William D. Carlson. Acquisition, optimization and interpretation of x-ray computed tomographic imagery: Applications to the geosciences. *Comput. Geosci.*, 27(4):381–400, May 2001. ISSN 0098-3004. doi: 10.1016/S0098-3004(00)00116-3. URL http://dx.doi.org/10.1016/S0098-3004(00)00116-3.

Faisal Khan, Frieder Enzmann, Michael Kersten, Andreas Wiegmann, and Konrad Steiner. 3d simulation of the permeability tensor in a soil aggregate on basis of nanotomographic imaging and lbe solver. *Journal of soils and sediments*, 12(1):86–96, 2012.

Dong-Ju Kim, Joung-Souk Kim, Seong-Taek Yun, and Sang-Hoon Lee. Determination of longitudinal dispersivity in an unconfined sandy aquifer. *Hydrological processes*, 16(10):1955–1964, 2002.

Kevin W King, Mark R Williams, Merrin L Macrae, Norman R Fausey, Jane Frankenberger, Douglas R Smith, Peter JA Kleinman, and Larry C Brown. Phosphorus transport in agricultural subsurface drainage: A review. *Journal of environmental quality*, 44(2):467–485, 2015.

D Klotz and H Moser. Hydrodynamic dispersion as aquifer characteristic: Model experiments with radioactive tracers. In *Isotope techniques in groundwater hydrology 1974, Vol. II. Proceedings of a symposium*, 1974.

Sandeep Kumar, Stephen H Anderson, Ranjith P Udawatta, and Clark J Gantzer. Ct-measured macropores as affected by agroforestry and grass buffers for grazed pasture systems. *Agroforestry systems*, 79(1):59–65, 2010a.

Sandeep Kumar, Stephen H Anderson, Ranjith P Udawatta, and Clark J Gantzer. Ct-measured macropores as affected by agroforestry and grass buffers for grazed pasture systems. *Agroforestry systems*, 79(1):59–65, 2010b.

P.H. Kuncoro, K. Koga, N. Satta, and Y. Muto. A study on the effect of compaction on transport properties of soil gas and water i: Relative gas diffusivity, air permeability, and saturated hydraulic conductivity. *Soil and Tillage Research*, 143:172 – 179, 2014. ISSN 0167-1987. doi: https://doi.org/10.1016/j.still.2014.02.006. URL http://www.sciencedirect.com/science/article/pii/S0167198714000282.

Miroslav Kutílek, Donald R Nielsen, et al. *Soil hydrology: texbook for students of soil science, agriculture, forestry, geoecology, hydrology, geomorphology and other related disciplines*. Catena Verlag, 1994.

Rattan Lal. Challenges and opportunities in soil organic matter research. *European Journal of Soil Science*, 60(2):158–169, 2009.

A Lallemand-Barres and P Peaudecerf. Recherche des relations entre la valeur de la dispersivité macroscopique d'un milieu aquifère, ses autres caractéristiques et les conditions de mesure. *Bull. Bur. Rech. Geol. Min., Sect 3*, 4(4), 1978.

LD Landau and EM Lifshitz. *Course of theoretical physics. vol. 6: Fluid mechanics*. London, 1959.

Christian Lang, Joachim Ohser, and Rudolf Hilfer. On the analysis of spatial binary images. *Journal of microscopy*, 203(3):303–313, 2001.

RB Lantz et al. Quantitative evaluation of numerical diffusion (truncation error). *Society of Petroleum Engineers Journal*, 11(03):315–320, 1971.

David Legland, Kiên Kiêu, and Marie-Françoise Devaux. Computation of minkowski measures on 2d and 3d binary images. *Image Analysis & Stereology*, 26(2):83–92, 2011.

Gaëtan Lehmann and David Legland. Efficient n-dimensional surface estimation using crofton formula and run-length encoding. *Insight J*, 2:1–11, 2012.

Gaëtan Lehmann, David Legland, and UMR Génie. Efficient n-dimensional surface estimation using crofton formula and run-length encoding. *Insight J*, 2012:1–11, 2012.

Johannes Lehmann and Markus Kleber. The contentious nature of soil organic matter. *Nature*, 528(7580):60, 2015.

P Lehmann, P Wyss, A Flisch, E Lehmann, P Vontobel, M Krafczyk, A Kaestner, F Beckmann, A Gygi, and H Flühler. Tomographical imaging and mathematical description of porous media used for the prediction of fluid distribution. *Vadose Zone Journal*, 5(1):80–97, 2006.

Thomas Martin Lehmann, Claudia Gonner, and Klaus Spitzer. Survey: Interpolation methods in medical image processing. *IEEE transactions on medical imaging*, 18(11):1049–1075, 1999.

J Letey. The study of soil structure-science or art. *Soil Research*, 29(6): 699–707, 1991.

Randall J LeVeque. *Finite volume methods for hyperbolic problems*, volume 31. Cambridge university press, 2002.

Haifeng Liang, Yongchen Song, Yu Liu, Mingjun Yang, and Xing Huang. Study of the permeability characteristics of porous media with methane hydrate by pore network model. *Journal of Natural Gas Chemistry*, 19(3): 255–260, 2010.

P.C. Lichtner, C.I. Steefel, E.H. Oelkers, and Mineralogical Society of America. *Reactive Transport in Porous Media*. Reviews in Mineralogy and Geochemistry Series. Mineralogical Society of America, 1996. ISBN 9780939950423. URL https://books.google.fr/books?id=nMsPAQAAIAAJ.

CL Lin and JD Miller. Pore structure and network analysis of filter cake. *Chemical Engineering Journal*, 80(1):221–231, 2000.

P Marschall, S Horseman, and Thomas Gimmi. Characterisation of gas transport properties of the opalinus clay, a potential host rock formation for radioactive waste disposal. *Oil & gas science and technology*, 60(1): 121–139, 2005.

Yashar Mehmani, Tie Sun, MT Balhoff, P Eichhubl, and S Bryant. Multiblock pore-scale modeling and upscaling of reactive transport: application to carbon sequestration. *Transport in porous media*, 95(2):305–326, 2012.

Fernando Mendoza, Pieter Verboven, Hibru K Mebatsion, Greet Kerckhofs, Martine Wevers, and Bart Nicolaï. Three-dimensional pore space quantification of apple tissue using x-ray computed microtomography. *Planta*, 226 (3):559–570, 2007.

Kevin J Miller, Laurent GJ Montési, and Wen-lu Zhu. Estimates of olivine–basaltic melt electrical conductivity using a digital rock physics approach. *Earth and Planetary Science Letters*, 432:332–341, 2015.

S. Mooney, T. Pridmore, J. Helliwell, and M. Bennett. Developing x-ray computed tomography to non-invasively image 3-d root systems architecture in soil. *Plant and Soil*, 352(1/2):1 – 22, 2012. ISSN 0032079X. URL http://search.ebscohost.com.biblioplanets.gate.inist.fr/login.aspx?direct=true&db=a9h&AN=73034975&lang=fr&site=ehost-live.

Peyman Mostaghimi, Martin J Blunt, and Branko Bijeljic. Computations of absolute permeability on micro-ct images. *Mathematical Geosciences*, 45 (1):103–125, 2013.

Francisco Javier Muñoz-Ortega, F San José Martínez, and FJ Caniego Monreal. Volume, surface, connectivity and size distribution of soil pore space in ct images: comparison of samples at different depths from nearby natural and tillage areas. *Pure and Applied Geophysics*, 172(1):167–179, 2015.

Shinji Nakaya, Taiyoh Yohmei, Akihisa Koike, Tetsuhiro Hirayama, Toshiaki Yoden, and Makoto Nishigaki. Determination of anisotropy of spatial correlation structure in a three-dimensional permeability field accompanied by shallow faults. *Water resources research*, 38(8), 2002.

Donald A Nield, Adrian Bejan, et al. *Convection in porous media*, volume 3. Springer, 2006a.

Donald A Nield, Adrian Bejan, et al. *Convection in porous media*, volume 3. Springer, 2006b.

Joachim Ohser and Frank Mücklich. *Statistical analysis of microstructures in materials science*. Wiley, 2000.

Saeed Ovaysi and Mohammad Piri. Pore-scale modeling of dispersion in disordered porous media. *Journal of contaminant hydrology*, 124(1-4):68–81, 2011.

J Anthony Parker, Robert V Kenyon, and Donald E Troxel. Comparison of interpolating methods for image resampling. *IEEE Transactions on medical imaging*, 2(1):31–39, 1983.

JB Passioura and DA Rose. Hydrodynamic dispersion in aggregated media: 2. effects of velocity and aggregate size. *Soil Science*, 111(6):345–351, 1971.

MK Patel, NC Markatos, and M Cross. A critical evaluation of seven discretization schemes for convection–diffusion equations. *International journal for numerical methods in fluids*, 5(3):225–244, 1985.

Timothy J Pedley. Introduction to fluid dynamics. *Scientia Marina*, 61:7–24, 1997.

Zhe Peng, Celine Duwig, Jean Paul Gaudet, Alfonso Gastelum Strozzi, Pascal Charrier, Herve Denis, et al. Dynamic visualization of water flow heterogeneous porous media by x-rays computed tomography. In *EGU General Assembly Conference Abstracts*, volume 16, 2014.

John F Pickens and Gerald E Grisak. Scale-dependent dispersion in a stratified granular aquifer. *Water Resources Research*, 17(4):1191–1211, 1981a.

John F Pickens and Gerald E Grisak. Scale-dependent dispersion in a stratified granular aquifer. *Water Resources Research*, 17(4):1191–1211, 1981b.

Massimo Prosdocimi, Artemi Cerdà, and Paolo Tarolli. Soil water erosion on mediterranean vineyards: A review. *Catena*, 141:1–21, 2016.

Larry J Puckett and W Brian Hughes. Transport and fate of nitrate and pesticides. *Journal of Environmental Quality*, 34(6):2278–2292, 2005.

Miriam Patricia Ortega Ramírez, Laurent Oxarango, and Alfonso Gastelum Strozzi. Effect of x-ray ct resolution on the quality of permeability computation for granular soils: definition of a criterion based on morphological properties. *Soil Research*.

Nadège Reboul, Eric Vincens, and Bernard Cambou. A statistical analysis of void size distribution in a simulated narrowly graded packing of spheres. *Granular Matter*, 10(6):457–468, 2008.

Xiaoya Ren, Guangming Zeng, Lin Tang, Jingjing Wang, Jia Wan, Yani Liu, Jiangfang Yu, Huan Yi, Shujing Ye, and Rui Deng. Sorption, transport and biodegradation–an insight into bioavailability of persistent organic pollutants in soil. *Science of the total environment*, 610:1154–1163, 2018.

TW Ridler, S Calvard, et al. Picture thresholding using an iterative selection method. *IEEE trans syst Man Cybern*, 8(8):630–632, 1978.

Olivier Rozenbaum and S Rolland du Roscoat. Representative elementary volume assessment of three-dimensional x-ray microtomography images of heterogeneous materials: Application to limestones. *Physical Review E*, 89 (5):053304, 2014.

Vita Rutka. A staggered grid-based explicit jump immersed interface method for two-dimensional stokes flows. *International journal for numerical methods in fluids*, 57(10):1527–1543, 2008.

PG Saffman. Dispersion due to molecular diffusion and macroscopic mixing in flow through a network of capillaries. *Journal of Fluid Mechanics*, 7(2): 194–208, 1960.

Luis A Santaló. *Integral geometry and geometric probability*. Cambridge university press, 2004.

Adrian E Scheidegger. General theory of dispersion in porous media. *Journal of Geophysical Research*, 66(10):3273–3278, 1961.

Jon E Schoonover and Jackie F Crim. An introduction to soil concepts and the role of soils in watershed management. *Journal of Contemporary Water Research & Education*, 154(1):21–47, 2015.

Jean Serra. *Image analysis and mathematical morphology, v. 1.* Academic press, 1982.

SM Shah, F Gray, JP Crawshaw, and ES Boek. Micro-computed tomography pore-scale study of flow in porous media: Effect of voxel resolution. *Advances in water resources*, 95:276–287, 2016.

Dmitriy Silin and Tad Patzek. Pore space morphology analysis using maximal inscribed spheres. *Physica A: Statistical Mechanics and its Applications*, 371(2):336 – 360, 2006. ISSN 0378-4371. doi: http://dx.doi.org/10.1016/j.physa.2006.04.048. URL http://www.sciencedirect.com/science/article/pii/S037843710600464X.

Hassan Smaoui, Lahcen Zouhri, and Abdellatif Ouahsine. Flux-limiting techniques for simulation of pollutant transport in porous media: Application to groundwater management. *Mathematical and Computer Modelling*, 47 (1-2):47–59, 2008.

Hans Jorg Vogel Steffen Schluter, Ulrich Weller. Segmentation of x-ray microtomography images of soil using gradient masks. *Computers and Geosciences*, 36(10):1246 – 1251, 2010. ISSN 0098-3004. doi: http://dx.doi.org/10.1016/j.cageo.2010.02.007. URL http://www.sciencedirect.com/science/article/pii/S0098300410001457.

Peter K Sweby. High resolution schemes using flux limiters for hyperbolic conservation laws. *SIAM journal on numerical analysis*, 21(5):995–1011, 1984.

Richard Szeliski. *Computer vision: algorithms and applications*. Springer Science & Business Media, 2010.

Gamze Tanoğlu et al. Operator splitting methhods for differential equations. Master's thesis, Izmir Institute of Technology, 2010.

GI Taylor. Diffusion and mass transport in tubes. *Proceedings of the Physical Society. Section B*, 67(12):857, 1954.

N Toride, FJ Leij, M Th Van Genuchten, et al. The cxtfit code for estimating transport parameters from laboratory or field tracer experiments. Technical report, version 2.0, research report, 1995.

Bram Van Leer. Towards the ultimate conservative difference scheme. v. a second-order sequel to godunov's method. *Journal of computational Physics*, 32(1):101–136, 1979.

Marnik Vanclooster, JJTI Boesten, A Tiktak, N Jarvis, JG Kroes, R Muñoz-Carpena, R Clothier, and SR Green. On the use of unsaturated flow and transport models in nutrient and pesticide management. *Frontis*, pages 331–361, 2005.

H-J Vogel and K Roth. Quantitative morphology and network representation of soil pore structure. *Advances in water resources*, 24(3-4):233–242, 2001.

H-J Vogel, Ulrich Weller, and Steffen Schlüter. Quantification of soil structure based on minkowski functions. *Computers & Geosciences*, 36(10):1236–1245, 2010.

HJ Vogel and K Roth. A new approach for determining effective soil hydraulic functions. *European Journal of Soil Science*, 49(4):547–556, 1998.

Jing Wang, Zhongzhi Zhang, Youming Su, Wei He, Feng He, and Hongguang Song. Phytoremediation of petroleum polluted soil. *Petroleum Science*, 5 (2):167–171, 2008.

Christoph Wanner, Sonja Zink, Urs Eggenberger, and Urs Mäder. Assessing the cr (vi) reduction efficiency of a permeable reactive barrier using cr isotope measurements and 2d reactive transport modeling. *Journal of contaminant hydrology*, 131(1-4):54–63, 2012.

Anne Weber, Aki S Ruhl, and Richard T Amos. Investigating dominant processes in zvi permeable reactive barriers using reactive transport modeling. *Journal of contaminant hydrology*, 151:68–82, 2013.

Stephen Whitaker. Flow in porous media i: A theoretical derivation of darcy's law. *Transport in porous media*, 1(1):3–25, 1986.

Stephen Whitaker. *The method of volume averaging*, volume 13. Springer Science & Business Media, 2013.

Frank M White. Fluid mechanics. Technical report, McGraw-hill, 1986.

A Wiegmann. Computation of the permeability of porous materials from their microstructure by fff-stokes. *Bericht des Fraunhofer ITWM*, 2007.

Andreas Wiegmann and Kenneth P Bube. The explicit-jump immersed interface method: finite difference methods for pdes with piecewise smooth solutions. *SIAM Journal on Numerical Analysis*, 37(3):827–862, 2000a.

Andreas Wiegmann and Kenneth P Bube. The explicit-jump immersed interface method: finite difference methods for pdes with piecewise smooth solutions. *SIAM Journal on Numerical Analysis*, 37(3):827–862, 2000b.

Dorthe Wildenschild and Adrian P. Sheppard. X-ray imaging and analysis techniques for quantifying pore-scale structure and processes in subsurface porous medium systems. *Advances in Water Resources*, 51(0):217 – 246, 2013. ISSN 0309-1708. doi: http://dx.doi.org/10.1016/j.advwatres.2012.07.018. URL http://www.sciencedirect.com/science/article/pii/S0309170812002060. 35th Year Anniversary Issue.

Qing-Hua Wu, Zhen Lu, and Tianyao Ji. *Protective relaying of power systems using mathematical morphology*. Springer Science & Business Media, 2009.

Xiaofan Yang, Yashar Mehmani, William A Perkins, Andrea Pasquali, Martin Schönherr, Kyungjoo Kim, Mauro Perego, Michael L Parks, Nathaniel Trask, Matthew T Balhoff, Marshall C Richmond, Martin Geier, Manfred Krafczyk, Li-Shi Luo, Alexandre M Tartakovsky, and Timothy D Scheibe. Intercomparison of 3d pore-scale flow and solute transport simulation methods. *Advances in water resources*, 95:176–189, 2016a.

Xiaofan Yang, Yashar Mehmani, William A Perkins, Andrea Pasquali, Martin Schönherr, Kyungjoo Kim, Mauro Perego, Michael L Parks, Nathaniel Trask, Matthew T Balhoff, et al. Intercomparison of 3d pore-scale flow and solute transport simulation methods. *Advances in water resources*, 95:176–189, 2016b.

Hongkyu Yoon and Thomas A Dewers. Nanopore structures, statistically representative elementary volumes, and transport properties of chalk. *Geophysical Research Letters*, 40(16):4294–4298, 2013.

Yan Zaretskiy, Sebastian Geiger, Ken Sorbie, and Malte Förster. Efficient flow and transport simulations in reconstructed 3d pore geometries. *Advances in Water Resources*, 33(12):1508–1516, 2010a.

Yan Zaretskiy, Sebastian Geiger, Ken Sorbie, and Malte Förster. Efficient flow and transport simulations in reconstructed 3d pore geometries. *Advances in Water Resources*, 33(12):1508–1516, 2010b.

Dongxiao Zhang, Raoyang Zhang, Shiyi Chen, and Wendy E Soll. Pore scale study of flow in porous media: Scale dependency, rev, and statistical rev. *Geophysical research letters*, 27(8):1195–1198, 2000.